SENSORDEVICES 2023

The Fourteenth International Conference on Sensor Device Technologies and Applications

ISBN: 978-1-68558-091-9

September 25 - 29, 2023

Porto, Portugal

SENSORDEVICES 2023 Editors

Lorena Parra Boronat, Universitat Politècnica de València, Spain
Narito Kurata, Tsukuba University of Technology, Japan

SENSORDEVICES 2023

Forward

The Fourteenth International Conference on Sensor Device Technologies and Applications (SENSORDEVICES 2023), held on September 25-29, 2023, continued a series of events focusing on sensor devices themselves, the technology-capturing style of sensors, special technologies, signal control and interfaces, and particularly sensors-oriented applications. The evolution of the nano-and microtechnologies, nanomaterials, and the new business services make the sensor device industry and research on sensor-themselves very challenging.

Most of the sensor-oriented research and industry initiatives are focusing on sensor networks, data security, exchange protocols, energy optimization, and features related to intermittent connections. Recently, the concept of Internet-of-things gathers attention, especially when integrating IPv4 and IIPv6 networks. We welcomed technical papers presenting research and practical results, position papers addressing the pros and cons of specific proposals, such as those being discussed in the standard fora or in industry consortia, survey papers addressing the key problems and solutions on any of the above topics short papers on work in progress, and panel proposals.

We take here the opportunity to warmly thank all the members of the SENSORDEVICES 2023 technical program committee, as well as all the reviewers. The creation of such a high quality conference program would not have been possible without their involvement. We also kindly thank all the authors who dedicated much of their time and effort to contribute to SENSORDEVICES 2023. We truly believe that, thanks to all these efforts, the final conference program consisted of top quality contributions.

We also thank the members of the SENSORDEVICES 2023 organizing committee for their help in handling the logistics and for their work that made this professional meeting a success.

We hope that SENSORDEVICES 2023 was a successful international forum for the exchange of ideas and results between academia and industry and to promote further progress in the area of sensor devices technologies and applications. We also hope that Porto provided a pleasant environment during the conference and everyone saved some time to enjoy the historic charm of the city.

SENSORDEVICES 2023 Chairs

SENSORDEVICES 2023 Steering Committee
Arcady Zhukov, University of Basque Country (UPV/EHU), San Sebastian / Ikerbasque, Basque Foundation for Science, Bilbao, Spain
Narito Kurata, Tsukuba University of Technology, Japan
Sazzadur Chowdhury. University of Windsor, Canada
Manuela Vieira, CTS/ISEL/IPL, Portugal
Toshihiko Kiwa, Okayama University, Japan

SENSORDEVICES 2023 Publicity Chair
Lorena Parra Boronat, Universitat Politecnica de Valencia, Spain
Laura Garcia, Universitat Politecnica de Valencia, Spain

SENSORDEVICES 2023

Committee

SENSORDEVICES 2023 Steering Committee
Arcady Zhukov, University of Basque Country (UPV/EHU), San Sebastian / Ikerbasque, Basque
Foundation for Science, Bilbao, Spain
Narito Kurata, Tsukuba University of Technology, Japan
Sazzadur Chowdhury. University of Windsor, Canada
Manuela Vieira, CTS/ISEL/IPL, Portugal
Toshihiko Kiwa, Okayama University, Japan

SENSORDEVICES 2023 Publicity Chair
Lorena Parra Boronat, Universitat Politecnica de Valencia, Spain
Laura Garcia, Universitat Politecnica de Valencia, Spain

SENSORDEVICES 2023 Technical Program Committee

Ahmed Alfadhel, Rochester Institute of Technology, USA / Research Products Development Company,
Saudi Arabia
Jesús B. Alonso Hernández, Institute for Technological Development and Innovation in Communications
(IDeTIC) | University of Las Palmas de Gran Canaria (ULPGC), Spain
Sebastian Anand Alphonse, LivaNova PLC, Houston, USA
Ahmed Ammar, Ohio Northern University, USA
Ismael Andrade Pimentel, Pontifical Catholic University of Rio de Janeiro. Brazil
Darius Andriukaitis, Kaunas University of Technology (KTU), Lithuania
Francisco Arcega, University of Zaragoza, Spain
Aktham Asfour, University Grenoble Alpes | CNRS | Grenoble INP, France
Herve Aubert, Laboratory for Analysis and Architecture of Systems (LAAS-CNRS), Toulouse, France
Ripendra Awal, Prairie View A&M University, USA
Orlando R. Baiocchi, University of Washinton Tacoma, USA
Valerio Baiocchi, "Sapienza" University of Rome, Italy
Camelia Bala, University of Bucharest, Romania
Krishnan Balasubramaniam, Indian Institute of Technology Madras, India
Jose Barata, NOVA University of Lisbon, Portugal
Yoseph Bar-Cohen, Jet Propulsion Laboratory | NASA, USA
Michal Borecki, Warsaw University of Technology | Institute of MIcroelectronics and Optoelectronics,
Poland
Christos Bouras, University of Patras, Greece
Manuel José Cabral dos Santos Reis, IEETA / University of Trás-os-Montes e Alto Douro, Portugal
Luigi Campanella, Sapienza University of Rome, Italy
Juan-Carlos Cano, Universitat Politecnica de Valencia, Spain
Nicola Carbonaro, Research Centre "E. Piaggio" | University of Pisa, Italy
Vítor Carvalho, 2Ai Lab- School of Technology - IPCA / Algoritmi Research Center - Minho University,
Portugal
Paula María Castro Castro, University of A Coruña, Spain

Fulvio Re Cecconi, Politecnico di Milano, Italy
Diliang Chen, University of New Hampshire, USA
Irinela Chilibon, National Institute of Research and Development for Optoelectronics - INOE-2000, Romania
Raad Farhood Chisab, Middle Technical University, Baghdad, Iraq
Nan-Fu Chiu, National Taiwan Normal University, Taiwan
Chi-Wai Chow, National Chiao Tung University, Hsinchu, Taiwan
Sazzadur Chowdhury, University of Windsor, Canada
Juan M. Corchado, University of Salamanca, Spain
Marco Crescentini, University of Bologna, Italy
Francesco G. Della Corte, Università degli Studi di Napoli Federico II, Italy
Emiliano Descrovi, Norwegian University of Science and Technology (NTNU), Trondheim, Norway / Polytechnic University of Turin, Torino, Italy
Abdou Karim Diallo,Gaston Berger University, Senegal
Dermot Diamond, Dublin City University, Ireland
Amad Ud Din, Fatima Jinnah Women University, Pakistan
Toan Dinh, University of Southern Queensland, Australia
Bahram Djafari Rouhani, University of Lille, France
René Domínguez-Cruz, Universidad Autónoma de Tamaulipas, Mexico
Mingzheng Duan, University of California Berkeley, USA
Jimmy T. Efird, CSPEC/DVAHCS/HSR&D (Duke University Affiliated Center), Durham, USA
Eugenia Fagadar-Cosma, Institute of Chemistry "Coriolan Dragulescu", Timisoara, Romania
Francisco Falcone, UPNA-ISC, Spain
Vittorio Ferrari, University of Brescia, Italy
Laurent Fesquet, Grenoble Institute of Technology, France
Rui Fonseca-Pinto, Polytechnic of Leiria, Portugal
Nazila Fough, Robert Gordon University, UK
Óscar Fresnedo Arias, University of A Coruña, Spain
Mounir Gaidi, University of Sharjah, UAE
Juan Carlos García, University of Alcala, Spain
Cécile Ghouila-Houri, Centrale Lille, France
Francesca Giannone, Niccolò Cusano University, Rome, Italy
Michele Giordano, IPCB - CNR, Italy
Jan Havlík, Czech Technical University in Prague, Czech Republic
Lukas Heindler, Johannes Kepler University Linz, Austria
Johan Holmgren, Malmö University, Sweden
M. Carmen Horrillo Güemes, Group of Technology of Advanced Sensors (SENSAVAN)-ITEFI-CSIC, Spain
Wen-Jyi Hwang, National Taiwan Normal University, Taipei, Taiwan
Mohamed Ichchou, Ecole Centrale de Lyon, France
Raul Igual, EUP Teruel | University of Zaragoza, Spain
Illyas Md Isa, Universiti Pendidikan Sultan Idris, Malaysia
Kh Tohidul Islam, The University of Melbourne | Melbourne Medical School, Australia
Chi-Shih Jao, University of California, Irvine, USA
Mark Kagarura, Paderborn University, Germany / Makerere University, Uganda
Grigoris Kaltsas, University of West Attica, Greece
Rajesh Khanna, Thapar Institute of Engineering and Technology, India
Ahmed Khorshid, Advanced Micro Devices (AMD), USA
Hyunook Kim, University of Seoul, Korea

Farzana Kulsoom, University of Engineering and Technology, Taxila, Pakistan
Narito Kurata, Tsukuba University of Technology, Japan
José Luis Lázaro-Galilea, University of Alcalá, Spain
Ching-Ting Lee, Yuan Ze University / National Cheng-Kung University, Taiwan
Gyu Myoung Lee, Liverpool John Moores University, UK
Kevin Lee, School of InformationTechnology | Deakin University, Melbourne, Australia
Martin Lenzhofer, SiliconAustriaLabsGmbH, Austria
Diego Liberati, National Research Council of Italy, Italy
Eduard Llobet, Universitat Rovira i Virgili, Spain
Adrian Luca, Lausanne University Hospital, Switzerland
Jerzy P. Lukaszewicz, Nicoulaus Copernicus University, Torun, Poland
Zhipeng Ma, School of Aeronautics and Astronautics | Zhejiang University, China
Joaquim Miguel Maia, Federal University of Technology - Paraná (UTFPR), Brazil
Oleksandr Makeyev, School of STEM | Diné College, USA
Jorge Marcos Acevedo, University of Vigo, Spain
Stefano Mariani, Politecnico di Milano, Italy
Carlo Massaroni, Università Campus Bio-Medico di Roma, Italy
Vojko Matko, University of Maribor, Slovenia
Demétrio Matos, Polytechnic Institute of Cávado and Ave |School of Design-ID+,Portugal
Carlos Montez, Federal University of Santa Catarina, Brazil
Rafael Morales Herrera, University of Castilla-La Mancha, Spain
Kebria Naderi, Guilan University, Rasht, Iran
Masanari Nakamura, Hokkaido University, Japan
Phendukani Ncube, Gwanda State University, Zimbabwe
Tanzila Noushin, The University of Texas at Dallas, USA
Michal Nowicki, Warsaw University of Technology, Poland
Mehmet Akif Ozdemir, Izmir Katip Celebi University, Turkey
Vinayak Pachkawade, SenseAll, India
Sujata Pal, Indian Institute of Technology, Ropar, India
Evangelos Papadopoulos, National Technical University of Athens, Greece
François Pérès, University of Toulouse, France
Ivan Miguel Pires, Instituto de Telecomunicações - Universidade da Beira Interior / Polytechnic Institute
of Viseu, Portugal
R. N. Ponnalagu, BITS Pilani, Hyderabad campus, India
Patrick Pons, CNRS-LAAS, Toulouse, France
Kushal K. Ponugoti, North Dakota State University, USA
Cleonilson Protasio de Souza, Federal University of Paraiba, Brazil
Radislav A. Potyrailo, GE Research, USA
Vaishak Prathap, State University of New York at Buffalo, USA
Antonio L. L. Ramos, University of South-Eastern Norway (USN), Norway
Mounir Bousbia Salah, BADJI Mokhtar Annaba University, Algeria
Mariano Raboso Mateos, Junta de Andalucía - Consejería de Educación, Spain
S. Radhakrishnan, Maharashtra Institute of Technology, India
Luca Rampini, Politecnico di Milano, Italy
Marwa Rezeg, EI&TIC Lab | National Engineering School of Carthage | University of Carthage, Tunisia
Helena Rifà-Pous, Universitat Oberta de Catalunya, Spain
Almudena Rivadeneyra, University of Granada, Spain
Christos Riziotis, National Hellenic Research Foundation, Greece

Copyright Information

For your reference, this is the text governing the copyright release for material published by IARIA.

The copyright release is a transfer of publication rights, which allows IARIA and its partners to drive the dissemination of the published material. This allows IARIA to give articles increased visibility via distribution, inclusion in libraries, and arrangements for submission to indexes.

I, the undersigned, declare that the article is original, and that I represent the authors of this article in the copyright release matters. If this work has been done as work-for-hire, I have obtained all necessary clearances to execute a copyright release. I hereby irrevocably transfer exclusive copyright for this material to IARIA. I give IARIA permission or reproduce the work in any media format such as, but not limited to, print, digital, or electronic. I give IARIA permission to distribute the materials without restriction to any institutions or individuals. I give IARIA permission to submit the work for inclusion in article repositories as IARIA sees fit.

I, the undersigned, declare that to the best of my knowledge, the article is does not contain libelous or otherwise unlawful contents or invading the right of privacy or infringing on a proprietary right.

Following the copyright release, any circulated version of the article must bear the copyright notice and any header and footer information that IARIA applies to the published article.

IARIA grants royalty-free permission to the authors to disseminate the work, under the above provisions, for any academic, commercial, or industrial use. IARIA grants royalty-free permission to any individuals or institutions to make the article available electronically, online, or in print.

IARIA acknowledges that rights to any algorithm, process, procedure, apparatus, or articles of manufacture remain with the authors and their employers.

I, the undersigned, understand that IARIA will not be liable, in contract, tort (including, without limitation, negligence), pre-contract or other representations (other than fraudulent misrepresentations) or otherwise in connection with the publication of my work.

Exception to the above is made for work-for-hire performed while employed by the government. In that case, copyright to the material remains with the said government. The rightful owners (authors and government entity) grant unlimited and unrestricted permission to IARIA, IARIA's contractors, and IARIA's partners to further distribute the work.

Table of Contents

Autocorrelation Average Based Sensing Technique for Cognitive Radio Networks

Lyes Labsis
Signal Processing Laboratory
Ecole Militaire Polytechnique
Bordj El Bahri, Algiers, BP17, Algeria
Email:
lyes.labs@gmail.com

Djamel Teguig
Telecommunications Laboratory
Ecole Militaire Polytechnique
Bordj El Bahri, Algiers, BP17, Algeria
Email:
djamel_teg@yahoo.com

Nacerredine Lassami
Signal Processing Laboratory
Ecole Militaire Polytechnique
Bordj El Bahri, Algiers, BP17, Algeria
Email:
lassami.nacerredine@gmail.com

Abstract—The increasing sophistication in the technological requirements of modern life has created intractable problems in controlling and managing the limited sources of frequency bands. While all modern wireless systems mainly propose to reconsider novel methods of exploiting these frequencies. Cognitive radio network techniques required both spectrum sensing and dynamic spectrum access to solve the problem of resources management. Where, the spectrum sensing aspect provide all information about the utilization stat of frequency bands. The secondary users get actions according to this information by adopting the Dynamic Spectrum Access (DSA). Those unlicensed users get the permission to use the frequency bands of primary/licensed users when it was free. This approaches had many difficulties citing the unpredictable communication conditions first, and secondly, the amount of damage caused by any wrong sensing detection. This paper presents the detection capabilities using a novel idea based on the signal correlation proprieties. This novel technique use the average of the three first correlation lags as a statistic parameter. Starting by presenting the optimized detector parameters and its efficiency in simulation environments. Ultimately, the practical implementation serves to validate the detection capabilities of the technique within an authentic FM Radio broadcasting setting. This involves utilizing the Register Transfer-Level Software Defined Radio (RTL-SDR) dongle to capture the FM signal, while leveraging the GNU Radio software platform to both showcase the efficacy of the technique and highlight its limitations.

Index Terms—*Spectrum sensing*, *Cognitive radio networks*, *Radio Spectrum*, *Correlation function*

I. INTRODUCTION

Recent statistical data reveals significant congestion in frequency utilization, prompting scientific investigation into strategies for managing frequency resources. Cognitive Radio (CR), introduced by [7], addresses spectrum scarcity through Spectrum Sensing (SS) and Dynamic Spectrum Access (DSA), enabling secondary users (SUs) to opportunistically reuse unoccupied bands. Various spectrum sensing techniques exist, yet none fully overcome real-world limitations. Energy detection, highlighted by [3] proves efficient for narrowband sensing. It compares received signal power against a threshold to identify primary user signals. Despite simplicity, susceptibility to low Signal-to-Noise Ratio (SNR) drives exploration of alternatives. Methods comparing signal statistics with established knowledge offer efficacy, but with higher complexity. Matched filters

[6] and cyclostationary techniques [11] use signal pattern databases, while [2] suggest autocorrelation for weak signal detection. [8] propose an autocorrelation-based statistic using Lag_1 and Lag_0 values. Similarly, Sharma et al. [10] advocate the sum of the first two autocorrelation lags. Correlation Sum (CorrSum) outperforms other techniques. Reyes et al. [9] explore autocorrelation-based sensing, comparing correlation detection, Euclidean distance, and energy detection for cognitive radio networks. The authors in [4] suggest utilizing the variance of autocorrelation coefficients as a statistical parameter, demonstrating its strong performance in spectrum sensing. Despite the array of solutions available, they fall short since Dynamic Spectrum Access (DSA) requires the utilization of a spectrum sensing technique that can operate effectively in practical real-world implementations for both narrow and wideband channels, even in the absence of prior knowledge, and yield commendable performance outcomes.

In practice, multiple sensing parameters are employed to evaluate the robustness of each detector. Notably, the probability of detection is a pivotal metric reflecting a detector's capabilities, often assessed through analysis of Signal-to-Noise Ratio (SNR) variations to elucidate sensing limitations. Another crucial parameter is the probability of false alarm, representing unnecessary frequency band consumption when the detector is utilized. Instances of false alarm declarations treat a channel as occupied, even if it remains available. Conversely, the probability of miss detection pertains to misclassifying an occupied channel as vacant, potentially leading to communication interference and operational disruptions between licensed and unlicensed users.

The wish list and the desired enhancements encompassed a range of anticipated features, notably a streamlined version of the spectral detection system to aid practical real-time implementation. The primary aspiration was to achieve a notably high detection probability, coupled with an acceptable false alarm probability, ensuring the dependable administration of spectral resources and preventing undesirable interference between licensed and non-licensed users. In our research, we suggest utilizing specific correlation characteristics of received signals as statistical measures. Notably, autocorrelation values tend to quickly converge to zero when noise is present,
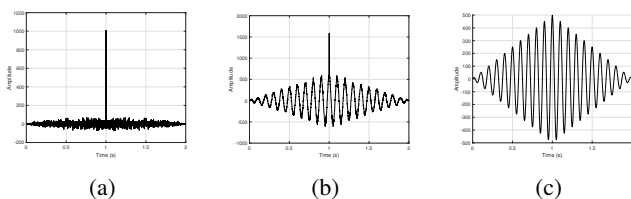
Fig. 1: Autocorrelation function of the noise signal (a) and a noisy signal (b) and a periodic signal (c)

whereas this trend is more gradual in other scenarios. Incorporating these insights, calculating the average of the first three lags results in a more pronounced distinction between scenarios involving noise and those with a noisy signal. Typically, beyond the fourth lag, the discrepancies in magnitude between lag values become more consistently aligned. The aim of this approach is to assess a novel, straightforward, and blind technique that can achieve a prominent position among conventional spectrum sensing methods.

The remainder of this paper is organized by detailing the following sections. The technique proposed system model is explained in Section II. Section III provides an exposition of the technique, encompassing its principles and the modeling of its detection methodology. The characterization of the correlation average sensing technique and its subsequent evaluation through simulation are expounded in Section IV. Utilizing a Software-Defined Radio (SDR) implementation on the GNU Radio platform, practical sensing outcomes are detailed in Section V. Concluding remarks are furnished in Section VI.

II. SYSTEM MODEL

In wireless communication systems the received signal X(n) always has some noise components W (n). In addition, the sensing technique procedure is used to detect the primary user signal S (n) presence or absence. All that makes the spectrum sensing process shortened as the following binary hypotheses test:

$$
\begin{array}{llll}
H_0 & : & X(n) = W(n) \\
H_1 & : & X(n) = S(n) + W(n)
\end{array} \tag{1}
$$

Where H_0 hypothesis means absence of the PU signal, and the inverse H_1 assumed that the PU signal is present. In this paper the PU signal is supposed M-PSK or M-QAM modulated signal in simulations and the noise is supposed Gaussian. However, in implementation, the received signal is a real received FM broadcasting signal undefined noise nature.

The detector principles based on comparing the statistic parameter T to a chosen threshold λ to differentiate between cases of PU signal presence or absence. The detector sets its outputs H_1 to 1 and fixes H_0 at 0 when the statistic parameter is greater than the threshold. However, in the opposite cases the parameters H1 and H0 are respectively fixed to 0 and 1, as it is mentioned in the following equation:

$$
\begin{cases}
T > \lambda & H_0 \\
T < \lambda & H_1
\end{cases} \tag{2}
$$

TABLE I: NUMERICAL SIMULATION PARAMETERS AND RESULTS.

Parameters	Values
Number of samples	1000
Sampling frequency	8000
Noise signal	$N(t) \sim \mathcal{N}(0,1)$
Periodic signal	$cos(100\pi t)$
Time domain	$\frac{1}{Fs}(1:1:1000)$
Statistic parameter T of the two first lags	0.89 periodic signal 0.61 noise
Statistic parameter T of the three first lags	**0.81** periodic signal **0.48** noise
Statistic parameter T of the four first lags	0.73 periodic signal 0.42 noise
Statistic parameter T of the five first lags	0.67 periodic signal 0.37 noise

$\mathcal{N}(\mu, \sigma^2)$ is a Gaussian distribution with μ mean and the variance σ^2.

III. AUTOCORRELATION AVERAGE SENSING PROCESS

The autocorrelation is a continuous function represented by the integration of the product between a signal and its time-shifted version. The time instances at which the correlation function is evaluated are referred to as lags. Analyzing these lags provides deeper insights into the signal's behavior, revealing the degree of independence between the signal and its temporally shifted counterpart. At the origin, the autocorrelation function achieves its maximum value, which is equivalent to the signal's energy. Mathematically, for a continuous-time signal $x(t)$, the autocorrelation function at the origin $R(0)$ is expressed as follows:

$$
R(0) = \int_{-\infty}^{\infty} x(t) \cdot x(t)\, dt = \text{Energy of the signal}
$$

The maximum value of the autocorrelation function experiences rapid decline in the presence of noise signals, and a more gradual decrease for correlated signals or signals with noise interference. This intriguing variation has prompted researchers to explore leveraging these distinctive patterns to differentiate between noise and other types of signals.

Consider Figure 1, which portrays three distinct simulation scenarios. Figure 1a showcases an instance of an uncorrelated signal (Additive Gaussian White Noise - AGWN signal). On the other hand, Figures 1b and 1c illustrate the autocorrelation function of a signal with noise interference and a periodic signal, respectively (correlated signals). The figure visually demonstrates the slower convergence of the autocorrelation function to zero for periodic signals, and its notably faster convergence for noisy signals. Conversely, for noise signals, the autocorrelation values swiftly approach zero. Table 1 provides a concise overview of simulation parameters and the corresponding statistical parameter values for each of these scenarios.

Table 1 resumes many simulation parameters and outline some interesting statistical indices. The table values are illustrated from the autocorrelation functions presented the figure 1. This figure plots the three different simulation cases. Table 1 presents two main ideas. The effectiveness of utilization of the

average of the three first lags as statistic parameter first, then a simple comparison between some statistical parameters to mention the purposes of limiting the average in the three first lags only. Generally, as much the difference between statistic parameter of the noise and the other cases is increased, the operation of choosing of the required threshold be easy.

Upon reviewing the contents of this table, the detection factors prominently demonstrate the innate sensing capabilities embedded within the proposed autocorrelation average-based sensing approach. In practical scenarios, the focal points regarding sensing capabilities frequently center on the straightforwardness of the sensing algorithm and the feasibility of its implementation. These attributes collectively position this proposed method at a higher vantage point relative to all currently existing narrowband sensing techniques.

For instance, when utilizing solely the initial three lags for statistical computation, the most notable disparity between noise and periodic signal instances becomes apparent, resulting in reduced computational load. Taking these insights into account, a suitable threshold can be established within the range of 0.6 to 0.7 for the specified statistical parameter presented in the following equation:

$$T = \frac{\mathrm{lag}_0 + \mathrm{lag}_1 + \mathrm{lag}_2}{3\,\mathrm{lag}_0} \qquad (3)$$

IV. Technique characterization and evaluation results

In order to define the techniques characteristics and to evaluate its performances. Many simulations have been realized using MATLAB platform [1]. At first, the proposed technique was tested to outline the effect of variation of both the threshold and the number of sample on the P_{fa} values. This operation was stimulated to mention the appropriate P_{fa} target value according to these parameters. Secondly, the proposed technique was evaluated to guess its efficiency compared to those of the reference sensing techniques in two different environments. The first environment is when the treated signal is a 4-QAM modulated signal. However, the second one is when the received signal is an 8-PSK modulated signal.

Figure 2 illustrates the initial impact of the chosen threshold on the target values of P_{fa}. It is evident that an inverse correlation exists between these two parameters. As the threshold increases, the probability of false alarm diminishes. A stable phase of P_{fa} values emerges at 0.5, highlighting the constancy in these values despite fluctuations in the threshold selection. This stability underscores the efficacy of leveraging such statistical parameters, effectively discerning noise cases from noisy signals. The persistent stability of P_{fa} values at 0.5 indicates a substantial gap between the two distinct states, a crucial requirement for accurate differentiation. This gap serves as a safety margin to prevent high false alarm probabilities arising from incorrect threshold choices. Furthermore, the simulation reveals the influence of varying the number of processed points on both the optimal threshold and the probability of false alarm. Notably, an increase in the number of processed points
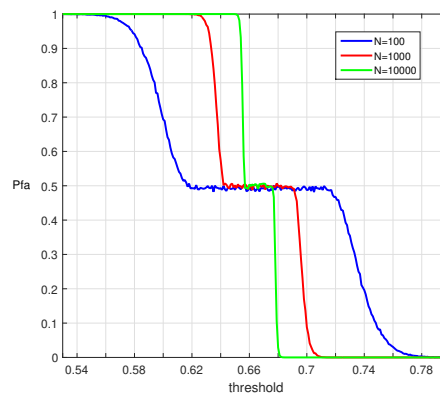

Fig. 2: The P_{fa} versus the selected threshold and for different number of samples in case of an 8-PSK modulated signal
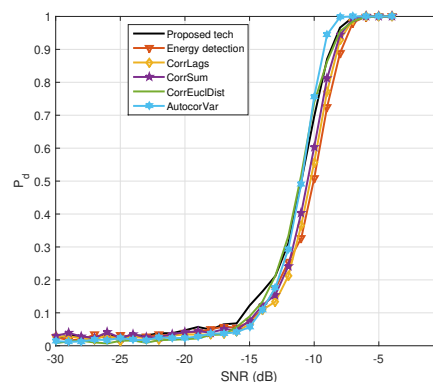
Fig. 3: The P_d versus SNR in case of a 4-QAM modulated signal when $P_{fa} = 0.01$.

reduces the range of impact that the selected threshold has on the target P_{fa}. The number of treated samples significantly affects sensing characteristics. As the number of processed samples rises, so does both the complexity of the technique and the sensing time, rendering the technique less feasible for implementation. In this study, we set the number of samples to 1000 and determined an optimal threshold value of 0.7. These selections ensure processing time aligns with network system requirements, where the desired probability of false alarm (P_{fa}) is maintained below 5%, the maximum acceptable value within network systems.

Figure 3 illustrates a comparison among various sensing techniques' probability of detection (P_d) with respect to Signal-to-Noise Ratio (SNR) variation, while keeping P_{fa} fixed at 0.01 and the number of samples at 1000. The effectiveness of the proposed method is contrasted with energy detection, correlation at lag_1, the Correlation Sum (lag_0 and lag_1, CorrSum), and the technique based on the variance of the autocorrelation coefficients (AutocorVar). The figure initially highlights the stability of the proposed autocorrelation-based sensing detection through the convergence of P_d to the target P_{fa} value under extremely low SNR conditions.
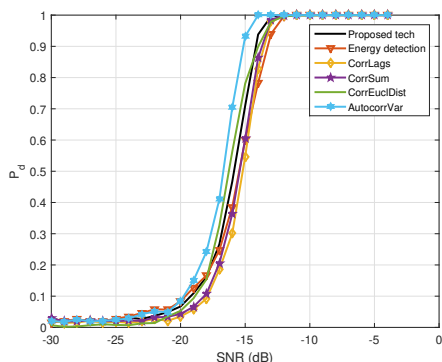
Fig. 4: The P_d versus SNR in case of a 8-PSK modulated signal when $P_{fa} = 0.01$.

Fig. 5: The practical experiment test-bed .

Figure 3 further emphasizes the superior detection capability of the proposed technique compared to all reference methods, with the exception of the technique based on the variance of autocorrelation function coefficients. This superiority is especially pronounced for the 4-QAM modulated signal. Importantly, across all communication system-required P_d values ($P_d \geq 0.9$), the SNR values corresponding to the proposed method consistently remain 1 dB lower than those associated with energy detection – a straightforward and extensively-used narrowband sensing approach.

Figure 4 illustrates the comparison between the probabilities of detection of the proposed method and those of the reference techniques as the signal-to-noise ratio (SNR) varies. The figure demonstrates that with increasing SNR, the detection probability (P_d) also increases. Furthermore, the figure highlights the superior detection performance of the autocorrelation average sensing technique compared to energy detection, correlation lags detection, and correlation sum-based sensing techniques. As an example, for all P_d values greater than or equal to 90%, the corresponding SNR values for the proposed method and energy detection are -14 dB and -13 dB, respectively, resulting in a detection improvement of 1 dB. Nevertheless, the AutocorVar approach exhibits the highest detection probability (P_d) when contrasted with all of these sensing methodologies. It is important to acknowledge that this method calculates a second-order statistical parameter derived from another second-order process, specifically the autocorrelation function.

V. RESULTS AND EVALUATIONS

This section provides the practice evaluation of the GNU Radio implementation of the proposed autocorrelation average based sensing technique. Where this method is implemented the radio FM broadcasting receiver and another floor for estimating the SNR.

A. Experimental test-bed setup

To validate the practical efficiency of the technique, experiments were conducted using a laptop equipped with the GNU Radio platform, along with an RTL-SDR dongle serving as a wireless receiver. The implementation of the SDR test-bed

was designed to evaluate the technique's sensing capabilities in real-world scenarios [5]. Figure 5 illustrates the configuration of the experimental setup for the proposed SDR test-bed. Leveraging the capabilities of the GNU Radio platform, wireless communication networks can be simulated and designed to closely resemble real systems. Additionally, the flexibility of the GNU Radio platform allows for the integration of various hardware components, including the RTL-SDR dongle, which is utilized in this implementation as an FM broadcasting receiver [12]. The RTL-SDR receiver was consistently tuned to a central frequency, providing coverage of the entire FM bandwidth ranging from 88 MHz to 108 MHz.

The system's implementation is structured across three tiers, as illustrated in Figure 6. The initial tier encompasses the reception and processing of radio broadcast signals, culminating in audio output via the loudspeaker (Audio Sink block). This stage also facilitates the adjustment of the central reception frequency of the RTL-SDR device, while enabling signal categorization into radio broadcast channel signals, radio broadcast side signals, or noise.

The second tier is dedicated to the sensing process, involving signal reception from the RTL-SDR dongle and subsequent processing through the sensing block (correlation avrlag block). The sensing block computes the average of the first three lags of the autocorrelation function for each 1000-sample set. This computed statistical parameter is then compared to a predefined threshold, yielding three outputs: the statistical parameter (lags mean), the threshold value, and the decision (1 or -1) denoting the presence or absence of a primary user signal.

Finally, the third tier focuses on estimating the signal-to-noise ratio (SNR), primarily utilizing the MPSK SNR Estimator block from the GNU Radio library. This stage aids in the analysis of detection results obtained through the proposed method. Notably, the presence of high-energy received signals does not guarantee accuracy, as these signals could originate from distortions. Conversely, low-energy received signals might exhibit high SNR values due to minimal interference.
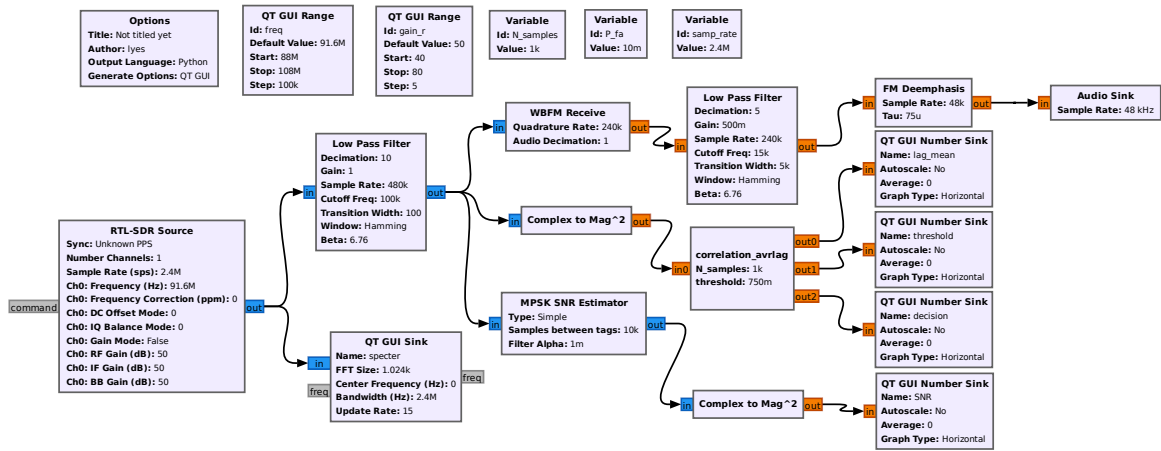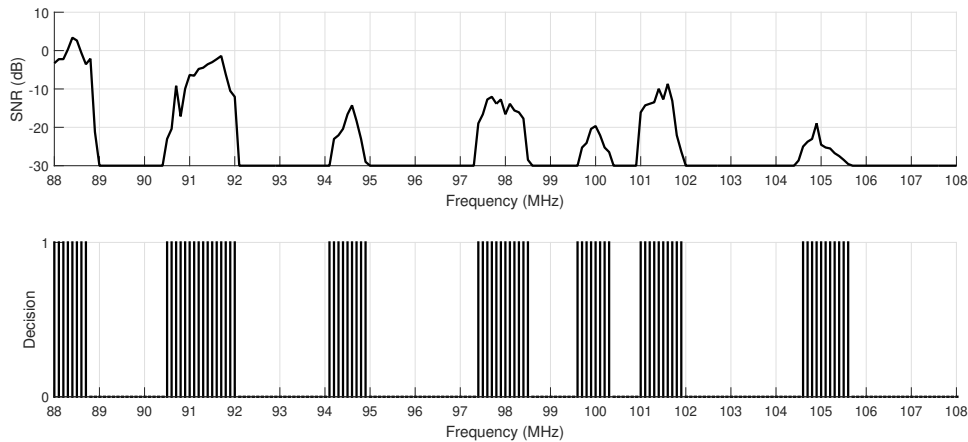
Fig. 6: GNU Radio flow-graph of the proposed autocorrelation average based sensing technique with the FM Receiver [4]

(a) The power spectrum density representation

(b) Sensing results

Fig. 7: The power spectrum density representation of the Radio FM broadcasting and the sensing decision for each FM channel

B. Practical results analysis

Figure 7 provides a comprehensive overview of the experimental results, encompassing Radio FM band spectrum scanning and analysis, SNR estimation, and practical sensing decisions. Subfigure 7a visually represents the energy intensity of received signals across the entire Radio FM spectrum, enabling the identification of varying energy levels within 200 KHz-wide FM channels.

Subfigure 7b comprises two significant curves. The first curve illustrates the signal-to-noise ratio (SNR) across all channels, determined through the MPSK SNR Estimator block. SNR values below -30 dB are capped at -30 dB, highlighting the characteristics of received signals and differentiating high-energy distortions from medium-to-low energy signals with comparatively higher SNR values. The second curve highlights practical sensing decisions, with a (1) denoting the presence of FM broadcasting in the respective channel, and a (0) indicating an unoccupied channel. This analysis reinforces the effectiveness of the correlation average-based sensing technique in detecting FM broadcasting activity.

While Subfigure 7a might suggest occupancy in only 6 frequency bands initially, a more detailed scrutiny of the SNR curve reveals the existence of 7 distinct frequency bands. These findings correlate with the detection outcomes of the proposed method. Notably, FM broadcasting activity around 100 MHz is less prominent in Subfigure 7a due to low received energy signals. However, this activity becomes evident in the curves of Subfigure 7b, despite the relatively weak SNR in this range. The audibility of this false broadcast activity from the loudspeaker (Audio Sink block) on the first tier further validates its presence.

VI. CONCLUSION

In this paper, a novel approach to spectrum sensing was presented, utilizing the average of the initial three autocorrelation lags. The aim was to tackle the issue of spectrum sensing limitations. The technique underwent preliminary simulations to both assess its sensing capacity and recognize its potential constraints. The simulation outcomes underscored the technique's exceptional detection proficiency, particularly in scenarios characterized by low Signal-to-Noise Ratio (SNR), outperforming various benchmark sensing techniques. However, it was worth noting that a notable limitation of this method lied in formulating the mathematical relationships required to establish an appropriate threshold, ensuring an acceptable level of probability of false alarm.

Furthermore, the simulations affirmed the superiority of the proposed approach by 1 dB compared to energy detection, both in environments involving (8-PSK) modulation and 4-QAM modulated received signals. Concluding the investigation, the implementation of the autocorrelation average-based sensing technique was demonstrated using the GNU Radio platform and the RTL-SDR dongle. The implementation underscored the simplicity of the technique and its efficient capability, as evidenced by the minimal sensing time required to detect rapid variations in radio FM broadcasting signals.

REFERENCES

[1] G. Ghosh, P. Das, and S. Chatterjee. Simulation and analysis of cognitive radio system using matlab. *International Journal of Next-Generation Networks*, 6(2):31–45, 2014.

[2] Y. Lee, T. Cheatham, and J. Wiesner. Application of correlation analysis to the detection of periodic signals in noise. *Proceedings of the IRE*, 38(10):1165–1171, 1950.

[3] J. Luo, G. Zhang, C. Yan, et al. An energy detection-based spectrum-sensing method for cognitive radio. *Wireless Communications and Mobile Computing*, 2022, 2022.

[4] L. Lyes, T. Djamal, and L. Nacerredine. Effective autocorrelation-based spectrum sensing technique for cognitive radio network applications. *International Journal of Communication Systems*, page e5502, 2023.

[5] A. Mate, K.-H. Lee, and I.-T. Lu. Spectrum sensing based on time covariance matrix using gnu radio and usrp for cognitive radio. In *2011 IEEE Long Island Systems, Applications and Technology Conference*, pages 1–6. IEEE, 2011.

[6] B. A. McGuire, R. A. Loomis, A. M. Burkhardt, K. L. K. Lee, C. N. Shingledecker, S. B. Charnley, I. R. Cooke, M. A. Cordiner, E. Herbst, S. Kalenskii, et al. Detection of two interstellar polycyclic aromatic hydrocarbons via spectral matched filtering. *Science*, 371(6535):1265–1269, 2021.

[7] J. Mitola and G. Q. Maguire. Cognitive radio: making software radios more personal. *IEEE personal communications*, 6(4):13–18, 1999.

[8] L. Pakula and S. Kay. Detection performance of the circular correlation coefficient receiver. *IEEE transactions on acoustics, speech, and signal processing*, 34(3):399–404, 1986.

[9] H. Reyes, S. Subramaniam, N. Kaabouch, and W. C. Hu. A spectrum sensing technique based on autocorrelation and euclidean distance and its comparison with energy detection for cognitive radio networks. *Computers & Electrical Engineering*, 52:319–327, 2016.

[10] R. K. Sharma and J. W. Wallace. Improved spectrum sensing by utilizing signal autocorrelation. In *VTC Spring 2009-IEEE 69th Vehicular Technology Conference*, pages 1–5. IEEE, 2009.

[11] K. Sherbin and V. Sindhu. Cyclostationary feature detection for spectrum sensing in cognitive radio network. In *2019 International Conference on Intelligent Computing and Control Systems (ICCS)*, pages 1250–1254. IEEE, 2019.

[12] R. Vuohtoniemi, J.-P. Mäkelä, J. Vartiainen, and J. Iinatti. Detection of broadcast signals in cognitive radio based plc using the fcme algorithm. In *18th IEEE International Symposium on Power Line Communications and Its Applications*, pages 70–74. IEEE, 2014.

Smarter Intersections with Cooperative Vehicular Visible Light Communication

Manuel Augusto Vieira, Manuela Vieira, Paula Louro, Gonçalo Galvão

DETC/ISEL/IPL,
R. Conselheiro Emídio Navarro, 1959-007
Lisboa, Portugal
NOVA School of Science and Technology, UNINOVA-CTS and LASI, NOVA University Lisbon
Quinta da Torre, Monte da Caparica, 2829-516, Caparica, Portugal
e-mail: mv@isel.pt, mv@isel- ipl.pt, plouro@deetc.isel.pt, A45903@alunos.isel.pt

Pedro Vieira
ADETC/ISEL/IPL,
R. Conselheiro Emídio Navarro, 1959-007
Lisboa, Portugal
Instituto das Telecomunicações
Instituto Superior Técnico, 1049-001,
Lisboa, Portugal
e-mail: pvieira@isel.pt

Abstract— **Our proposed system utilizes Vehicle-to-Vehicle, Vehicle-to-Infrastructure, and Infrastructure-to-Vehicle communications to create a Visible Light Communication system for managing vehicles crossing light-controlled intersections in a safe manner. The system leverages connected vehicles and infrastructure to exchange information through the use of headlights, streetlights, and traffic signals. In this system, transmitters emit light signals that are encoded, modulated, and converted from data. Optical sensors with light filtering properties serve as receivers and decoders, allowing them to capture and interpret the transmitted signals. To facilitate effective communication, a specific communication scenario is established. Concurrently, an intersection manager takes charge of coordinating traffic flow and interacts with vehicles using embedded Driver Agents. The system incorporates a dynamic phasing diagram based on the total accumulated time to illustrate the concept. The collected data demonstrates that the adaptive traffic control system in the V2X environment can gather detailed information, including vehicle position, speed, queue length, and stopping time. By dynamically controlling traffic flows at intersections, the system adjusts the durations of cycles based on traffic demands. This improved temporal management of phases results in smoother traffic flow and higher average speeds.**

Index Terms— *Traffic control; Reinforcement Learning; Vehicular Visible Light Communication; Cooperative Driving.*

I. INTRODUCTION

The primary objective of Intelligent Transport System (ITS) technology is to enhance traffic safety and efficiency on public roads by increasing situational awareness and mitigating traffic accidents through vehicle-to-vehicle (V2V) and vehicle-to-infrastructure (V2I) communications[1] [2] [3]. Inefficiencies in existing traffic light cycle control systems lead to problems such as long delays and energy wastage. To address these issues and improve efficiency, it is crucial to utilize real-time traffic information as input and dynamically adjust the duration of traffic lights accordingly. The ultimate goal is to enhance safety and increase the throughput of traffic intersections through cooperative driving [4][5].

This research specifically focuses on utilizing Visible Light Communication (VLC) as a means of transmitting information to provide guidance services and specific information to drivers. The objective is to decide the duration of traffic signals based on the data collected from VLC data transmission. VLC is an emerging technology [6][7] that enables data communication by modulating information on the intensity of light emitted by LEDs. In the context of vehicular communications, VLC becomes more accessible as all vehicles, streetlights, and traffic lights are equipped with LEDs, which are primarily used for illumination. By utilizing streetlamps, traffic signals, and the headlights and taillights of vehicles, communication and localization can be facilitated, allowing for the dual use of exterior automotive and infrastructure lighting for both illumination and communication purposes[8][9]. After the introduction, Section II introduces the scenario, environment, and architecture for cooperative guidance systems. In Section III, a proposal for Dynamic Traffic Phasing is presented, followed by an analysis of the Adaptive V-VLC in Section IV. Sections V and VI establish a correlation between experimental and simulated results. Finally, Section VII encapsulates the main conclusions drawn from the study.

A. Background Theory on Adaptive Traffic Control

As wireless communication technologies advance and V2V and V2I systems, known as Connected Vehicles (CV), are developed, there arises an opportunity to optimize the operation of urban traffic networks through cooperation between traffic signal control and driving behaviors. The adaptive traffic control strategy we propose aims to effectively respond to real-time traffic demand by utilizing current and predicted future traffic flow data modeling.

In comparison to the fixed coil detectors used in traditional traffic environments, the adaptive traffic control system in a V2X environment can collect more detailed

data. This includes not only traffic flow and occupancy information but also specific details such as vehicle position, speed, queuing length, and stopping time. By leveraging the capabilities of the V2X system, the adaptive traffic control system can gather comprehensive and granular data, providing a more accurate representation of the traffic situation [10][11]. This increased level of data granularity allows for more precise analysis and decision-making in traffic control. It enables the adaptive traffic control system to dynamically adjust signal timings, optimize signal phasing, and coordinate traffic flow based on real-time conditions and predicted future demand. By incorporating the detailed data provided by the V2X environment, the adaptive traffic control system can improve traffic efficiency, reduce delays, and enhance overall urban traffic network performance.

B. V-VLC Communication Link

A Vehicular VLC system (V-VLC) comprises a transmitter that generates modulated light and a receiver located in infrastructures and driving cars to detect the received light variation. Both the transmitter and receiver are connected through the wireless channel. In this system, the light produced by the LED is modulated using ON-OFF-keying (OOK) amplitude modulation [12]. The environment is defined by a cluster of square unit cells arranged in an orthogonal geometry. Different data channels are provided by tetra-chromatic white light (WLEDs) sources positioned at the corners of the square unit cells[13][14].

The input of the V-VLC system consists of coded signals sent by transmitters such as streetlights and headlights. These signals are intended to communicate with identified vehicles (I2V), traffic lights (V2I), or other vehicles (V2V). The input also includes the position of transmitters in the network and the steering angle (δ) to guide the driver's orientation along their path. To manage the passage of vehicles crossing the intersection, queue/request/response mechanisms and temporal/space relative pose concepts are employed. The coded signals are received and decoded by a PINPIN photodetector with light filtering properties.

C. Intelligent control system

In order to develop an intelligent control system model that facilitates safe vehicle management through intersections using V2V, V2I, and I2V communications, Reinforcement Learning (RL) concepts are utilized. RL is a training method that involves rewarding desired behaviors and/or punishing undesired ones [15] [16]. The simulations are agent-based and are conducted using a tool for Simulation of Urban MObility (SUMO) [17]. As the agent gains experience, it learns to avoid negative situations and focus on positive ones. The traffic lights in SUMO are controlled by the learning agent based on its decisions, and the overall flow of traffic is described while rewarding the actions of the traffic lights control agent. The agent's goal is to explore new states while maximizing its total reward to develop the best possible policy. A dynamic phasing diagram and a matrix of states based on the total accumulated time are presented to illustrate the concept.

II. SCENARIO, ENVIRONMENT AND ARCHITECTURE

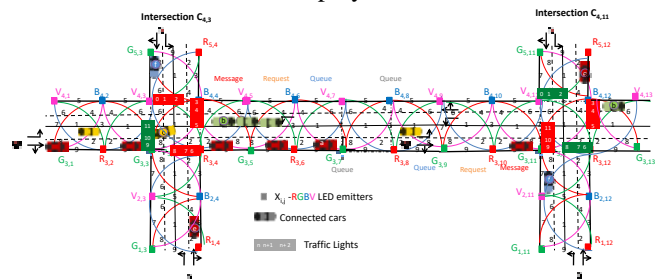In Figure 1, the scenario with two traffic signals controlled intersections is displayed.

Fig. 1. Simulated scenario with the optical infrastructure (X_{ij}), the generated footprints (1-9), the CV and the environment.

Based on clusters of square unit cells, an orthogonal topology was considered. Each transmitter, $X_{i,j}$, carries its own color, X, (Red, Green, Blue, Violet) as well as its horizontal and vertical ID position in the surrounding network (i,j). During the Proof of Concept (PoC), it was assumed that the crossroads are located at the intersections of line 4 with column 3 and column 11, respectively. In Figure 1, four traffic flows were considered. Twenty-four vehicles arriving from West (W): twenty red a_i Vehicles with straight movement and four yellow c_i Vehicles with left turn only. In the second flow green Vehicles from East (E) b_i approach the intersection with left turn only (thirteen straight and two left turn). In the third flow, six orange e_i Vehicles, oncoming from South (S), two have left-turn approach and four straight movement. Finally, in the fourth flow, thirteen blue f_i Vehicles coming from North, nine go straight and four have left turn in both intersections. Road request and response segments, offer a binary (turn left / straight or turn right) choice. According to the simulated scenario, each car represents a percentage of traffic flow. It is assumed that a_1, b_1, and a_2, make up the top three requests, followed by b_2, a_3, and c_1 in fourth, fifth and sixth place, respectively. In seventh, eighth and nineth request places are b_3, e_1 and a_3, respectively, followed in tenth place, by c_2. In penultimate request is a_5, and in the last one is f_1. According to our assumptions, 540 cars approach the intersection per hour, of which 80 percent come from east and west. Then, 50% of cars will turn left or right at the intersection and the other 50% will continue straight.

In the proposed system, a mesh cellular hybrid structure is utilized, as depicted in Figure 2. The "mesh" controller, situated at the streetlights, plays the role of forwarding messages to vehicles (I2V) within the mesh. It functions similar to router nodes in a network, facilitating communication between vehicles. On the other hand, the "mesh/cellular" hybrid controller acts as a border-router and

can also be employed for edge computing. This hybrid architecture allows for edge computing and device-to-cloud communication (I2IM), enabling the exchange of information. It leverages embedded computing platforms to perform a significant portion of processing tasks, while directly interfacing with sensors and controllers. This approach supports geo-distribution, local decision making, and real-time load balancing. By utilizing the mesh cellular hybrid structure, the system can effectively process and analyze data at the edge, enabling quicker response times and reducing the burden on central cloud infrastructure. Furthermore, this architecture promotes peer-to-peer communication (I2I), enabling direct information exchange between vehicles. This peer-to-peer communication enhances the efficiency of data sharing and collaboration among vehicles in the network.
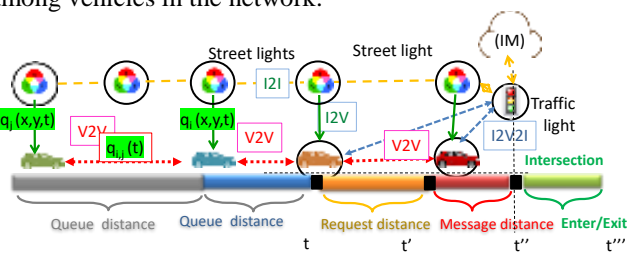

Fig. 2.   Representation of the Edge Computing infrastructure. Mesh and cellular hybrid architecture.

Emitters (street lights) are located along the roadside (Figure 1). Thus, each LED sends an I2V message that includes the synchronism, its physical ID and the traffic information. When a probe vehicle enters the streetlight´s capture range, the receiver replies to the light signal, and assigns a unique ID and a traffic message [15]. When approaching the intersection, it asks permission "request" to cross. An IM acknowledge is sent, "response" from the traffic signal over the facing receiver to the in-car application of the head vehicle. Once the response is received (message distance), the vehicle is required to follow the provided occupancy trajectories (footprint regions, see Figure 1). If a request has any potential risk of collision with all other vehicles that have already been approved to cross the intersection, the control manager only sends back to the vehicle (V2I) the "response" after the risk of conflict is exceeded. The vehicle speed can be calculated by measuring the actual travelled distance overtime, using the ID´s transmitters tracking, $q_i(x,y,t)$. For a vehicle with several neighboring vehicles, the mesh node uses the indirect V2V relative pose estimations, $q_{ij}(t)$ method taking advantage of the data of each neighboring vehicle [18].

III.   DYNAMIC TRAFFIC SIGNAL PHASING

Existing inefficient traffic light cycle control causes numerous problems, such as long delay and waste of energy. The traffic signal duration will be based on the collected data from V2V, V2I and I2V VLC communication. The traffic controller uses queue, request and response messages,

from the a_i, b_i, c_i, e_i and f_i vehicles, fusing the self-localizations $q_i(t)$ with their space relative poses $q_{ij}(t)$ to generate phase durations appropriate to accommodate the demand on each cycle. The following parameters are therefore needed to model the queuing system: The initial arrival time (t_0) and velocity (v_0) in each the occupied section. The initial time is defined as the time when the vehicles leave the previous section (queue, request or message distances) and move along the next section, $q_i(t, t')$. The service time is calculated using vehicle speed and distance of the section. The number of service units or resources is determined by the capacity of the section, $n(q_i (x,y, \delta, t))$ and vehicle speed which depends on the number of request services, and on the direction of movement along the lane $q_i(x, y, \delta, t)$. The maximum number of possible vehicles in the message distance is 4 by lane and 8 by route. So, a maximum of 32 vehicles are expected at the message distances (20 m) based on the stipulated average vehicle length (4.5 m). It was assumed that $t_{a1}<t_{b1}<t_{a2}<t_{b2}<t_{a3}<t_{c1} <t_{b3}<t_e<t_{a4}<t_{c2}<t_{a5}<t_f$. To each driving Vehicle, x_i, is assigned the unique time at which it must enter the intersection, $t''[x_i]$.

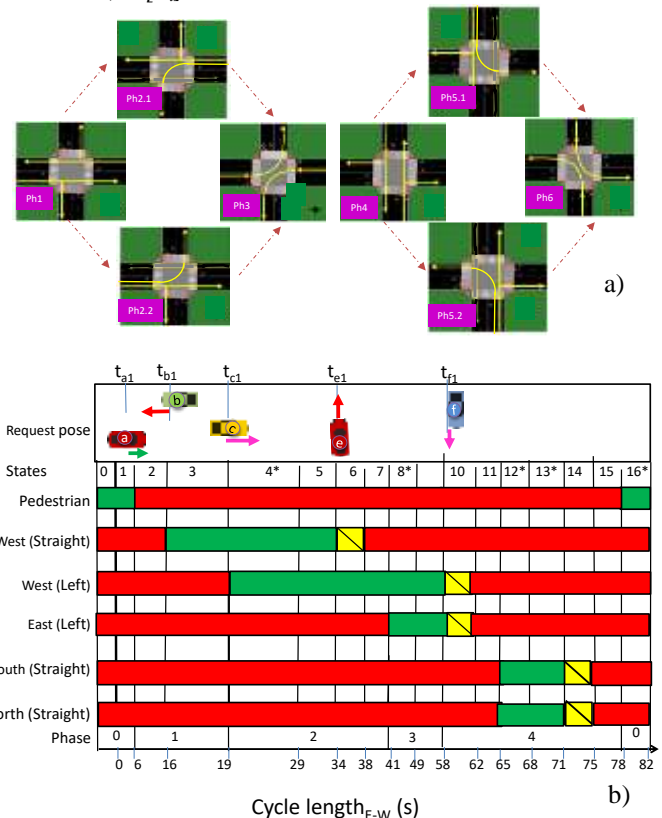Fig. 3.   a) Diagram of phases. b) Requested phasing of traffic flows ($t_{a1}<t_{b1}<t_{a2}<t_{b2}<t_{a3}<t_{c1} <t_{b3}<t_e<t_{a4}<t_{c2}<t_{a5}<t_f$). * Adaptive sequences.

The phase flow of the PoC intersection is shown in Figure 3b according to the phasing diagram assumed in Figure 3a. In this diagram, the cycle length is composed of 5 of the 7 phases contemplated   and divided in 16 time

sequences (states). The states marked with * are dynamic movable states that depends on the traffic demand during the cycle. The exclusive pedestrian phase contains the *"0"*, the *"1"* and the *"16"* sequences. The cycle's top synchronism starts with sequences *"1"*. The first, second, third, and fourth phases contain sequences between *"2"* and *"15"* and control traffic flow. The PoC assumes that all the leaders approach the intersection with similar velocities at different times (Figure 3b). Vehicle a_1 was the first to request to cross the intersection and informed IM about its position and also that four others follow it at their positions with their speeds. Phase 1, sequence 3, therefore, begins at $t'a_1$. Vehicle b_1 requests access later and includes the mappings of its two followers in its request. As the order to cross conflicts with a_i movement, he and his followers will pile up on the stop line increasing the total waiting time of the b_i cars. The fourth sequence is an adaptive sequence. Due to the presence of a medium E-W traffic scenario, the IM extends the green time in order to accommodate the passage of all the a_i followers as well as the simultaneous passage of the arriving c_i.

From the capacity point of view, it is more efficient, if Vehicle c_1 is given access (Phase 2) before Vehicles b_i, and Vehicle c_2 is given access before Vehicle e, forming a west left turn of set of vehicles (platoon) before giving way to the fourth phase with north and south conflicting flows. Meanwhile, the speed of Vehicle e was reduced, increasing the total accumulated time, r_t, in the S-N arm. Adaptive sequences 8 and 9 kick off Phase 3 and the sequence times will be adjusted according to the variation of waiting accumulated times for the left turn of the b_i cars. A new phase, Phase 4, begins and includes two adaptive sequences, sequence 12 and 13 also dependent on the accumulated waiting times of the N-S arms. Their time intervals will be as short as possible, which will free up capacity in the cycle for the E-W flows that are heavily loaded. Taking into account the accumulated total waiting time in each arm an 85-second cycle is recommended for this type of flow. The times associated with each sequence can be visualized in Figure 3.

IV. V-VLC ADAPTIVE TRAFFIC CONTROL

To code the information, an On-Off keying (OOK) modulation scheme was used, and it was considered a synchronous transmission based on a 64- bits data frame. Each infrastructure is equipped with white tetrachromatic LEDs, making it possible to transmit four signals simultaneously. So, all that is needed is a receiver that actively filters each of the channels, and a four-fold increase in bandwidth is possible. Each of the RGBV signals sent has calibrated amplitude that defines it. Because each VLC infrastructure has four independent emitters, the optical signal generated in the receiver can have one, two, three, or even four optical excitations, resulting in 2^4 different optical combinations and 16 different photocurrent levels at the photodetector [15]. Filtering is achieved by the PINPIN

demultiplexer, which receives the combined OOK signal and through prior knowledge of the calibrated amplitudes is able to decode the sent message. As an example, in in Figure 4 Vehicle c_1 (Figure 1), receives three MUX signals as it crosses the intersection during Phase2.This vehicle, driving on the left lane (#8 E), was the sixth to ask permission to cross the intersection it receives order to enter the intersection in pose # 8E, turns left (#1NE) and keeps moving in this direction across position #1 toward the North exit (#4N). In the right side, the received channels are identified by its 4-digit binary codes and associated positions in the unit cell. On the top the transmitted channels packets [R, G, B, V] are decoded. The environment is also inserted to guide the eyes.
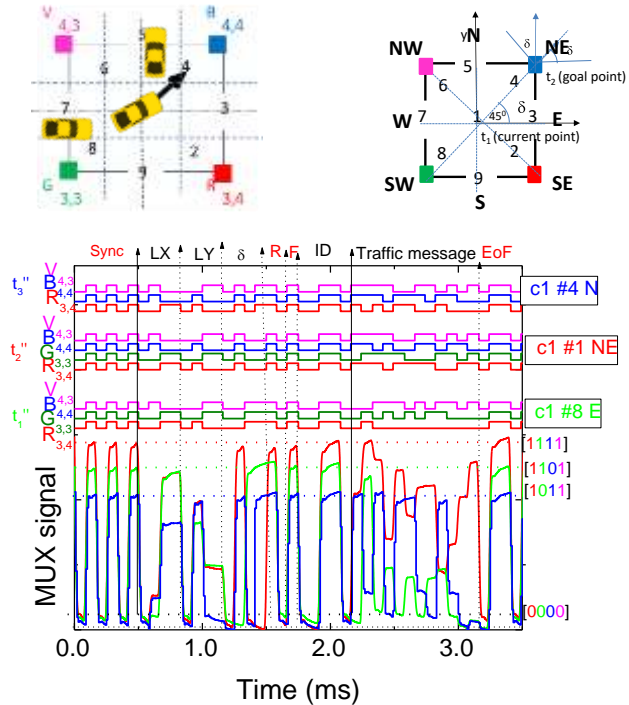

Fig. 4. MUX signals and assigned decoded poses inside intersection 1 acquired by vehicle c_1, entering (t_1'), crossing (t_2') and exit (t_3'). On the top the transmitted channels packets [R, G, B, V] are decoded. The insert visualizes the environment.

As exemplified in the top part of Figure 4, the frame is divided into several blocks. The first block is the synchronization block. The synchronism always considers the same sequence of bits for all transmitters in a pattern [10101], having as a second purpose the identification of the maximum possible amplitude at reception. By knowing the maximum amplitude received it is possible to identify the footprint region [15]. With this information and with the help of the calibration signal, the location of the vehicle in its cell is defined. The next two blocks, gives the location (*x, y* coordinates) of the emitters inside the array ($X_{i,j}$). Cell's IDs are encoded using a 4 bits binary representation for the decimal number. The δ block (steering angle (δ)) completes the pose in a frame time $q(x, y, \delta, t)$. Eight coded steering

angles along the cardinal points gives the car direction. The next block (R) identifies the message type, which can be a "request" [00], a "response" [01] or another message type. The Flag (F) is a bit indicating whether there is vehicle identification in the following bits or not. Its purpose is to alert the decoder that the following bit sequence corresponds to the vehicle identification rather than the payload. ID block is the temporary identification of the vehicle, decided and provided by the infrastructure on the "response" message and order the request message at the intersection. Here, 5 bits are considered because a maximum of 32 vehicles per lane (8 routes, 4 lanes) are expected at message distance (20 m). The last is the traffic message. It is the body of the message, and may include other information such as the road condition, average-waiting time, and weather conditions, among others. EoF Bit or sequence of bits defines the end of the frame. In this case, the sequence [0110] was considered.

V. DYNAMIC TRAFFIC FLOW CONTROL SIMULATION

The considered environment for SUMO simulation (Figure 1), is a 4-way intersection, 2 lanes on each arm approach the intersection from compass directions, leaving 2 lanes on each arm. Each arm is 100 meters long. On every arm, each lane defines the directions that a vehicle can follow. In both intersections, a traffic light system, controlled by the IM (also known as agent), manages the approaching traffic.

Figure 5, illustrates the state representation for the west arm of the intersections at specific time points. Each lane has a dedicated traffic light labeled TL/0-15. The state representation segregates the arm into discrete "response", "request", and "queue" cells. In total, there are 4 cells (0/message, 1/request, 2,3/queues) per lane (L/0-7), resulting in a total of 32 state cells during the simulation.

During the simulation, an array contains information about all vehicles present at a given time, with states assigned to them. The state of a vehicle, denoted as $"v_i,"$ where i represent the order of the crossing request, consists of a two-digit string. The first digit represents the lane the vehicle is in, while the second digit represents its position within that lane. For example, the state of the leader vehicle a1 in lane L0 would be represented as $v_1="00"$, and the state of the leader vehicle b_1 in lane L4 would be represented as $v_2="50"$.
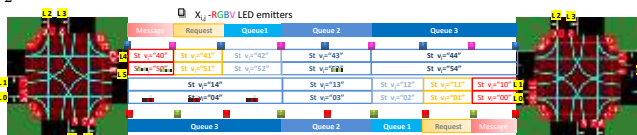

Fig. 5. State representation for the west arm of the intersections. Traffic Lights' (TL; 0-15), Lanes (L ;1-7.) Agent states (s_t) representation.

The training process is divided into multiple episodes, typically exceeding 100 episodes. Actions (Figure 3a) are performed when the traffic light system activates a set of lanes for a predetermined time during green phases. The yellow phase lasts four seconds, while the green phase lasts eight seconds. If the current action matches the previous action, there is no yellow phase, and the current green phase continues. However, if the current action differs from the previous one, a 4-second yellow phase occurs between the two actions. The reward, denoted as r, represents the environment's response to the agent's decision. The reward is based on a traffic efficiency metric, allowing the agent to assess whether the action taken improves or hampers intersection efficiency. In the presented scenario (Figure 1), the IM receives access requests to the intersection from leading vehicles at different times (t_{x1}, Figure 3). This V2I information provides the IM with precise location and speed data of all leading vehicles, as well as the location and speed of their followers obtained through V2V communication. This data helps the IM anticipate the initial arrival times and speeds at various sections, facilitating traffic coordination.

VI. ADAPTIVE V-VLC TRAFFIC CONTROL EVALUATION

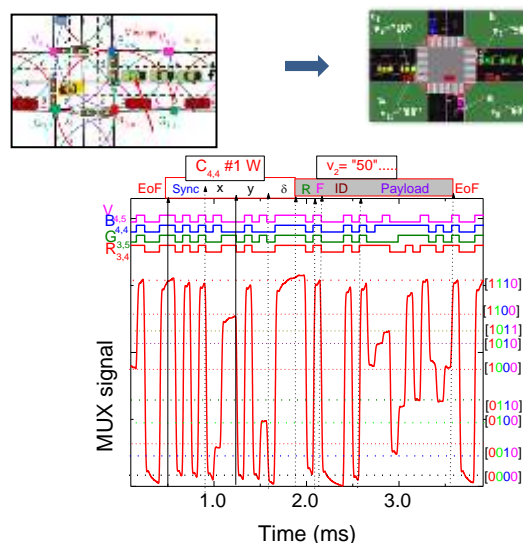To exemplify the process, in Figure 6 it is displayed a response to leader vehicle b_1 at t_{b1}.

Fig. 6. Normalized MUX signal and the assigned and decoded messages acquired by vehicles b_1. Pose C_{44}, #1W.

As far as circulation is concerned, the vehicles are all moving at an average of 10 m/s, dropping the speed to 5 m/s when reaching the traffic light at the beginning of the cycle, during pedestrian eviction. Considering this speed, approximately three seconds of green light are estimated to be required for each vehicle to drive through the traffic light. Taking into account Figure 1 a state diagram resulting from the SUMO simulation was generated and presented in Figure 7. Essentially, the result demonstrates the feasibility and benefit of creating a dynamic system that adapts to specific traffic scenarios. It is important to improve the coding techniques, in the future, in order to allow only the legitimate receivers to process secure request/response

messages. Here, the security is embedded in the physical transmission. In the LoS channel no information can be made available by the eavesdropper, i.e., he is completely passive.
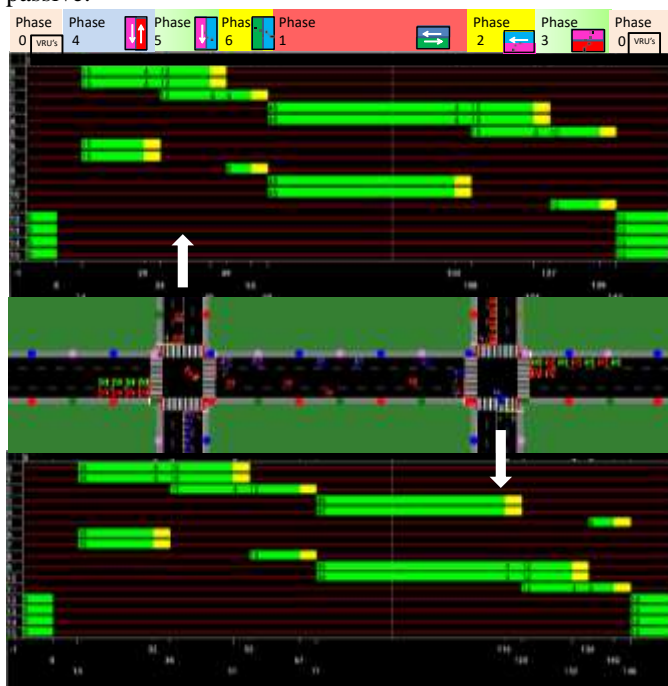

Fig. 7.   State diagram resulting in two coordinated intersections. On the top an insert of environment and the color phasing is inserted.

VII.   CONCLUSIONS

The integration of V-VLC technology with connected cars has optimized the operation of urban traffic networks by combining traffic signal control with driving behavior. A queue/request/response approach is employed for managing intersections, facilitated by V-VLC communications. This system enables real-time monitoring of queues, requests, and messages, along with the synchronization of traffic routing in different routes based on travel times.

To demonstrate the concept, architecture, scenario, and environment were developed. A phasing diagram is proposed to illustrate the traffic control process. A simulation using an urban mobility simulator was conducted, showcasing the benefits of adaptive traffic control. For future work, expanding upon this study could involve refining the developed architecture, scenario, and environment, further validating the proposed phasing diagram's efficacy in real-world traffic control, and exploring advanced simulation techniques to delve deeper into the advantages of adaptive traffic control.

ACKNOWLEDGMENT

REFERENCES

[1] Elliott, D., Keen W., and Miao L., "Recent advances in connected and automated vehicles" Journal of Traffic and Transportation Engineering, Vol. 6, Issue 2, pp.109-131(April 2019).

[2] Jitendra, N., and Bajpai, "Emerging vehicle technologies & the search for urban mobility solutions, Urban, Planning and Transport Research, 4:1, pp.83-100, (2016).

[3] Wang, N., Qiao, Y., Wang, W., Tang, S. and Shen, J. "Visible Light Communication based Intelligent Traffic Light System: Designing and Implementation,"2018 Asia Communications and Photonics Conference (ACP) DOI: 10.1109/ACP.2018.8595791(2018).

[4] Cheng, N. et al. "Big data driven vehicular networks," IEEE Network, vol. 32, no. 6, pp.160–167, (Nov. 2018).

[5] Singh, P., Singh, G., and Singh, A., "Implementing Visible Light Communication in intelligent traffic management to resolve traffic logjams" Int. J. Comput. Eng. Res, 5(9), pp.1-5 (2015).

[6] O'Brien, D. et al. "Indoor Visible Light Communications: challenges and prospects," Proc. SPIE 7091, 709106, pp. 60-68 (2008).

[7] Parth. H., Pathak, X., Pengfei, H. and Prasant, M.,"Visible Light Communication, Networking and Sensing: Potential and Challenges," September 2015, IEEE Communications Surveys & Tutorials 17(4): Fourthquarter 2015, pp. 2047 – 2077 (2015).

[8] Nawaz, T., Seminara, M.,, Caputo, S., Mucchi, L. and Catani, J. ''Low-latency VLC system with Fresnel receiver for I2V ITS applications,'' J. Sensor Actuator Netw., vol. 9, no. 3, p. 35 (Jul. 2020).

[9] Caputo, S., et al. ''Measurement-based VLC channel characterization for I2V communications in a real urban scenario,'' Veh. Commun., vol. 28, Apr. 2021, Art. no. 100305.

[10] Pribyl, P., Pribyl, M., Lom, and Svitek, M., ''Modeling of smart cities based on ITS architecture,'' IEEE Intell. Transp. Syst. Mag., vol. 11, no. 4, pp. 28–36 (Nov. 2019).

[11] Miucic, R. "Connected Vehicles: Intelligent Transportation Systems." Cham, Switzerland: Springer (2019).

[12] Vieira, M. A., Vieira, M., Louro, P., Vieira, P., "Bi-directional communication between infrastructures and vehicles through visible light," Proc. SPIE 11207, Fourth International Conference on Applications of Optics and Photonics, 112070C (3 October 2019); doi: 10.1117/12.2526500 (2019).

[13] Vieira, M. A., Vieira, M., Louro, P., Vieira, P. "Cooperative vehicular visible light communication in smarter split intersections," Proc. SPIE 12139, Optical Sensing and Detection VII, 1213905 (17 May 2022); doi: 10.1117/12.2621069.

[14] Vieira, M. A., Vieira, M., Vieira, P. and Louro, P., "Optical signal processing for a smart vehicle lighting system using a-SiCH technology," Proc. SPIE 10231, Optical Sensors 2017, 102311L (2017).

[15] Junping Zhang, Fei-Yue Wang, Kunfeng Wang, Wei-Hua Lin, Xin Xu, and Cheng Chen. Data-driven intelligent transportation systems: A survey. IEEE Transactions on Intelligent Transportation Systems, 12(4):1624–1639, 2011.

[16] Liang, X., Du, X., Wang, G., and Han, Z., "A Deep Reinforcement Learning Network for Traffic Light Cycle Control," in IEEE Transactions on Vehicular Technology, vol. 68, no. 2, pp. 1243-1253, Feb. 2019, doi: 10.1109/TVT.2018.2890726.

[17] Alvarez Lopez et al., " Microscopic Traffic Simulation using SUMO. In: 2019 IEEE Intelligent Transportation Systems Conference (ITSC), pp. 2575-2582. IEEE. The 21st IEEE International Conference on Intelligent Transportation Systems, 4.-7. Nov. 2018, Maui, USA.

[18] Vieira, M. A., Vieira, M., Louro, P., and Vieira, P., "Cooperative vehicular communication systems based on visible light communication" Opt. Eng. 57(7), 076101 (2018).

Self-location, Routing and Navigation Through Visible Light Communication

Manuela Vieira, Manuel Augusto Vieira, Paula Louro,
Alessandro Fantoni
DETC/ISEL/IPL,
R. Conselheiro Emídio Navarro, 1959-007
Lisboa, Portugal
NOVA School of Science and Technology, UNINOVA-
CTS and LASI, NOVA University Lisbon
Quinta da Torre, Monte da Caparica, 2829-516,
Caparica, Portugal
e-mail: mv@isel.pt, mv@isel- ipl.pt, plouro@deetc.isel.pt,
afantoni@deetc.isel.pt

Pedro Vieira
ADETC/ISEL/IPL,
R. Conselheiro Emídio Navarro, 1959-007
Lisboa, Portugal
Instituto das Telecomunicações
Instituto Superior Técnico, 1049-001,
Lisboa, Portugal
e-mail: pvieira@isel.pt

Abstract— **The paper describes an approach that utilizes Visible Light Communication (VLC) to generate landmark route and alert instructions for supporting people's wayfinding activities. The system consists of multiple transmitters, which are ceiling luminaries that transmit map information, alerts, and path messages necessary for wayfinding. Optical receivers are used to collect this information. The system operates in real time, providing users with the most optimal route to their destination, thereby helping them avoid congested areas. The transmitters employ tetrachromatic identifier white sources, which serve the dual purpose of providing lighting and different data channels for each chip. The data is encoded, modulated, and converted into light signals. By employing joint transmission, mobile optical receivers can capture data at high frame rates, determine their own location, and simultaneously read transmitted data from each transmitter. The communication is bidirectional, allowing users to interact with the received information. The system calculates the best route through the venue, taking into account static or dynamic destinations. Additionally, the paper mentions the consideration of buddy wayfinding services. According to the results presented, the system not only enables self-location but also deduces the travel direction and interacts with the received information. This optimization process helps users navigate efficiently towards their desired destination, whether it is a static or dynamic location.**

Index Terms— Visible Light Communication; Geolocation; Indoor navigation; Bidirectional Communication; Wayfinding; Optical sensors; Transmitter/Receiver.

I.   INTRODUCTION

Navigation systems have traditionally relied on Global Positioning System (GPS) for outdoor positioning, providing users with direct and shortest routes based on their current location and intended destination. However, when it comes to indoor navigation, GPS is not suitable due to the difficulty of satellite signals penetrating buildings' roofs, tunnels, or floors. This limitation has led to the development of alternative indoor positioning systems based on various radio technologies.

One commonly used technology for indoor positioning is Wi-Fi. Wi-Fi signals can be utilized to estimate a user's location within a building by measuring signal strengths from multiple access points. By comparing these measurements, the system can determine the user's position. Bluetooth is another technology used for indoor positioning. Bluetooth beacons or tags placed strategically within a building emit signals that can be detected by users' devices. The strength and proximity of these signals allow the system to calculate the user's position. Radio-Frequency Identification (RFID) [1][2] is also employed in some indoor positioning systems. RFID tags attached to objects or worn by users emit radio signals that can be detected and used for determining location. Visible Light Communication (VLC) [3] is a relatively newer technology used for indoor positioning. As mentioned, VLC can be utilized to transmit data, including map information and path messages, to aid in wayfinding activities. VLC systems use light signals emitted by transmitters and collected by optical receivers to determine the user's location and provide navigation instructions. These radio-based technologies provide alternatives to GPS for indoor positioning and have been employed in various indoor navigation systems. Each technology has its own advantages and limitations, and the choice of technology depends on factors such as the specific use case, accuracy requirements, and infrastructure availability. In order to solve the contradiction between the explosive growth of data and the consumption of spectrum resources, VLC has become the development direction of the next generation communication network with its huge spectrum resources, high security, low cost, and so on [4][5].

Visible light can be used as an Identifier (ID) system and can be employed for identifying the building itself. The main idea is to divide the service area into spatial beams originating from the different ID light sources and identify each beam with a unique timed sequence of light signals. The signboards, based on arrays of LEDs, positioned in strategic directions [6], can be modulated acting as down- and up-link channels in the bidirectional communication. For the consumer services, the applications are enormous. Positioning, navigation, security and even mission critical

services are possible use cases that should be implemented. VLC is a data transmission technology that can easily be employed in indoor environments since it can use the existing LED lighting infrastructure with simple modifications [7] [8]. The use of white polychromatic LEDs offers the possibility of Wavelength Division Multiplexing (WDM), which enhances the transmission data rate. A WDM receiver based on tandem a-SiC:H/a-Si:H pin/pin light-controlled filter can be used [9] [10] to decode the received information. Here, when different visible signals are encoded in the same optical transmission path, the device multiplexes the different optical channels, performs different filtering processes (amplification, switching, and wavelength conversion) and finally decodes the encoded signals recovering the transmitted information.

In this paper, a VLC based guidance system to be used by mobile users inside large buildings is proposed. After the Introduction, in Section 2, a model for the system is proposed and the communication system described. In Section 3, the main experimental results are presented, downlink and uplink transmission is implemented and the best route to navigate calculated. In Section 4, the conclusions are drawn.

II. SYSTEM MODEL

The main goal is to specify the system conceptual design and define a set of use cases for a VLC based guidance system to be used by mobile users inside large buildings.

A. Background Theory

The system model consists of two main modules: the transmitter and the receiver, as depicted in Figure 1.
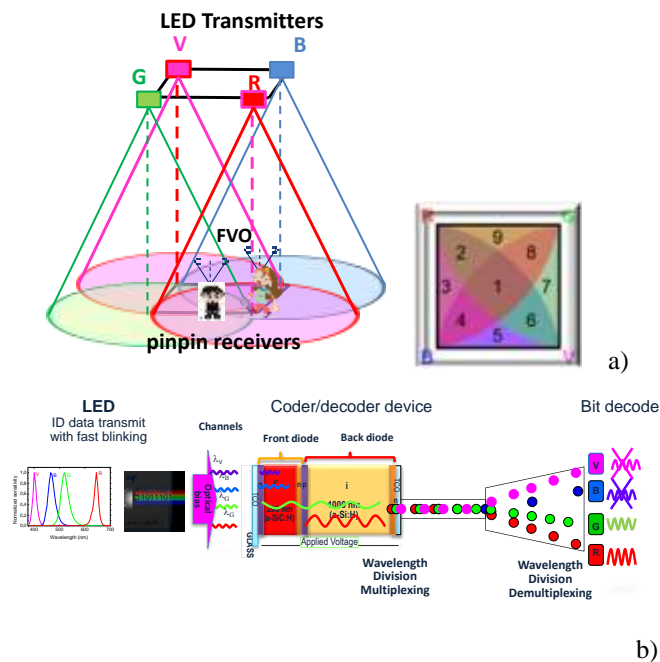

a)

b)

Fig. 1. a) Transmitters and receivers 3D relative positions and footprints in the square topology. b) Configuration and operation of the pin/pin receiver.

The transmitter module is responsible for converting data from the sender into an intermediate data representation in byte format. This byte-format data is then converted into light signals emitted by the transmitter. To achieve this, the data bit stream is input to a modulator, which utilizes an ON-OFF Keying (OOK) modulation scheme. The OOK modulation modulates the light signal to represent the digital data being transmitted. On the transmission side, the digital data is converted into analog data, and a modulation process takes place. The driver circuit will keep an average value (DC power level) for illumination, combining it with the analog data intended for communication. The visible light emitted by the LEDs passes through the transmission medium and is then received by the MUX device.

To realize both the communication and the building illumination, white light tetra-chromatic sources (WLEDs) are used providing a different data channel for each chip. The transmitter and receiver relative positions are displayed in Figure 1a. Each luminaire is composed of four polychromatic WLEDs framed at the corners of a square. At each node, only one chip is modulated for data transmission (see Figure 1a), the Red (R: 626 nm, 25 μW/cm^2), the Green (G: 530 nm, 46 μW/cm^2), the Blue (B: 470 nm, 60 μW/cm^2) or the Violet (V, 400 nm, 150 μW/cm^2). A fundamental difference between VLC and regular radio frequency (RF) communication is that VLC does not allow amplitude or phase modulation, and it must encode information by varying emitted light intensity. The LED can be dimmed ("off") when transmitting data bit '0' and at its maximum brightness ("on") when transmitting data bit '1'. This way, digital data is represented by the presence or absence of a carrier wave. The signal is propagating through the optical channel, and a VLC receiver, at the reception end of the communication link, is responsible to extract the data from the modulated light beam. In the receiving system, a MUX photodetector acts as an active filter for the visible spectrum. The integrated filter consists of a p-i'(a-SiC:H)-n/p-i(a-Si:H)-n heterostructure with low conductivity doped layers [10] as displayed in Figure 1b. It transforms the light signal into an electrical signal that is subsequently decoded to extract the transmitted information. The obtained voltage is then processed, by using signal conditioning techniques (adaptive bandpass filtering and amplification, triggering and demultiplexing), until the data signal is reconstructed at the data processing unit (digital conversion, decoding and decision) [11] [12]. At last, the message will be output to the users. In order to receive information from several transmitters, the receiver must position itself so that the circles corresponding to the range of each transmitter overlap. This results in a multiplexed (MUX) signal that acts both as a positioning system and as a data transmitter. The grid sizes were chosen to avoid overlap in the receiver from adjacent grid points. The nine possible overlaps (#1-#9), defined as fingerprint regions are also pointed out for the unit square cell, in Figure 1a.

B. Lighting Plan layout and Building model

In VLC geotracking, geographic coordinates are generated to provide location information. However, the

usefulness of this feature is further enhanced by using these coordinates to determine meaningful locations within a building and guide users through unfamiliar spaces or towards specific destinations, such as meeting rooms. To facilitate this process, VLC employs cells for positioning and a Central Manager (CM) that oversees and manages the entire system, including generating optimal routes. In Figure 2 the 3D building model is depicted.
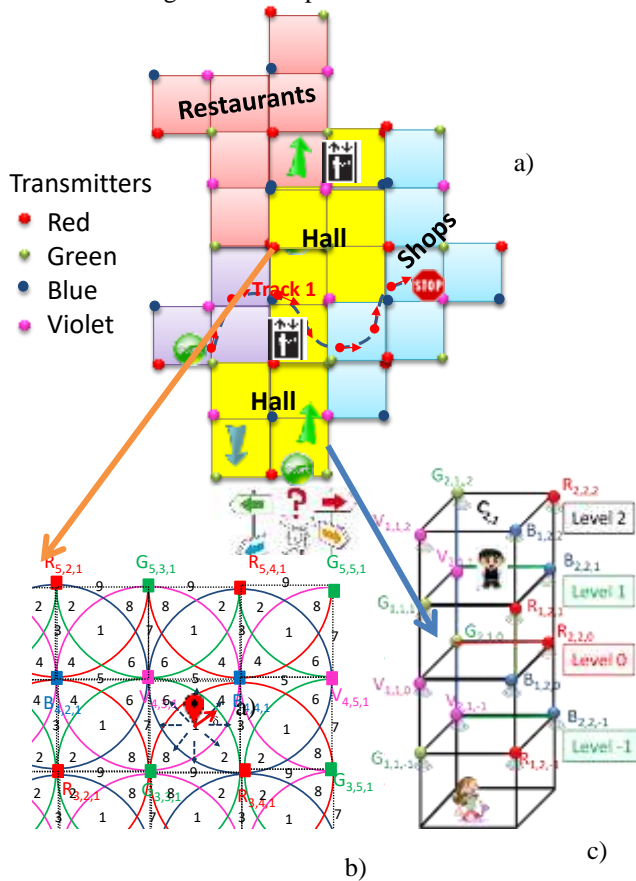

Fig. 2. a) Indoor layout and proposed scenario. b) Clusters of cells in square topology. c) 3D optical scenario (RGBV).

Building a geometry model of buildings' interiors is complex. A square lattice topology was considered for each level [13]. A user navigates from outdoor to indoor (Figure 2a). This topology is represented using x, y and z axes to simplify the distance between any pair of nodes. Each room/crossing/exit represents a node, and a path as the links between nodes. The user positions can be represented as P (x, y, z) by providing the horizontal positions (x, y) and the correct floor number z. The ground floor is level 0 and the user can go both below (z<0) and above (z>0) from there. Lighting in large environments is designed to illuminate the entire space in a uniform way. Ceiling plans for the LED array layout, in floor 1 is shown in Figure 2b. Each node emits light all around it and up to a certain range, which allows each cell to be divided into nine footprints depending on which LEDs are covering any given space (Figure 2b), thus allowing the system to determine the position of a user

or device in any given cell, $q(x,y,z,\delta)$. δ is one of the eight possible steering angles (arrows along the cardinal points in Figure 2b) and guides the user across his path. The 3D model generation is based on footprints of a multi-level building that are collected from available sources (luminaires), and are displayed on the user receiver for user orientation. It is a requirement that the destination can be targeted by user request to the CM and that floor changes are notified. Each unit cell can be referred as $C_{i,j,k}$ were i, j, k are the x, y position in the square unit cell of the top left node and k the floor level.

C. Architecture and Geolocation

Fog/Edge computing is a paradigm that brings computing capabilities closer to IoT devices by utilizing network nodes in the proximity of these devices. It enables tasks such as computing, storage, networking, and data management to be performed on these nodes, thereby reducing latency and bandwidth usage by offloading processing from the cloud.

A mesh cellular hybrid structure is proposed and displayed in Figure 3. This architecture consists of VLC-ready access equipment, that provides the computing resources, end devices, and a controller that is in charge of receiving service requests and distributing tasks to fog nodes.
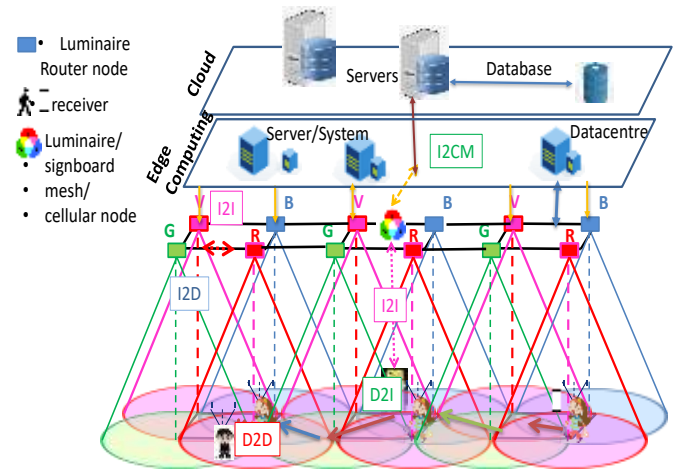

Fig. 3. Mesh and cellular hybrid architecture.

A user moves from outdoor to indoor and requests assistance in finding the right track (D2I). They can customize their points of interest for wayfinding services. The requested information (I2D) is sent by the emitters, at the ceiling, to its receiver. This architecture serves two purposes: enabling edge computing and device-to-cloud communication, and enabling peer-to-peer communication for information exchange.

Under this architecture, the short-range mesh network purpose is twofold: enable edge computing and device-to-cloud communication, by ensuring a secure communication from a luminaire controller to the edge computer or datacenter (I2CM), through a neighbor luminaire/signboard controller with an active cellular connection; and enable peer-to-peer communication (I2I), to exchange information.

Each WLED emits a unique VLC signal for identification, and the optical receiver calculates the user's track using this information and a position algorithm The indoor route (track; $q(x, y, z, \delta, t)$) is presented to the user via messages (I2D) transmitted by the ceiling luminaires acting as routers or mesh/cellular nodes.

III. COOPERATIVE GUIDANCE SYSTEM

Cooperative guidance systems enhance navigation accuracy by integrating data from multiple sources for seamless and reliable guidance.

A. Communication protocol, coding/decoding techniques

To code the information, an OOK modulation scheme was used, and it was considered a synchronous transmission based on a 64- bits data frame. The frame is divided into three main blocks (Sync, Navigation data and Payload) as displayed in the top of Figure 4 where a received MUX signal is displayed and decoded.

TABLE 1. FRAME STRUCTURE

Header	Navigation Data						Payload	
Synch	x	y	z	pin$_1$	pin$_2$	δ	Wayfinding data	Stop bit
5 bits (10101)	24 bits (4 bits per field)						34 bits (…….)	1 bit (0)
Frame length = 64 bits								

The header block is the synchronization block [10101]. This first block refers to the starting bit sequence that is repeated in every data frame and allows the receiver to determine from an array of incoming bits where each frame begins. For this purpose, the same header bit sequence is imposed simultaneously to all emitters, in this case in an alternating "on"- "off" pattern [10101]. The second block contains the ID, 4+4+4 bits, gives the geolocation (x,y,z coordinates) of the emitters inside the array ($X_{i,j,k}$). These IDs were encoded using a 4-bit binary representation for the decimal number. The z coordinate refers to the floor number, which can be negative thus the first bit is used to represent the floor number's sign ('0' when a positive number, '1' when a negative number) and the remaining three bits indicating the coordinate's value. When bidirectional communication is required, the user must register by choosing a username (pin$_1$) with 4 decimal numbers, each one associated to a RGBV channel. If buddy friend services are required a 4-binary code of the meeting (pin$_2$) must be inserted. The δ block (steering angle (δ)), a 4-bit sequence, completes the user's pose in a frame time q(x,y, δ, t). Eight steering angles along the cardinal points are possible from a start point to the next goal as pointed out as dotted arrows in Figure 2. The codes assigned to the pin$_2$ and to δ are the same in all the channels. If no wayfinding services are required these last three blocks are set at zero and the user only receives its own location. The third and final block is named the payload and refers to sequence of bits that is not necessary for the navigation service. It is made up of

miscellaneous data and followed by a stop bit. Using the photocurrent signal measured by the photodetector, it is necessary to decode the received information. A calibration curve is previously defined to establish this assignment [14].The calibration curve refers to a sequence of bits that, when received, is purposefully meant to reach each of the possible decoding levels. calibration curve (MUX signal) make use of 16 distinct photocurrent thresholds which correspond to a bit sequence that allows all the sixteen combinations of the four RGBV input channels (2^4). If the calibrated levels (d_0-d_{15}) are compared to the different four-digit binary codes assigned to each level, then the decoding is obvious, and the message may be read [14].
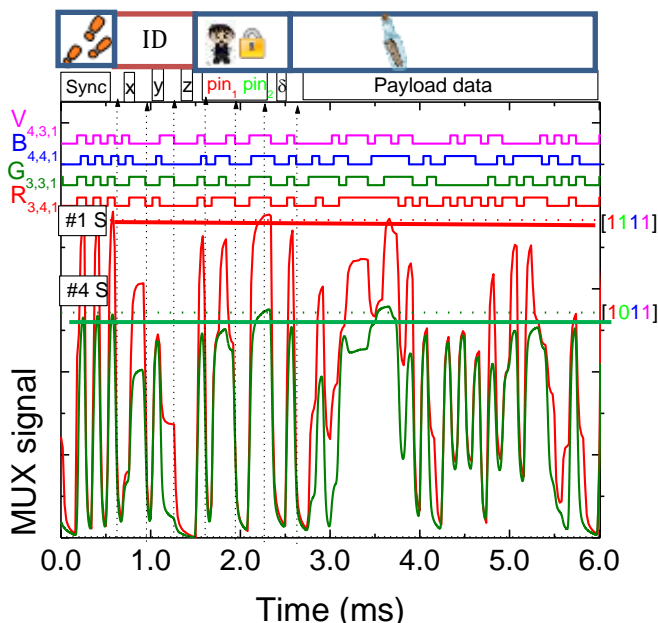

Fig. 4. MUX signals. On the top the transmitted channels packets are decoded [R, G, B, V].

The footprint position comes directly from the synchronism block, where all the received channels are, simultaneously, *on* or *off*. The binary code from the higher amplitude (horizontal lines in Figure 4) gives the received channel. So, two different signals were received by user "7261" at footprints #1 [1111] and # 4 [1011]. The next block of 12 bits gives de ID of the received nodes $R_{3,4,1}$, $G_{33,1}$, $B_{44,1}$ and $V_{4,3,1}$ (#1) or $R_{3,4,1}$, $B_{44,1}$ and $V_{4,3,1}$ in #4. Then the user code (pin1/"7261") and the meeting code (pin2/"3") as well as the steering angle (δ/S) are decoded . The last block is reserved for the transmission of the wayfinding message.

B. Fine-grained indoor localization, navigation and route control

In Figure 5, the MUX received signal and the decoding information that allows the VLC geotracking and guidance in successive instants (t_0, t_1, t_2) from user "7261" guiding

him along his track is exemplified. The visualized cells, paths, and the footprints are also shown as inserts.
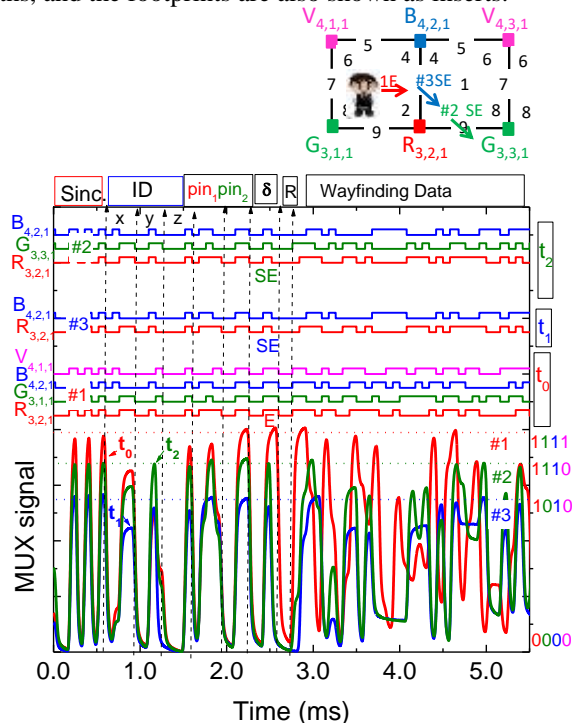

Fig. 5. Fine-grained indoor localization and navigation in successive instants. On the top the transmitted channels packets are decoded [R, G, B, V].

Data shows that at t_0 the network location of the received signals is $R_{3,2,1}$, $G_{3,1,1}$, $B_{4,2,1}$ and $V_{4,1,1}$, at t_1 the user receives the signal only from the $R_{3,2,1}$, $B_{4,2,1}$ nodes and at t_2 he was moved to the next cell since the node $G_{3,1,1}$ was added at the receiver. Hence, the mobile user "7261" begins his route into position #1 (t_0) and wants to be directed to his goal position, in the next cell (# 9). During the route the navigator is guided to E (code 3) and, at t_1, steers to SE (code 2), cross footprint #2 (t_3) and arrives to #9. The ceiling lamps (landmarks) spread over all the building and act as edge/fog nodes in the network, providing well-structured paths that maintain a navigator's orientation with respect to both the next landmark along the path and the distance to the eventual destination.

Also, the VLC dynamic system enables cooperative and oppositional geolocation. In some cases, it is in the user's interest to be accurately located, so that they can be offered information relevant to their location and orientation (pin $_1$, pin$_2$ and δ blocks). In other cases, users prefer not to disclose their location for privacy, in this case these last three blocks are set at zero and the user only receives its own location.

C. Multi-person cooperative localization and guidance services

In Figure 6, the MUX synchronized signals received by two users that have requested guidance services, at different times, are displayed. In the top of the figure, the decoded

information is shown and the simulated scenario is inserted to guide the eyes. At the right hand the request/response information is inserted.
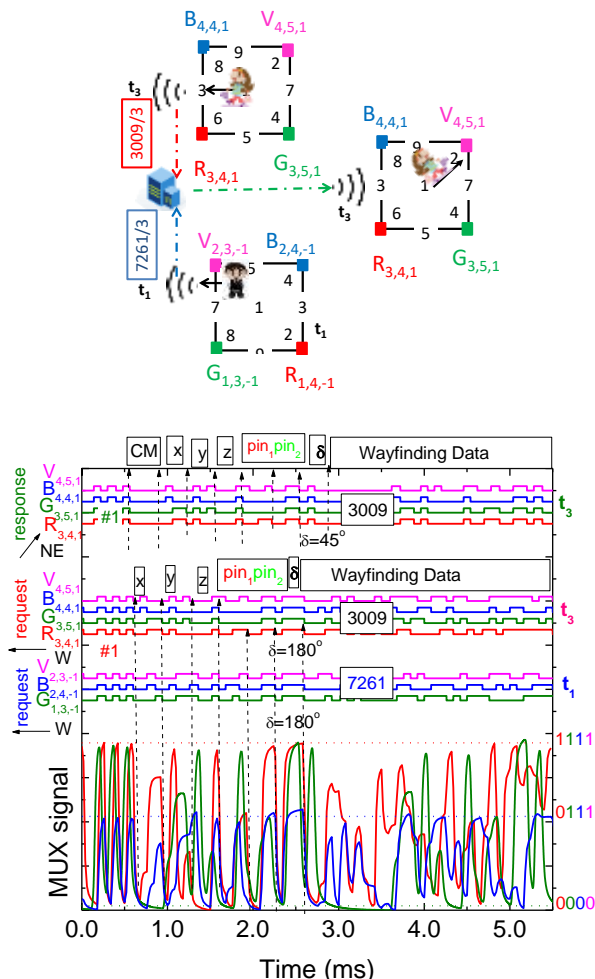

Fig. 6. MUX/DEMUX signals assigned requests from two users ("3009" and "7261") at different poses ($C_{4,4,1}$; #1W and $C_{2,3,-1}$; #6 W) and in successive instants (t_1 and t_3).

We have assumed that a user located at $C_{2,3,-1}$, arrived first (t_1), auto-identified as ($q_i(t_1)$, i="7261",) and informed the controller of his intention to find a friend for a previously scheduled meeting (code 3). A buddy list is then generated and will include all the users who have the same meeting code. User "3009" arrives later ($q_j(t_3)$), sends the alert notification ($C_{4,4,1}$; t_3) to be triggered when his friend is in his floor vicinity, level 1, identifies himself ("3009") and uses the same code (code 3), to track the best way to his meeting . The "request" message includes, beyond synchronism, the identification of the user ("3009"), its address and orientation, $q_i(t)$, ($C_{4,4,1}$, #1W) and the help requested (Wayfinding Data). Since a meet-up between users is expected, its code was inserted before the right track request. Upon receiving this request (t_3), the buddy finder service uses the location information from both devices to determine

the proximity of their owners ($q_{ij}(t_3)$) and provides the best route to the meeting, avoiding crowded areas. In the "response", the block CM identifies the CM [0000] and the next blocks the cell address ($C_{4,4,1}$), the user (3009) for which the message is intended and finally the requested information: meeting code 3, orientation NE (code 4) and wayfinding instructions.

Results show that, with VLC's dynamic LED-aided guidance system, users can get accurate route guidance and perform navigation and geotracking. Users of VLC in large buildings will be able to find the shortest route to their destination, providing directions as they go.

Moreover, the bidirectional communication capabilities of the system open up possibilities for various services. For example, mission-critical services can utilize the reliable and low-latency communication provided by the ID system. Furthermore, consumer-oriented services such as location-based advertisements, personalized information delivery, and indoor wayfinding can be implemented to enhance user experiences within the building.

IV. CONCLUSIONS

We have proposed and characterized a VLC-based guidance system for mobile users inside large buildings. A mesh cellular hybrid structure was chosen as the architecture, and the communication protocol was defined for a multi-level building scenario. An analysis of bidirectional communication between the infrastructure and the mobile receiver was conducted.

According to global results, the location of a mobile receiver is found in conjunction with data transmission. The dynamic LED-aided guidance system provides accurate route guidance, allows navigation, and keeps track of the route. Localization tasks are automatically rescheduled in crowded regions by the cooperative localization system, which provides guidance information and alerts the user to reschedule.

Additionally, the ID system based on visible light can enhance security within the building. The unique identification of spatial beams enables the implementation of access control systems, ensuring that only authorized individuals can access specific areas. Overall, the utilization of visible light as an ID system offers significant potential for a wide range of applications, including positioning, navigation, security, and various consumer services.

ACKNOWLEDGMENT

REFERENCES

[1] Huang, C.-H., Lee, L.-H. ,Ho, C., L., Wu -L. and Lai, Z.-H., "Real-Time RFID Indoor Positioning System Based on Kalman-Filter Drift Removal and Heron-Bilateration Location Estimation," IEEE Transactions on Instrumentation and Measurement, Vol. 64, Issue 3 (2015), pp. 728-739, 4 September 2014, DOI: 10.1109/TIM.2014.2347691.

[2] Lin, X.-Y., Ho, T.-W., Fang, C.-C. , Yen, Z.-S., Yang, B.-J. and Lai, F., "A mobile indoor positioning system based on iBeacon technology," 37th Annual International Conference of the IEEE Engineering in Medicine and Biology Society (EMBC), pp. 4970-4973, 25 August 2015, DOI: 10.1109/EMBC.2015.7319507.

[3] Hassan, N. U., Naeem, A., Pasha, M. A. and Adoon, T. J. "Indoor Positioning Using Visible LED Lights: A Survey," ACM Computing Surveys Vol. 48, pp. 1-32, 2015, DOI: 10.1145/2835376.

[4] Hassan, N. U., Naeem, A., Pasha, M. A., Jadoon, T., and Yuen, C., "Indoor positioning using visible led lights: A survey,"ACM Comput. Surv., vol. 48, pp.1–32, 2015.

[5] Ozgur, E., Dinc, E., Akan, O. B., "Communicate to illuminate: State-of-the-art and research challenges for visible light communications," Physical Communication 17, pp.72–85 (2015).

[6] Park, S. B., et al., "Information broadcasting system based on visible light signboard," presented at Wireless and Optical Communication 2007, Montreal, Canada (2007).

[7] Tsonev, D., Chun, H., Rajbhandari, H., S., McKendry, J., Videv, S., Gu, E., Haji, M., Watson, Kelly, S. A., Faulkner, G., Dawson, M., Haas, H., and O'Brien, D. "A 3-Gb/s single-LED OFDM-based wireless VLC link using a Gallium Nitride μLED," IEEE Photon. Technol. Lett. 26 (7), pp. 637–640 (2014).

[8] O'Brien, D.H., Minh, L., Zeng, L., Faulkner, G., Lee, K., Jung, D., Oh, Y., and Won, E. T., "Indoor visible light communications: challenges and prospects," Proc. SPIE 7091, 709106 (2008).

[9] Vieira, M., Louro, P., Fernandes, M., Vieira, M. A., Fantoni, A. and Costa, J., "Three Transducers Embedded into One Single SiC Photodetector: LSP Direct Image Sensor, Optical Amplifier and Demux Device," Advances in Photodiodes InTech, Chap.19, pp. 403-425 (2011).

[10] Vieira, M. A., Louro, P., Vieira, M., Fantoni, A., and A. Steiger-Garção, "Light-activated amplification in Si-C tandem devices: A capacitive active filter model," IEEE sensor journal, 12, 6, pp. 1755-1762 (2012).

[11] Vieira, M. Vieira, M. A., Louro, P., Vieira, P., Fantoni, A., "Light-emitting diodes aided indoor localization using visible light communication technology," Opt. Eng. 57(8), 087105 (2018).

[12] Vieira, M. A., Vieira, M., Louro, P., Vieira, P., "Bi-directional communication between infrastructures and vehicles through visible light," Proc. SPIE 11207, Fourth International Conference on Applications of Optics and Photonics, 112070C (3 October 2019); doi: 10.1117/12.2526500 (2019).

[13] Vieira, M., Vieira, M.A., Louro, P., Vieira, P. (2022). A Visible Light Communication System to Support Indoor Guidance. In: Camarinha-Matos, L.M., Ribeiro, L., Strous, L. (eds) Internet of Things. IoT through a Multi-disciplinary Perspective. IFIPIoT 2022. IFIP Advances in Information and Communication Technology, vol 665, pp. 235-252. Springer, Cham. https://doi.org/10.1007/978-3-031-18872-5_14.

[14] Vieira, M., Vieira, M. A., Louro, P., Fantoni, A., Vieira, P. "Dynamic VLC navigation system in Crowded Buildings", International Journal On Advances in Software, v 14 n 3&4, pp. 141-150 (2021).

Heat and Current Annealing Effects on Magnetic Properties of Fe-rich Glass-Coated Amorphous Microwires with Different Radius

Álvaro González*, Paula Corte-León, Valentina Zhukova, Alfon-so García-Gómez, Mihail Ipatov, Julian María González, Juan María Blanco, and Arcady Zhukov
Advanced Polymers and Materials: Physics, Chemistry and Technology, Department of Applied Physics.
Universidad del País Vasco.
San Sebastián, Spain.
e-mail: alvaro.gonzalezv@ehu.eus

Álvaro González, Paula Corte-León, Valentina Zhukova, Alfonso García-Gómez, Mihail Ipatov, Julian María González, Juan María Blanco, and Arcady Zhukov
EHU Quantum Center.
Universidad del País Vasco.
Bilbao, Spain.

Arcady Zhukov
IKERBASQUE, Basque Foundation for Science.
Bilbao, Spain.

Abstract—**For Fe-rich glass-coated microwires to be a competitive option for magnetic technologies, the enhancing and tuning of their properties is necessary, and therefore, a better understanding of these processes is also needed. In this work, two Fe microwires with different geometries are subjected to both conventional and current annealings to study their effects. Results show a general enhancement of magnetic softness and domain wall dynamics after both treatments, also suggesting an earlier onset of crystallization in thin samples.**

Keywords- Amorphous alloys; Annealing; Glass-coated microwires; Magnetic characterization.

I. INTRODUCTION

Glass-Coated amorphous microwires are wires with radius sizes of µm, consisting of an amorphous metallic alloy core enveloped by a glass coating. The main interest in this kind of materials comes from their wide range of magnetic properties, such as: bi-stability, ultra-fast magnetic switching, magnetic softness [1] and the general modification of most of these properties under different situations, like the application of high temperatures and/or electrical currents to a microwire sample. As magnetic properties of these microwires are dependent on their chemical composition and geometric parameters, so are the resulting changes on them after annealing, thus the same process parameters may produce different results on different kinds of samples.

While Fe-rich microwires properties are generally considered inferior (mainly lower magnetic sensitivity and magnetic softness) to those possessed by Co microwires, they represent a cheaper, more obtainable alternative [1]. Thus, annealing might prove to be an important asset in producing microwires with properties tuned to their desired use. As such, the main goal of this work is to measure some of the magnetic properties of two different types of glass-coated microwires under the same annealing conditions, to obverse and better understand the resulting changes and the differences between them.

Henceforth, this paper is structured as follows: Section II focuses on the physical techniques used to procure the experimental data to be studied in this paper. As such, Section III consists of a series of subsets, each focusing on the observation and study of data, each related to a relevant property of the microwires and their change with different parameters. After exposing the results, Section IV conducts a briefer explanation and discussion on them, and the conclusions that can be drawn from this work.

II. EXPERIMENTAL

In this section we introduce and describe the experimental procedures applied in the obtention of our studied data, consisting of both the fabrication technique of our microwires and the measurement experiments conducted to study their magnetic properties, as well as their most relevant parameters to their results.

A. Fabrication and Parameters of the Microwires

While some different fabrication processes for amorphous magnetic microwires may be used, we focus on the Taylor-Ulitovsky technique, explained in further detail in [2], as it allows to produce up to 103 m of a single microwire, while simultaneously coating it with Duran type glass. The importance of this glass coating comes from its mechanical interaction with the metallic core. As the alloy lacks crystalline ordering, magnetoelastic anisotropy is one of the main parameters to define its magnetic structure. Therefore, the presence of a glass coating and the stresses that it brings to the core strongly contribute to its magnetic behavior. As such, chemical composition of the core is also relevant, as it defines the magnetostriction constant, λ. By this criteria, two general compositions are usually described and studied: Co-rich with $\lambda<0$, and Fe-rich with $\lambda>0$ [1].

A notable characteristic of microwires, originated from their λ values and the internal stresses originated from the shell-core interactions, are magnetic domain structures: an inner and outer domain arranged in a cylindrical symmetry, with the inner domain presenting axial magnetic anisotropy, pararel to the wire's axis for both Co and Fe based microwires. However, while the former's outer domain has circular magnetic anisotropy, the latter's anisotropy is radial,

TABLE I.   TABLE TYPE STYLES

Sample name	Composition	Inner diameter d (µm)	Total Diameter D (µm)	d/D
"Thick"	$Fe_{71.8}B_{13.27}Si_{11.02}Nb_{2.99}Ni_{0.92}$	47.9	53.2	0.9
"Thin"	$Fe_{74.87}B_{9.06}Si_{11.99}C_{4.08}$	15.2	17.2	0.88

Composition and geometries of studied microwires. The inner diameter, d, corresponds to only the metallic core, while the total diameter, D, includes both core and glass coating.

usually with a proportionally thinner inner domain [1]. These differences in magnetic domains are related to magnetic properties of microwires: while Co-based microwires typically attract more attention, as they show higher magnetic softness, Giant Magneto-Impedance (GMI) effect and sensitivity to stimuli (like stress or magnetic fields), Fe is a more common, cheaper material, allowing for the production of bigger quantities of microwire for less costs, making it an attractive alternative for the long run [1].

On the other hand, treatment of microwires has shown observable changes of their magnetic properties, depending on both treatment conditions and microwire parameters [3]. Therefore, a correct combination of these two elements may be used to tune properties into the most advantageous for desired applications. With all of this in mind, two Fe-rich glass coated microwires have been fabricated and characterized, as shown in Table I. From these microwires, several 24 cm samples were then cut off, as to allow their proper handling for annealing and experimentation.

B.   Magnetic Characterization and Annealing

For this work, we focus on the measurement of the hysteresis loop, Domain Wall (DW) velocity and GMI efficiency of microwire samples before and after specific annealing treatments. Measurements of hysteresis loops are carried out via a simple fluxmetric method at 114Hz, with a 13cm long inductive coil, and 2 cm pickup and compensator coils. DW dynamics is studied with a modified Sixtus-Tonks method [4], using three pickup coils to detect the change in magnetic flux produced by the change in the sample magnetization as domain walls move through them.

Determination of the GMI efficiency is carried out by using a network vector analyser, as described in [5], which allows measuring the impedance Z of a ~5mm sample under the action of both an alternate current at fixed frequencies and homogeneous magnetic fields. Thus, for each AC frequency we can evaluate the GMI ratio as a function of the applied magnetic field, H [6]:

$$\Delta Z/Z = [Z(H) - Z(H_{max})]/Z(H_{max}) \qquad (1)$$

Hmax being the max value of the applied magnetic field in the used experimental setup. Measurements were carried out on samples subjected to at least one of two different types of annealing: conventional annealing, by simply introducing them into a furnace at temperatures of 300, 400 and 500 ℃, for 1 and 3 hours; and current annealing, by making a direct current pass through them. Current intensities and annealing times presented in this work were

chosen as it had been previously observed that they produce the most noticeable changes in these microwires [7].

III.   RESULTS

Having produced our microwire samples and experimented on their magnetic behavior, we now proceed to study the obtained data on their magnetic hysteresis, domain wall dynamics and giant magneto-impedance effect, comparing the results depending on measurement and annealing conditions, as to ascertain the effect of said conditions and their possible combination to tune the microwire's properties for desired applications.

A.   Magnetic Hysteresis

Some examples of the measured loops are presented in Figure 1. As usual for Fe based microwires with positive λ (~10-6), their shapes are fairly rectangular, with a single Barkhausen jump and magnetic bi-stability [8]. It can be seen that, the thicker the sample, the bigger its coercive field, HC. It is also worth noting that the effect of current annealing seems to be greater on both samples, as it brings HC to lower values.

To better compare the effects of annealing, Figure 2 shows the measured HC obtained for all realized treatments, except for the "Thin" wire annealed with 500ºC. It is obvious that for "Thick" samples, the higher the annealing temperature, the bigger its reduction of HC as a result of the relaxation of their inner stresses. Opposite to this, "Thin" samples show a raise after long enough annealing times, as their higher surface to volume ratio allow for higher thermal energy densities, and thus, for an earlier onset of the alloy's crystallization. On the other hand, current annealing of all samples shows a consistent reduction of HC, even for long annealing times.

The reason for excluding "Thin" samples annealed with 500ºC is that they exhibited rather different results, as can be seen in Figure 3. Annealing at high temperatures of "Thin" samples resulted on an observable magnetic hardening, most likely as a result of crystallization of the metallic core [1].
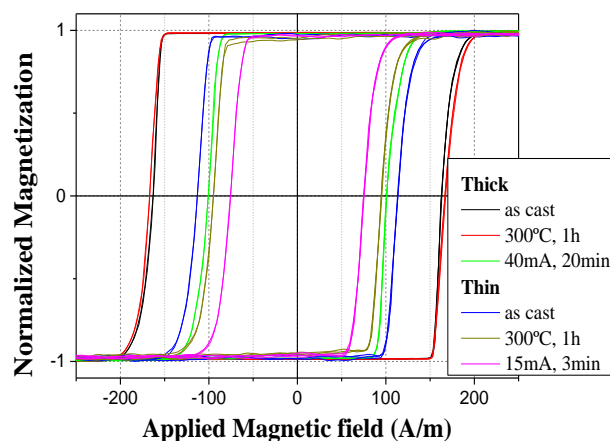

Figure 1.   Hysteresis loops of samples before and after different treatments.
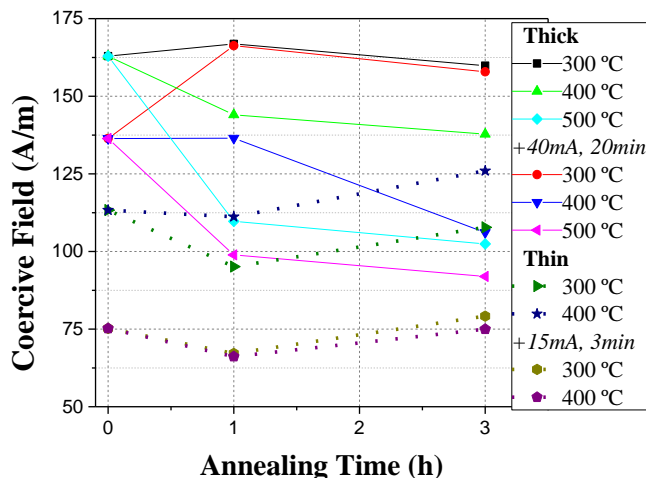
Figure 2. H_C dependece on annealing times. The "+" indicates the application of current annealing <u>after</u> conventional annealing.

Additionally, as the inset in Figure 3 shows, a small metastable transition between two Barkhausen jumps is taking place at around 0 magnetization, which could be hinting at the presence of two distinct crystalline phases in the metallic core upon its devitrification, with the magnetization of one phase beginning shortly after the other one is completely done. Furthermore, current annealing of these samples may be resulting in a change in the proportion of said crystalline phases, as the position of this metastable step is modified upon the application of current.

B. Domain Wall Dynamics

After measuring DW velocities of all samples under applied field, a consistent pattern, briefly represented in Figure 4, was observed. Firstly, "Thin" microwires possess higher DW mobility (slope of the field dependence of DW velocity [4]), than "Thick" ones, reaching higher DW velocities for the same applied field. Conventional annealing of both types of samples yields a boost on DW mobility, especially on the
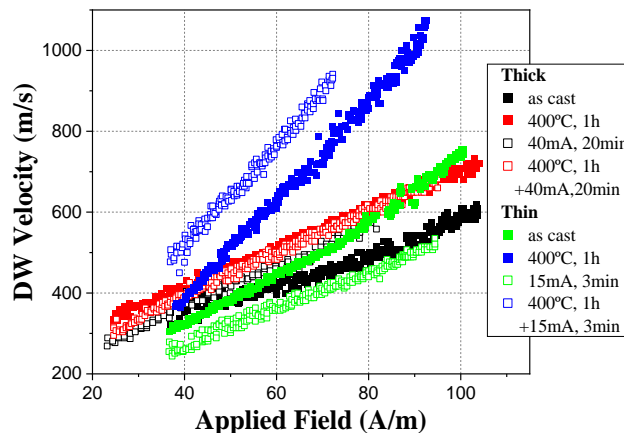

Figure 4.   DW velocities of samples after annealing.

DW velocities of "Thin" samples annealed at 500º could not be measured, most probably due to their magnetic hardening, as shown in Figure 3, which would make them require a higher magnetic field than those produced by our system for their DW to star propagating. Secondly, current annealing results on different effects depending on the sample and previous annealing: while current alone produces a slight increase of DW mobility of "Thick" microwires, "Thin" ones experience an observable reduction. However, current annealing after conventional annealing seems to have opposite effects, as "Thick" samples seem unaffected while the boost on mobility of "Thin" ones grows even bigger.

C. Giant Magneto-Impedance

The GMI ratio of all samples was measured for frequencies up to 1 GHz. A short, representative example is shown in Figure 5. This figure carries some interesting information points about the magnetic domain structure of our microwires, as well as about their behavior under the action of annealing and their contribution to the GMI effect efficiency. First, both type of microwires exhibit a double
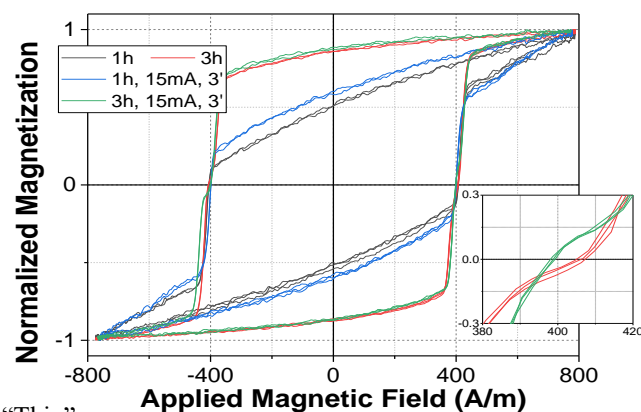
"Thin" ones.

Figure 3.   Hysteresis loops of "Thin" microwires annealed with 500˚C for different times and with posterior current annealing.
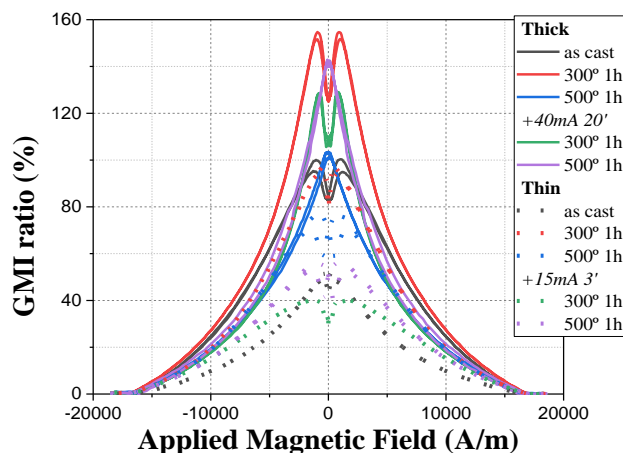

Figure 5.   GMI ratios of microwire samples at 200 MHz.

peak structure in their GMI graphs, a phenomenon usually related to the magnetic domain structure of Co-rich microwires. This is congruent with previous results obtained by our own research [7]. However, when "Thick" samples are annealed at high enough temperatures, this double peak is lost at lower frequencies, appearing as the single peak expected in Fe-rich microwires. The most probable cause for this is the relaxation of internal stresses in the microwire, causing a reduction in size of the outer domain and, therefore, its contribution to the GMI effect.

Secondly, while as-cast "Thick" samples show a GMI max ratio (100%) quite higher than that of "Thin" ones (50%), and annealing of both microwires results in an enhancement of their ratios, the growth of "Thin" GMI (from 50% to 100%) is proportionally bigger than that observed in "Thick" ones (from 100% to less than 160%).

To better understand how annealing affects each microwire, Figure 6 and Figure 7 represent the max values of GMI ratios of annealed "Thick" and "Thins" samples respectively. When comparing both graphs, it becomes obvious that thicker microwires yield a higher GMI performance, as the highest ratios produced by annealed "Thin" samples does not surpass those of the "Thick" as cast sample. While it can be seen that annealing has indeed provided an enhancement on GMI ratios of both microwires, a closer look on both graphs reveals behaviors that are more complex. In Figure 6, conventional annealing at 300ºC results in the highest GMI values of the sample at both 1 and 3 hours, while annealing at 500ºC lowers said values back to a level similar to that of the as cast state. The addition of current annealing after these processes yields a negative effect in most cases, as the GMI ratios values become lower, with the exception of the annealing with 500ºC for 1 hour, which results in an enhancement comparable to those obtained at 300ºC.
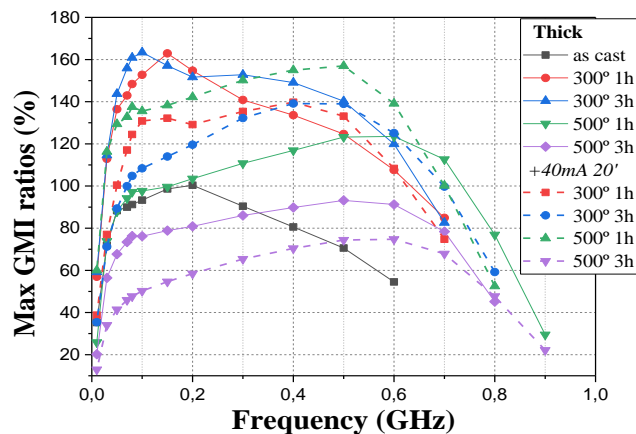

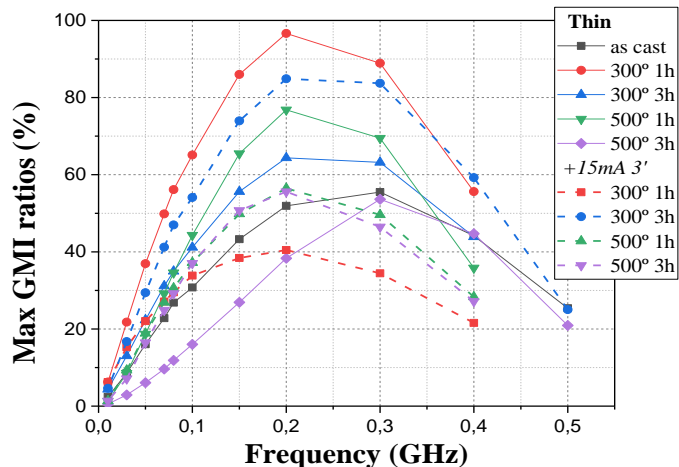Figure 6. Max values of GMI ratios of annealed "Thick" samples.

Figure 7. Max values of GMI ratios of annealed "Thin" samples.

IV. CONCLUSIONS

While thinner microwires possess better magnetic softness due to lower HC values, they also show a lower resistance to heat as, under the same annealing conditions, there are hints of alloy crystallization, not present on thicker ones. Current annealing may prove to be a decent alternative to heat annealing as, with only some minutes of treatment, the reduction of HC is bigger than annealing under 400ºC for 3h (Figure 2). Combination of both annealings has yielded a further reduction of these values, especially in thicker microwires. Opposite to these trends, DW dynamics show that annealing barely affects thick microwires, while thin ones can be subjected to either a boost or reduction of their DW velocities.

Conventional annealing of both types of microwires at 300ºC for 1 hour has shown to yield the highest values of GMI ratios, while de addition of current annealing after this process is mostly detrimental, except for specific cases in which said values are once again enhanced after their lowering due to excessive annealing temperatures or times. This might prove to be an interesting option to "repair" the sensitivity of microwires used in magnetic sensing technologies at high temperatures.

REFERENCES

[1] A. Zhukov, M. Ipatov, and V. Zhukova, "Advances in giant magnetoimpedance of materials", in: K.H.J. Buschow (Ed.), Handbook of Magnetic Materials, vol. 24, pp. 139 - 236 (chapter 2), 2015.

[2] A.V. Ulitovsky, I.M. Maianski, and A. I. Avramenco, "Method of continuous casting of glass coated microwire", Patent No128427 (USSR), 15.05.60, Bulletin, 10, p. 14.

[3] V. Zhukova et al., "Optimization of soft magnetic properties in nanocrystalline Fe-rich glass-coated microwires", JOM, 67, pp 2107 - 2113, 2015.

[4] V. Zhukova et al., "Domain wall propagation in micrometric wires: limits of single domain wall regime", J. Appl. Phys. 111, pp 07E311-1 - 07E311-3, 2012.

[5] M. Ipatov, V. Zhukova and A. Zhukov. "Low-field hysteresis in the magnetoimpedance of amorphous microwires". Phys. Rev. B 81, pp 134421-1 - 134421-8, 2010.

[6] P. Corte-Leon, V. Zhukova and A. Chizhik. "Magnetic Microwires with Unique Combination of Magnetic Properties Suitable for Various Magnetic Sensor Applications". Sensors 20, pp 7203-1 – 7203-21. 2020

[7] A. Gonzalez et al., "Effect of Joule heating on GMI and magnetic properties of Fe-rich glass-coated microwires", AIP Adv. 12, pp 035021-1 - 035021-4, 2022.

[8] M. Churyukanova et al., "Magnetostriction investigation of soft magnetic microwires", Phys. Status Solidi A 213(2), pp. 363 - 367, 2016.

Multi Human Posture Classification Using MIMO FMCW Radar Point Cloud and Deep Learning

Sohaib Abdullah, Shahzad Ahmed, Junbyung Park, Chanwoo Choi, Sung Ho Cho[*]

Department of Electronic Engineering, Hanyang University

Seoul, South Korea

E-mail: {engrsohaib79, shahzad1, jbp0917, choi231121, dragon}@hanyang.ac.kr

*Correspondence: Sung Ho Cho, dragon@hanyang.ac.kr

Abstract—Human action and pose recognition in context of health and safety has lately attracted a huge amount of attraction. Human pose recognition using radar is a challenging task since the human under consideration is static. This paper uses Multi Input Multi Output (MIMO) Frequency Modulated Continuous Wave (FMCW) radar to recognize postures of two co-located humans using Convolutional Neural Network (CNN). Two humans at different angles and arbitrary distance (in living room) are simultaneously considered for data collection. Radar-extracted spherical coordinates of posture are acquired using Fast Fourier transform (FFT) and afterwards, spatial transformation is used to convert these points into Cartesian coordinate system. The resultant image shows the posture of two persons in a single image. A clustering approach is used to classify the two postures and CNN is trained to classify each posture. Promising accuracy is achieved for one and two persons posture recognition.

Keywords—*Human Posture Recognition; FMCW Radar; Deep Learning; non-contact healthcare; CNN.*

I. Introduction

The increasing life expectancy [1] and declining birth rate [2] in developed nations have raised concerns regarding the healthcare provision for aging population. Statistics suggest that elderly persons tend to either live alone or with their spouse. For example, the percentage of elderly people living alone was 36% in 2016 [3].

Continuous posture recognition in the home environment can be used to monitor human behavior for remote healthcare applications. Any abnormality in the behavior can be recognized remotely by recognizing the postures or the dynamic movements (activities).

Sensory technology to detect and a sign of danger or medical emergency based on activity and posture recognition can be a useful tool in scenarios where people (or a couple) tend to live alone. Need of having persuasive healthcare for elderly persons is increasing lately. Consequently, wireless (non-contact) human posture and activity recognition is emerging as a prominent research domain since it can provide a framework for an early detection of medical emergency. In particular, we exert our focus on multi-human posture recognition in this paper.

For posture recognition, one of the best candidate solutions could be a camera sensor however, installing camera in home environment raises several privacy related issues. A possible privacy-preserving solution for posture and activity recognition is a radio sensor such as radar. Nowadays, off the shelf (OTS) low cost and compact size radar sensors are abundantly available and have shown their usefulness in several research domains, such as gesture recognition [4] [5], vital sign monitoring [6] [7] and people counting [8].

For human posture recognition based on radar, several research works have been published in recent year [9]. Nowadays, researchers are showing interest in recognizing activities from the radar-extracted point cloud [10] [11] [12]. Activities recognized from the radar point cloud have a huge potential in recognizing the dynamic movements as well as static postures. Lee et al. [11] recognized several postures using radar extracted point clouds. However, two deep learning models were used in that study, first to extract the point cloud followed by posture and activity classification which is a computationally expensive deep learning framework. Another study presented by Singh et al. [12] extracted five exercising activities using radar point cloud followed by deep learning model. Similarly, sleep posture recognition is also a topic of consideration amongst research community [13].

In this study, we are aiming for a deep learning framework which can learn features from raw point cloud images to classify multi-human postures. The postures considered in this study are sitting, standing, lying down, and picking up something from ground. Since we are recognizing the posture of the two co-located humans, ten different scenarios (or combinations) can be visualized based on the four basic postures as shown in Figure 1. We used Multi Input Multi Output (MIMO) Frequency Modulated Continuous Wave (FMCW) radar for data capturing purposes. The cascade radar consists of 86 x 4 receivers (RX) and transmitters (TX). Although high dimensional MIMO configuration is used however, such sensor are now abundantly available in the market.

The Proposed framework is capable of recognizing the postures of two persons located at different angles and arbitrary distance within a small room. If an elderly person is standing or sitting or lying on ground, one can get a detailed insight about what the person is trying to do. For instance, if the person is lying on ground, it can be a sign of fall.

To our knowledge, multi-human posture classification using FMCW radar-extracted point cloud has not been discussed widely so far. The rest of our paper is organized as follows: Section 2 presents the methodology and Section 3 discusses the experimental setup. Afterwards, Section 4 and 5 discuss the results and conclusion respectively.
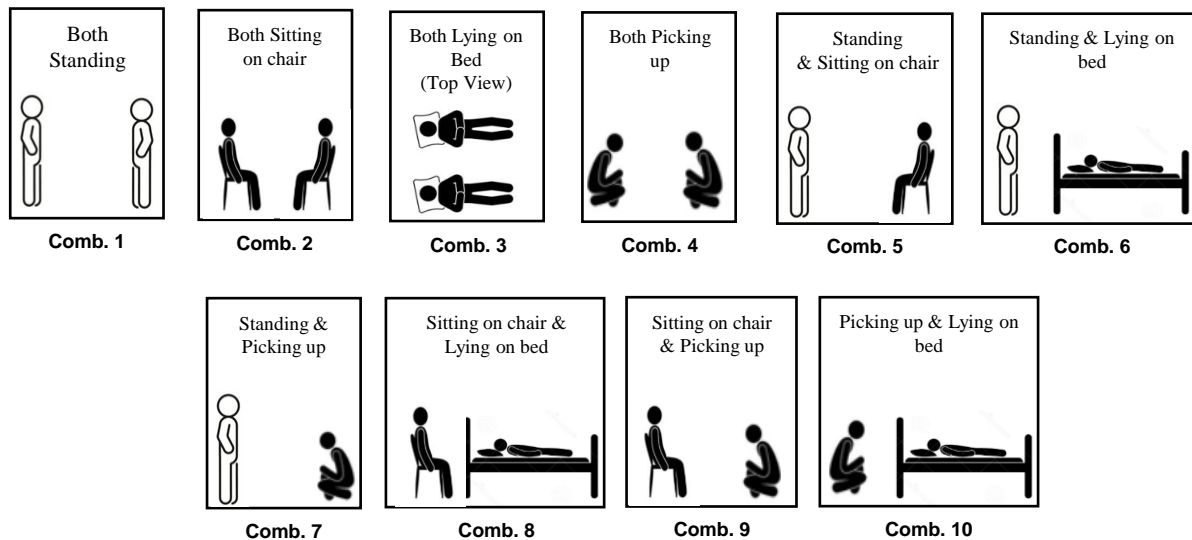
Figure 1. Ten possible combinations of postures (standing, sitting on chair, picking up something and lying down on bed) for two persons.

II. METHODOLOGY

Figure 2 shows the overall methodology of our point cloud based activity recognition framework. First the data is collected from two human participants closely located humans using FMCW radar. Afterwards, point cloud is generated using range, doppler and angle information, which will provide us the spherical coordinates of the radar returns. These spherical radar returns are further converted into three dimensional (3D) Cartesian coordinate system. Afterwards, a Deep Convolutional Neural Network (DCNN) model is trained and evaluated. Note that in our study, the extracted 3D point cloud in its raw form shows the shape of actual posture up to some extent. Next, following passages discuss each step in further detail.
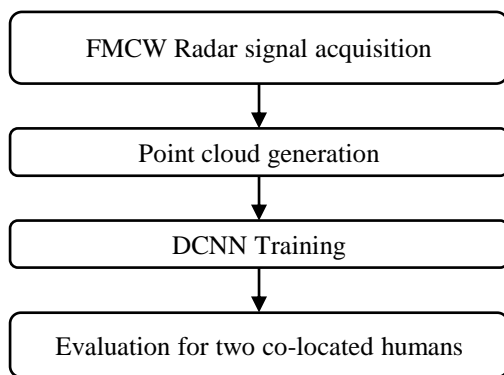

Figure 2. High level block diagram of posture recognition framework.

A. FMCW Radar Data Pre-processing

In FMCW radar, the frequency of the transmitted signal increases linearly with time and the increasing ramp is known as chirp. Several chirps are transmitted simultaneously in a single frame. This allows the FMCW radar to extract the distance and velocity in simultaneous fashion. In addition to that, the diversity created by MIMO settings is used to extract the angle of the target as well. The transmitted signal $x(t)$ can be expressed as:

$$x(t) = exp(j2\pi(f_c t + \frac{B}{T}t^2)) \tag{1}$$

where the term B represents the bandwidth of signal, f_c denotes the operating frequency and T is pulse duration. After colliding with the body of human in sitting, standing, picking up something, or lying down settings, the received signal will be:

$$x(t) = exp(j2\pi(f_c(t - \tau) + \frac{B}{T}(t - \tau)^2)) \tag{2}$$

where τ represents the delay between transmitted and received signal. After multiplying the transmitted signal with the copy of received signal, the low frequency signal which carries the information about the target is termed as the Intermediate Frequency (IR) signal and expressed as:

$$x_{IF}(t) = exp(j2\pi(f_c\tau + \frac{B}{2T}\tau^2)) \tag{3}$$

This low frequency signal is sent to the computer and further exploited to extract target information. The FFT of this signal will give us the distance information of the targets present within the operational range of radar. The same process is repeated for all the RX channels to extract the target information at each receiver. Note that we require multiple channels to find the azimuth and elevation angles of the target.

B. Target Detection using CFAR

The acquired signal at each RX channel is passed through a Constant False Alarm Rate (CFAR) detection algorithm to detect the target and neglect the noise. A 2D-CFAR is applied
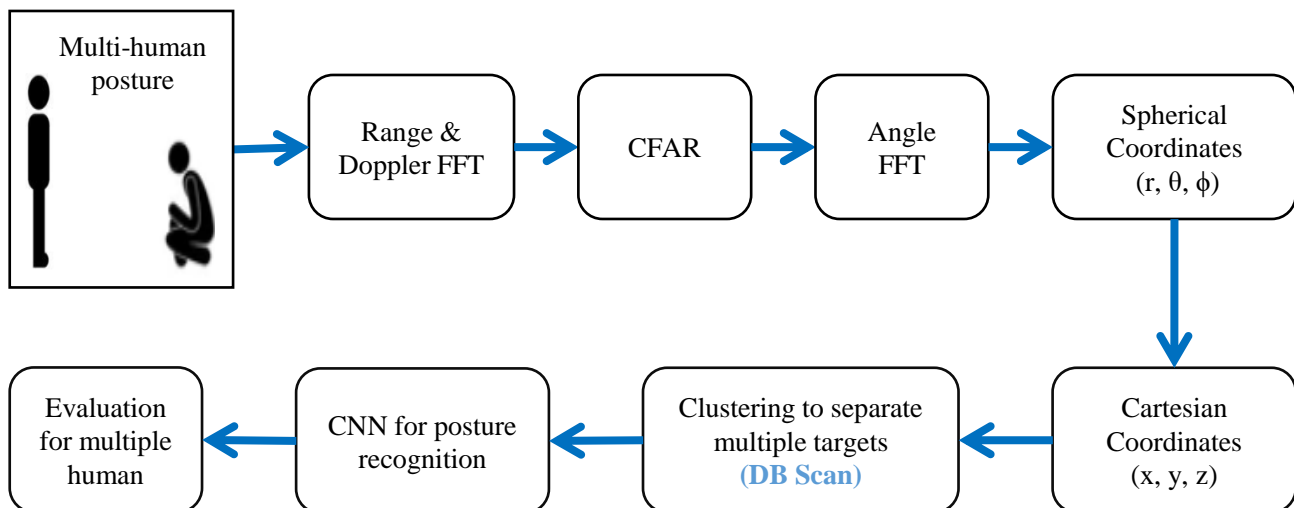
Figure 3. End-to-End framework from data capturing to classification.

on radar signals, first in the range dimension followed by doppler dimension. Specifically, Cell-Averaging Order Statistics (CASO-CFAR) is used as it leverages the benefits of both CA-CFAR and OS-CFAR, thus making robust target detection in low as well as high cluttered environments.

C. Data to Point Cloud Conversion

Once targets are detected, a MIMO FMCW radar allows the extraction of distance (r), azimuth angle (θ), and the elevation angle (ϕ) of the targets. These spherical values of each back-scattered reflection shows where the target is located in the spherical coordinate system. These values are further converted into the Cartesian coordinate system by using below set of identities:

$$x = r\sin(\theta)cos(\phi) \tag{4}$$

$$y = r\cos(\theta)cos(\phi) \tag{5}$$

$$z = rsin(\phi) \tag{6}$$

where the pairs x, y, z represents the Cartesian points of the target corresponding to the spherical points r, θ, ϕ.

D. Recognition Framework

1) Radar Data to Image Conversion

The overall end-to-end recognition framework is shown in Figure 3. As discussed earlier, taking the FFT of each received frame shown in (3), provides the distance of back-scattered signal. Taking another FFT across each chirp within a frame provides the velocity FFT. Prior to the extraction of angle, CFAR detection is applied to find human targets. Afterwards, taking FFT of range-Doppler across each receiving channel will provide the angles of the target denoted as r, θ, ϕ.

After extracting the Cartesian coordinate points of the target, the point where human is located appears as a cluster of co-located points. These patterns are saved as a 2-D images for Deep learning model training purposes.

2) Model Training

In this work, the model is first trained to recognize each individual posture. A four-class classifier using DCNN model named as shuffle-net [14] is used for that purpose. Image containing a single human posture is first labeled, since the supervised learning approach requires dataset labeling [15]. In comparison to the other deep variants of CNN such as AlexNet and GoogleNet [4], Shuffle-net is extremely efficient in terms of computation [14].

Several density-based region selection methods exist for recognition of multiple objects in an image such as region based rCNN and fast rCNN [16]. We opted a simple clustering approach to detect multiple objects in an image. DBSCAN algorithm is opted to find multiple (two) clusters in an image. DBSCAN joins the point based on regional density, rather than the distances. It has an extensive usage in radar-based target localization applications [17]. In this way, multiple images are generated from a single image containing posture of two persons, and multiple deep learning classifiers are used to find the two postures within one image.

III. EXPERIMENTAL SETUP

The experimental setup and equipment to capture radar point cloud is shown in Figure 4. Two participants were in front of radar with a slightly distinct angle. Two commercial radars named AWR2243 CASCADE and IWR6843ISK-ODS were used to show the posture quality of a high and low virtual antenna array. Both radars are manufactured by Texas Instrument (TI), United States. CASCADE radar offers 86 x 4 horizontal and vertical arrays for azimuth and elevation calculation whereas ODS radar consists of 4 x 4 azimuth
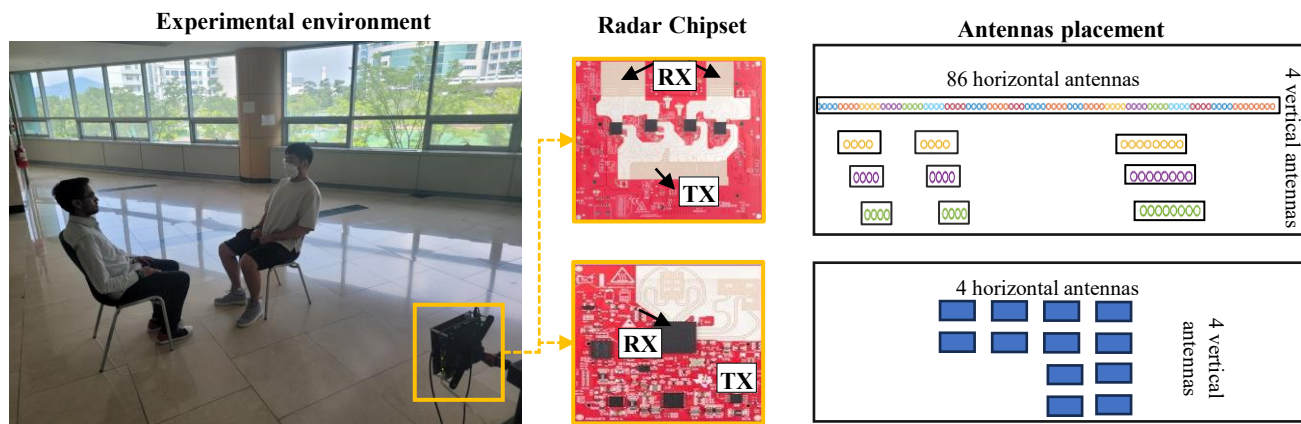
Experimental environment **Radar Chipset** **Antennas placement**

Figure 4. Experimental setup and equipment. Left: Experimental environment; middle: OTS FMCW radars; right: Antennas placement configuration.
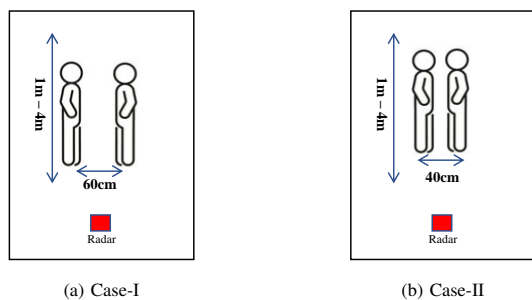

(a) Case-I (b) Case-II

Figure 5. Experimental setup showcasing target range and separation.

and elevation antennas. For CASCADE radar, two cases were taken into study as shown in Figure 5. In Case-I, the range of targets from radar was within one to four meters, while keeping a fixed 60cm separation between both participants at all times. In Case-II, the separation between participants was further reduced to 40cm. For ODS radar, separation of participants was set to 60cm at 2.5m range. A Total of 600 samples were collected for all the ten combinations shown in Figure 1 and data from two different participants was collected.

The rest of the hardware parameters of both radars are shown in Tables I.

TABLE I. Radar Sensor Parameters.

Parameter	CASCADE Radar	ODS Radar
Start Frequency	77 GHz	60 GHz
Bandwidth	3.3 GHz	4 GHz
Number of Chirps	32	32
Number of ADC samples	256	256
Frame Rate	20 FPS	20 FPS
Number of Frames	20	20
Number of TX antennas	12	3
Number of RX antennas	16	4
Antenna Array (TX x RX)	86 x 4	4 x 4
Range Resolution	4.5 cm	3.76 cm
Azimuth Angle Resolution	1.4^o	29°
Elevation Angle Resolution	18°	29°

IV. RESULTS

This Section discusses the results obtained using CAS-CADE and ODS FMCW radars and compare their efficacies for co-located multi-person posture recognition.

A. Point Cloud Visualization with Cascade Radar

1) Case-I: 60cm Separation between Targets and Arbitrary Range

Figure 6 shows the clustered point-cloud of all the ten combinations of postures using high resolution cascade radar. The first four images are the cases when both the participants are having same posture, that is to say, both participants are standing, sitting, picking up something from ground, or lying down. Afterwards, the individual postures are combined in such a way that there is no repetition of posture in the patterns. As shown in Figure 6, the cascade radar is capable of extracting the exact postures of two participants with high precision.

2) Case-II: 40cm Separation between Targets and Arbitrary Range

The cascade radar can clearly differentiate two closely located humans, due to very high azimuth angle resolution (see Tables I). Figure 7 shows some combinations of postures in which both participants are in very close proximity. In this case, feet of both participants were in touch with each other. For both sitting scenario, point cloud for left participant has some empty area because of very small separation between them. These two figures suggest that a high resolution antenna diversity radar is required for multiple person human posture recognition problem. Figure 6 and Figure 7 suggest that if the two participants are slightly distinct in terms of horizontal angle, the both the postures can be visualized using the framework presented in this paper. In the end, samples from both cases were merged for final classification.

B. Point Cloud Visualization with ODS Radar

The point cloud extracted using the radar consisting of fewer TX and RX antennas was not as accurate as the one shown in Figure 6. Hence, only the point cloud images extracted
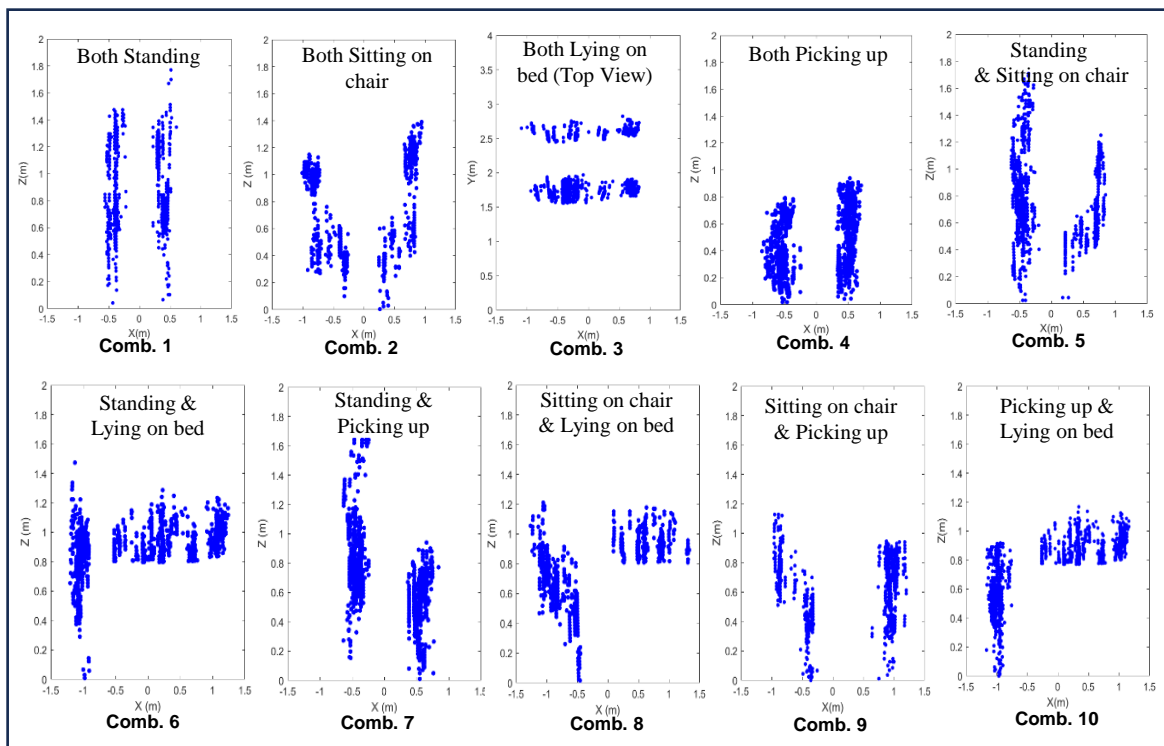
Figure 6. Point cloud for all the ten combinations of postures using cascade FMCW radar (for Case-I).
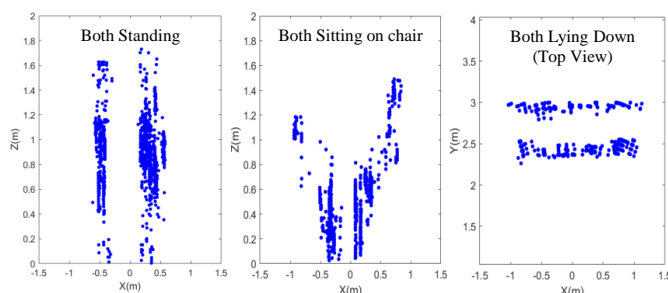

Figure 7. Point cloud of two persons extracted using cascade FMCW radar (for Case-II).
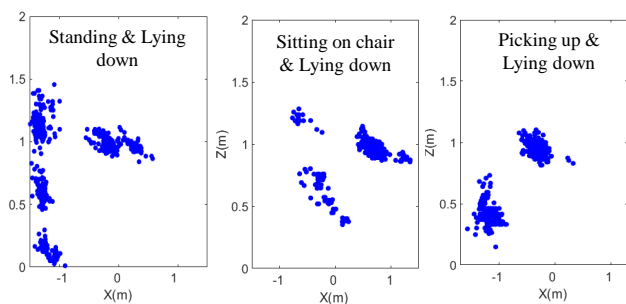

Figure 8. Point cloud of two persons, extracted using a low (angle) resolution (ODS) FMCW radar.

using CASCADE FMCW radar are used in this study. A few scenarios of two persons point cloud extracted using a 4x4 low (angle) resolution FMCW radar are shown in Figure 8. In order to be properly detected as two distinct targets, the separation between two targets was set to 60cm but the point cloud generated using 4x4 radar is not clear in comparison to the point cloud generated using cascade radar.

C. Classification Accuracy

Although we performed classification using both the radars, the confusion matrix of Cascade radar is included in the paper since the accuracy of ODS radar was very low. Consequently, we can conclude that a radar with high angle resolution can be used to extract point cloud based posture of multiple human subjects consecutively.

The results of the DBSCAN based image cropping are shown in Figure 9. The image on the left side shows separate clusters being formed for standing and sitting postures. In addition to that, noise is also shown as a third cluster. For the captured dataset, DBSCAN clustering approach was able to divide the input point cloud image having two postures into two separate images.

The confusion matrix presented in Figure 10 shows the classification accuracy of all the ten scenarios using Cascade radar, consisting of 86 RX horizontal and 4 vertical antennas (see Figure 4). It can be seen that, 2nd, 5th and 8th combination showed highest classification error followed by 3rd, 6th and 9th combination as expressed in the confusion matrix shown in Figure 10. Although DBSCAN allows robust

target segregation while rejecting noise, some information of the human body can also be lost, if not properly detected by the radar. This is why, sitting on chair and lying down was confused with picking up in some cases when head and feet were not properly detected by the radar. Nevertheless, the algorithm was able to classify the two persons scenario with an overall success rate of 95%.
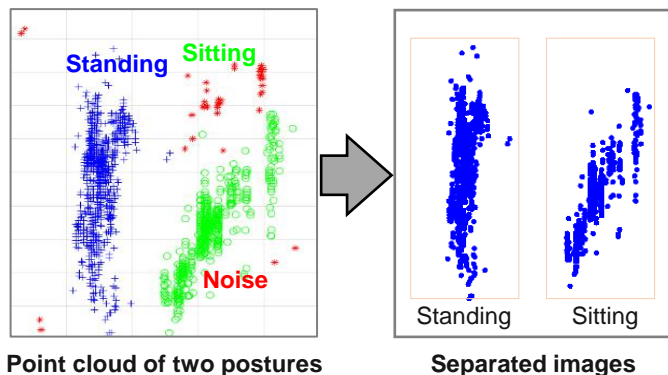

Figure 9. DBSCAN based posture segregation approach.

Figure 10. Confusion matrix for Cascade radar.

V. CONCLUSION AND FUTURE WORK

This paper presents a framework to recognize the posture of two humans located at different angles. A point cloud map showing both the person is first constructed using FMCW radar, and DBSCAN clustering is used to segregate the postures of the two humans. Afterwards, deep learning is used to find the postures of each human. A considerable amount of accuracy is observed while using a high- resolution antenna array.

This framework enables non-intrusive surveillance of elderly couples by providing an assessment of their current position, like lying down. This allows medical professionals and caregivers to intervene promptly in case of emergencies. In addition to static poses, the framework can be extended to detect subtle changes in movement patterns providing more insight into potential risks, like fall detection and prevention.

REFERENCES

[1] L. F. Berkman and B. C. Truesdale, "Working longer and population aging in the us: Why delayed retirement isn'ta practical solution for many," *The Journal of the Economics of Ageing*, vol. 24, p. 100438, 2023.

[2] O. Okpareke, A. Lakhanpal, and S. Chattopadhyay, "The decline in us birthrates in recent years is indicative of cultural and economic changes," 2022.

[3] T.-H. Tan *et al.*, "Binary sensors-based privacy-preserved activity recognition of elderly living alone using an rnn," *Sensors*, vol. 21, no. 16, p. 5371, 2021.

[4] S. Ahmed and S. H. Cho, "Hand gesture recognition using an ir-uwb radar with an inception module-based classifier," *Sensors*, vol. 20, no. 2, p. 564, 2020.

[5] S. Ahmed, K. D. Kallu, S. Ahmed, and S. H. Cho, "Hand gestures recognition using radar sensors for human-computer-interaction: A review," *Remote Sensing*, vol. 13, no. 3, p. 527, 2021.

[6] M. Kebe *et al.*, "Human vital signs detection methods and potential using radars: A review," *Sensors*, vol. 20, no. 5, p. 1454, 2020.

[7] S. Ahmed, J. Park, and S. H. Cho, "Effects of receiver beamforming for vital sign measurements using fmcw radar at various distances and angles," *Sensors*, vol. 22, no. 18, p. 6877, 2022.

[8] C. Y. Aydogdu, S. Hazra, A. Santra, and R. Weigel, "Multi-modal cross learning for improved people counting using short-range fmcw radar," in *2020 IEEE International Radar Conference (RADAR)*. IEEE, 2020, pp. 250–255.

[9] S. Ahmed, J. Park, and S. H. Cho, "Fmcw radar sensor based human activity recognition using deep learning," in *2022 International Conference on Electronics, Information, and Communication (ICEIC)*. IEEE, 2022, pp. 1–5.

[10] Y. Huang *et al.*, "Activity recognition based on millimeter-wave radar by fusing point cloud and range–doppler information," *Signals*, vol. 3, no. 2, pp. 266–283, 2022.

[11] G. Lee and J. Kim, "Improving human activity recognition for sparse radar point clouds: A graph neural network model with pre-trained 3d human-joint coordinates," *Applied Sciences*, vol. 12, no. 4, p. 2168, 2022.

[12] A. D. Singh, S. S. Sandha, L. Garcia, and M. Srivastava, "Radhar: Human activity recognition from point clouds generated through a millimeter-wave radar," in *Proceedings of the 3rd ACM Workshop on Millimeter-wave Networks and Sensing Systems*. Association for Computing Machinery, 2019, pp. 51–56.

[13] J. E. Kiriazi, S. M. Islam, O. Borić-Lubecke, and V. M. Lubecke, "Sleep posture recognition with a dual-frequency cardiopulmonary doppler radar," *IEEE Access*, vol. 9, pp. 36 181–36 194, 2021.

[14] X. Zhang, X. Zhou, M. Lin, and J. Sun, "Shufflenet: An extremely efficient convolutional neural network for mobile devices," in *Proceedings of the IEEE conference on computer vision and pattern recognition*. IEEE, 2018, pp. 6848–6856.

[15] S. Asghar, J. Choi, D. Yoon, and J. Byun, "Spatial pseudo-labeling for semi-supervised facies classification," *Journal of Petroleum Science and Engineering*, vol. 195, p. 107834, 2020.

[16] R. Girshick, "Fast r-cnn," in *Proceedings of the IEEE international conference on computer vision*. IEEE, 2015, pp. 1440–1448.

[17] L. Y. Chan, D. Genschow, and U. T. Schwarz, "Combining delta-phi velocity measurement and dbscan clustering to localize slowly moving objects in short ranges with limited slow-time radar data," in *2023 24th International Radar Symposium (IRS)*. IEEE, 2023, pp. 1–11.

Development of An Autonomous Time-synchronized Sensing System Capable of Measuring Acceleration and Images

Narito Kurata

Faculty of Industrial Technology
Tsukuba University of Technology
Tsukuba City, Ibaraki, Japan
e-mail: kurata@home.email.ne.jp

Abstract - **In Japan, the maintenance and management of aging bridges, highways, and other civil infrastructure and buildings is an important social issue. Proper maintenance and management require regular and highly accurate inspections, but these inspections rely on visual examinations by humans, which are expensive. Hence, to make this process more efficient, there is a need to automate inspections using sensing systems. Moreover, after a disaster, such as a major earthquake or a tsunami, it is necessary to expedite evacuation operations and rescue people, and for this purpose, the viability of or damage to each structure must be accurately evaluated using a sensing system. To meet these challenges, research and development is being carried out on an autonomous time-synchronized sensing system. The system adds high-precision time information to measurement data, acquires and analyzes digital sensor data that are time-synchronized, and uses it to automate inspections. As a first step in this research, a sensor device was developed that performs autonomous time-synchronized sensing using a digital high-precision accelerometer. As a second step, a heterogeneous digital sensing platform was developed that can be connected to a camera sensor in addition to a digital accelerometer. The data from the digital accelerometer and images from the camera sensor are given a unified time stamp synchronized with the absolute time at the moment of data acquisition, thereby enabling synchronized measurement of vibration and images. A mechanism was implemented to add time stamps to the outputs of the digital accelerometer and camera sensor using the timekeeping accuracy of a chip-scale atomic clock (CSAC) mounted on the sensor device. As a prototype, the heterogeneous digital sensing platform achieved the desired performance. In this paper, an autonomous time-synchronized sensing system, which was newly designed and built to be applied to actual bridges, highways and buildings to stably acquire data from a digital accelerometer with accurate time information, image data from a camera sensor and data from any type of analog sensor, based on knowledge obtained in previous development, is reported.**

Keywords-Time Synchronization; Chip Scale Atomic Clock; Earthquake Observation; Structural Health Monitoring; Micro Electro Mechanical Systems; Camera Sensor

I. INTRODUCTION

As civil infrastructure, such as bridges and highways as well as high-rise buildings, deteriorate over time, automation of inspections for their maintenance and management is an important social issue. In addition, Japan is prone to earthquakes and other disasters, so there is a need to detect damage to structures immediately after a disaster and to assess the damage status. Data collection by sensing systems is necessary to automate these inspections and damage detection, but time synchronization across sensors must be ensured in order to analyze the data measured by multiple sensors and evaluate structural viability. Without time-synchronized data, time-series analysis using phase information cannot be performed. Time synchronization methods have been realized using dedicated wiring, wired or wireless networks, etc. However, when wiring is required, it places significant restrictions on the locations where sensors can be installed, and when wireless communication is used, it can be applied only where wireless communication is possible between sensors. In either case, it is impossible to deploy sensors over a wide area. On the other hand, if sensors installed at arbitrary locations can autonomously maintain accurate time information, this problem can be overcome. The method of using Global Positioning System (GPS) signals is effective outdoors, but cannot be used inside buildings, underground, under bridges or in tunnels. Therefore, a sensor device was developed that autonomously maintains accurate time information using a chip-scale atomic clock (CSAC) [2][3][7], which is an ultra-high precision clock [4][8][9]. In order to apply the sensor device to earthquake observation, logic was implemented to detect the occurrence of earthquakes and store data of earthquake events, and its functionality was confirmed in a shaking table experiment. The developed sensor device was also installed in actual buildings and bridges, and applied to earthquake observation and structural viability assessment [4]. However, the sensor device had a MEMS accelerometer, which made it difficult to accurately measure minute vibrations, and there was still a risk of noise contamination in the analog signal. The accelerometer mounted in the sensor device is therefore now a digital type, eliminating the risk of noise [5]. A camera sensor can also be connected to the sensor device, and a heterogeneous digital sensor platform was developed as a prototype [6]. In this paper, details of the autonomous time-synchronized sensing system, newly designed and built based on knowledge obtained from previous research and development, and a mechanism for adding ultra-high-precision time information to sensor data by a CSAC are described.

In this paper, Section II shows the existing time synchronization methods and describes their problems and achievement of the development of digital sensing platform proposed in this research. Section III describes the configuration of autonomous time-synchronized sensing system and the development of the actual sensor device. Further, Sections IV and V describe the performance verification experiments on the time synchronization and the time stamp of developed camera sensor device, respectively. It is confirmed that time synchronization among the developed digital sensor devices with camera is achieved.

II. STATE OF THE ART

Many studies have been done on time synchronization in sensing, including the use of Global Navigation Satellite System (GNSS) signals via satellites, and the Network Time Protocol (NTP) [10] for time synchronization on the Internet. There are also studies that have achieved time synchronization by taking advantage of the characteristics of wireless sensor networks, such as low propagation delay. For example, protocols, such as Reference Broadcast Synchronization, Timing-sync Protocol for Sensor Networks, Flooding Time Synchronization Protocol, etc., have been studied [11]-[15]. However, although time synchronization methods that use wireless technology are convenient, there is no guarantee that wireless communication will always be available. Particularly, if wireless communication is disrupted during a disaster, such as an earthquake, it will be impossible to perform time-synchronized sensing, and data analysis cannot be carried out. Another technology that achieves highly accurate time synchronization indoors is the IEEE 1588 Precision Time Protocol (PTP), which employs Ethernet cables used in general Local Area Networks (LANs) as the transmission path, and time packets to achieve a synchronization accuracy within 1 microsecond. However, it is difficult to ensure stable synchronization accuracy due to fluctuations in packet delay and packet loss due to congestion within the LAN. In addition, because the delay is compensated by packet switching, the number of PTP devices that can be connected to the master device is limited, and it is not possible to deploy them in a Wide Area Network environment, where the delay changes dramatically.

When GPS signals are not available, wireless transmission and reception are unstable, and wired network connections are unavailable, it is nevertheless desirable for sensors to autonomously maintain accurate absolute time information in order to acquire data that ensure long-term, stable time synchronization. If each sensor can provide accurate absolute time information (a time stamp) to the data it measures, sensor data with autonomous time synchronization can be obtained. It was therefore decided to develop a sensor device that autonomously maintains accurate absolute time information by applying a CSAC [2][3][7], which is a clock with high timekeeping accuracy, The CSAC is a clock that can achieve ultra-high accuracy time measurement of the order of tens of picoseconds ($5 \times 10-11$ seconds), while being sufficiently ultra-compact to be mounted on a board. Development began in 2001 with support from Defense Advanced Research Projects Agency (DARPA), and a consumer version was released in 2011. The CSAC is expected to be further miniaturized and lower-priced as it becomes more widely used for applications, such as countermeasures against interference with GPS due to jamming signals, high-precision positioning in environments without access to GPS signals, installation in smartphones and advanced disaster monitoring. CSACs have a smaller error by 4 to 8 digits than that of timekeeping using a crystal oscillator, NTP or GPS signals, which are commonly used in sensor devices. If this CSAC is installed in each sensor device and a mechanism implemented to add a high-precision time stamp to the sampling of measured data, time-synchronized sensor data can be collected even when GPS signals are unavailable, wireless transmission/reception is unstable, and wired network connections are not available. In previous development, the sensor device had an analog MEMS accelerometer, and the system configuration was such that any analog sensor could be connected via an external input interface. However, since the accuracy of an analog MEMS accelerometer was not high and the risk of noise contamination of the analog signal remained, it was decided to develop a fully digital sensing platform. Specifically, a digital accelerometer was installed in the sensor device to enable highly sensitive acceleration measurement without the risk of noise contamination, while a camera sensor could also be connected, and a technology was developed to accurately time-stamp both digital outputs using the CSAC. The data acquired by the sensor device described in this paper, which ensure time synchronization, can be used for the purpose of civil infrastructure inspection and structural viability assessment of buildings.

III. AUTONOMOUS TIME-SYNCHRONIZED SENSING SYSTEM AND CIRCUIT CONFIGURATION

If an ordinary sensor device is provided with a CSAC to correct the time information of the CPU and perform measurement, the CSAC's timekeeping accuracy is too high, which results in a delay. Therefore, to add the time information of the CSAC directly to the sensor's measurement data by hardware, a mechanism was implemented using a Field-Programmable Gate Array (FPGA), which is a dedicated integrated circuit. In this way, measurement data with absolute time information added by the FPGA are stored in a storage device and collected over a network, without putting an excessive load on the CPU of the sensor device. Moreover, since the FPGA is programmable, it can not only handle CSAC time information but can also incorporate logic for detecting the occurrence of earthquakes and fires using the measurement data. In this paper, a mechanism whereby accurate CSAC time stamps are added to the outputs of a digital-type accelerometer, a camera sensor and an external analog input, is described.

A. System Configuration

As shown in Figure 1, the sensor device developed in this research consists of an oscillator and FPGA that synchronize GPS time (GPST) with a CSAC, provide a stable reference signal, and maintain absolute time information; a sensor section with a digital accelerometer and an external analog sensor input interface; a signal processing board with a CPU;

and a camera for capturing images. The oscillator and FPGA supply a high-precision 10 MHz reference clock and 1 Pulse Per Second (PPS) signal, and the FPGA generates time stamps and trigger signals for acquiring data. The sensor section comprises a digital accelerometer and an external analog sensor input interface. Any analog sensor can be connected to the external analog sensor input interface. The digital accelerometer outputs data in response to a trigger signal via a Universal Asynchronous Receiver/Transmitter (UART). Data from the sensor connected to the external analog sensor input interface are converted by A/D converters in response to trigger signals, and output as 16-bit serial values. The camera sensor can release the shutter in response to a trigger signal, and output RGB values. The acquired data are stored in a connected Solid-State Drive (SSD). Camera data and sensor data are stored on separate SSDs in consideration of access speed. This data can be viewed, retrieved or deleted via the network by taking out each SSD, or by using the system's file server function. Operations, such as measurement setup, time setting and operation mode change are performed via the network. As for the network, the system has an internal wired LAN and Wi-Fi, so users can choose either one.

B. Oscillator and FPGA

Figures 2 and 3 show the configuration and appearance of the oscillator and FPGA sections. The oscillator and FPGA sections have the function of synchronizing the CSAC with 1 PPS output from the GPS module or 1 PPS input from outside, and generate triggers to be input to the sensors and camera in the FPGA from the 10 MHz clock of the CSAC. The trigger signals thus generated are synchronized with the 1 PPS of the CSAC, which is synchronized with the GPS.

When performing time synchronization across multiple sensor devices, all sensor devices can be set as "master", or one sensor device can be set as "master" and the other sensor devices can be set as "slaves." When a sensor device is a "master," it receives the GPS signal, and inputs the 1 PPS from the GPS module to the CSAC to synchronize the GPS with the CSAC. If the sensor device is a "slave," the master and slave are synchronized by inputting the 1 PPS output from the "master." In addition, commands to set the CSAC synchronization period or reset the CSAC 1 PPS phase value, and a command to select either the GPS or an external input, are executed from the signal processing board on the CSAC and FPGA via a connector. The 10 MHz and 1 PPS output from this board is the clock source for this system. Due to a combination of the frequency stability of the GPS and CSAC, the synchronization period is set to 1000 seconds so that the time can be maintained for a long period even if the GPS is interrupted.

C. Sensor board

Figures 4 and 5 show the configuration and appearance of the sensor section. The sensor section comprises a digital accelerometer and an external analog sensor input interface. The data from the digital accelerometer can be sampled at 1 kHz at the time of the trigger. The external analog sensor input interface has three channels for connecting an analog accelerometer for comparison with the digital accelerometer.

Depending on the purpose of measurement, any analog sensor can be connected in addition to the analog acceleration sensor.
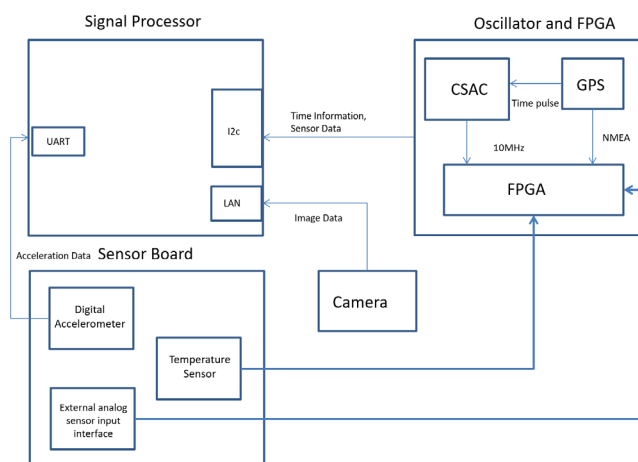

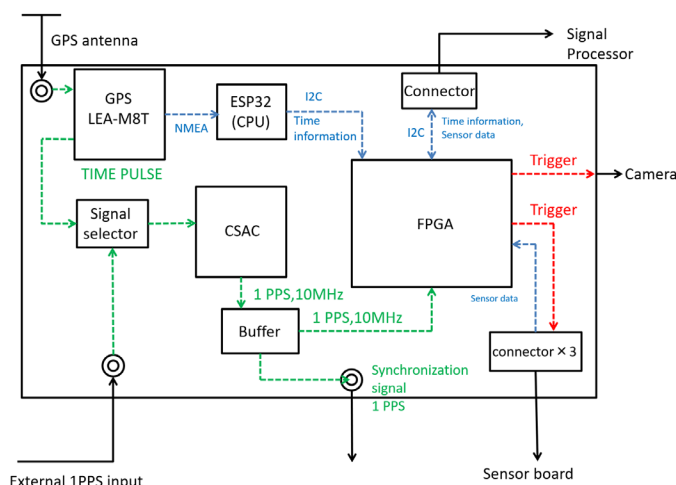Figure 1. System configuration.

Figure 2. Oscillator and FPGA.

Figure 3. External appearance of oscillator and FPGA.

The signal input from the external analog sensor interface is converted by an A/D converter and output as a 16-bit serial value, but by splitting the signal into two channels and amplifying one of them 64 times, an A/D converter with 16-bit resolution can obtain a resolution equivalent to 22-bits. Data from the digital accelerometer are output to the FPGA via the UART, and data from the sensor connected to the external analog sensor input interface are output via a Serial Peripheral Interface (SPI).
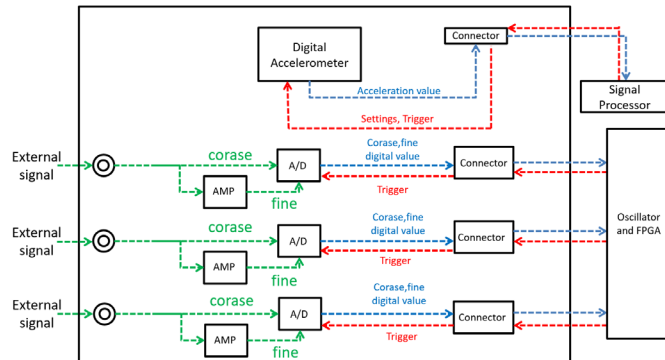

Figure 4.   Sensor board.
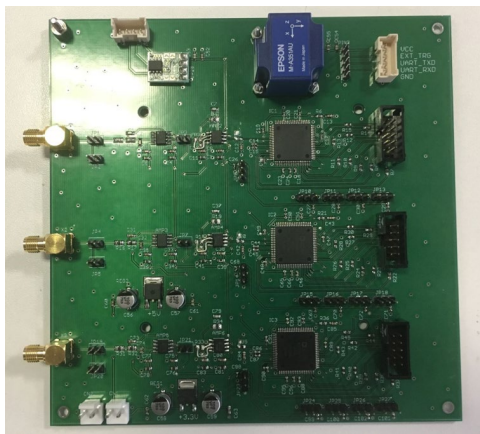
Figure 5.   External appearance of Sensor board.

D. Signal processor

Figures 6 and 7 show the configuration and appearance of the signal processor. For the signal processor, the Raspberry Pi 4 shown in Table 1 is used. As shown in Table 1, Ubuntu is installed as the CPU OS, an SSD can be used via USB 3.0, camera communication is possible via Gigabit Ethernet, and an internal Wi-Fi antenna can be connected. Internal data can be retrieved and viewed via the LAN (Wi-Fi) using Samba functions, and Secure Shell (SSH) can be used to configure settings and start measurements. In addition to the above functions, the CPU mainly performs time setting, sorting of acquired data, format conversion, filing, and processing of image data from the camera.

E. Digital accelerometer

Figure 8 and Table 2 respectively show the appearance and specifications of the digital accelerometer mounted on the

sensor board. The digital MEMS accelerometer mounted on the sensor board has a 3-axis crystal acceleration sensor with high accuracy and excellent stability, which is micro-fabricated from a highly accurate and stable crystal material. As shown in Table 2, it has low noise and low power consumption and is capable of high-resolution vibration measurement.
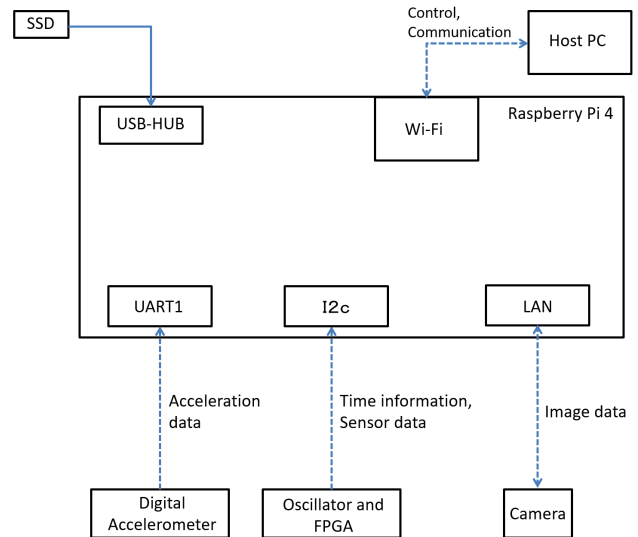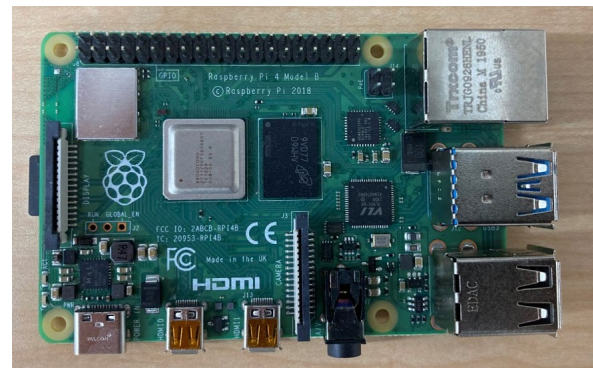

Figure 6.   Signal processor.

Figure 7.   External appearance of Signal processor.

TABLE I.   SPECIFICATIONS OF SIGNAL PROCESSOR

OS	Ubuntu 20.04.2 LTS
CPU	(GNU/Linux 4.5.0-00185-g3bb556b armv7l)
Memory	1.5GHz quad-core Cortex-A72 (ARM v8) 64-bit SoC
LAN	8GB
USB	RJ-45×1：IEEE802.3i（10BASE-T）、IEEE802.3u（100BASE-TX）、IEEE802.3ab（1000BASE-T）
UART	USB3.0 Standard A Connector×2
FPGAROM	UART×2
Storage	16GB(MicroSD,OS)

Figure 8.   Digital Accelerometer.

TABLE II.   SPECIFICATIONS OF DIGITAL ACCELEROMETER

Model	EPSON M-A352VD10
Range	±15 G
Noise Density	0.2 µG/√Hz (Average)
Resolution	0.06 µG/LSB
Bandwidth	460 Hz
Output Range	1000 sps (selectable)
Digital Serial Interface	SPI
Outside Dimensions (mm)	48 × 24 × 16
Weight	25 grams
Operating Temperature	-30 ℃ to +85 ℃
Power Consumption	3.3 V, 13.2 mA(Typ.)

F. Camera sensor

Figure 9 and Table 3 respectively show the appearance and specifications of the camera sensor. Baumer VCXG-02C, a high-speed Gigabit Ethernet camera module, was used as the camera sensor.

It is compact, has low power consumption, has excellent performance in low-light environments, and can acquire images at the time of a trigger by inputting an external trigger. Furthermore, it features reliable and stable data transfer with an internal buffer for retransmission, and is equipped with an overlap trigger mode that allows trigger shooting at a frame rate equivalent to free-run shooting.

Figure 9.   Camera sensor.

TABLE III.   SPECIFICATIONS OF CAMERA SENSOR

Model	Baumer VCXG-02C
Active Array Size	640 x 480
Sensor	CMOS ON Semiconductor： PYTHON 300
Pixel Size	4.8 μ m x 4.8 μ m
Shutter	Global Shutter
Power Supply	12-24 VDC/2.6W
Image Formats	BayerRG / RGB / BGR / Mono
Frame Rate(fps)	401(640 x 480)
Exposure Control	20µsec ～ 1sec
Operation Mode	Trigger/Free Run
Size(mm)	29 × 29 × 49
Weight(g)	120
Interface	GigabitEthernet（1000BASE）/ FastEthernet（100BASE）

Rolling shutter is a capture method that scans the entire frame vertically or horizontally. From the point of view of time-synchronized sensing, the biggest drawback of the rolling shutter is that it does not capture the same moment. Scanning itself is performed at high speed, but there is a time difference in the photographed object due to the sequential scanning. To overcome this shortcoming, a global shutter camera was adopted, which shoots a frame at a time. This allows for accurate timestamping of each captured image.

IV.   TIME SYNCHRONIZATION PERFORMANCE EXPERIMENT OF THE CAMERA SENSOR

An experiment was conducted to verify the camera sensor's time synchronization performance. Figure 10 shows the experimental system configuration. A trigger signal generated by the oscillator and FPGA section is simultaneously sent to the camera sensor and LED control FPGA. Since the shutter of the camera sensor is synchronized with the lighting state of the LEDs, if images are acquired in accordance with the transition in the lighting state, it is considered that trigger-synchronized images are being acquired. The source of this signal is the CSAC, which is synchronized with the trigger signal passed to the sensor section, so the sensor and the camera sensor are synchronized.
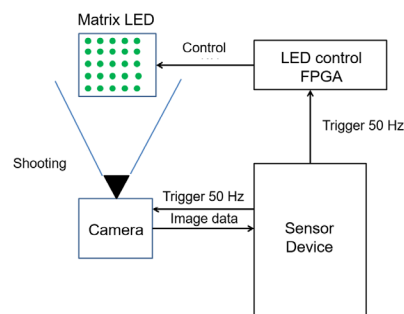

Figure 10. Camera data measurement system.

The FPGA for LED control is configured to control the lighting of the LEDs at the time of the trigger signal clock (50 Hz). With a 5 x 5 LED matrix, the LEDs light from upper left to lower right, one by one, in accordance with the rising edge of the trigger signal. The camera sensor is fixed to photograph the LED matrix. Figure 11 shows the pictures taken by the camera sensor. Time elapses in 20 ms increments from upper left to lower right. Since the LEDs in the photos light one by one, images are acquired according to the signals input to the FPGA for LED control. In this figure, the period of 1 horizontal line of LEDs is 100 ms as the number of LEDs in each line is five. Each vertical line in the images is every 100 ms, and since all the LEDs are lit in the same way, none are left out. From these results, it was confirmed that images can be continuously acquired in synchronization with the trigger from the sensor device.
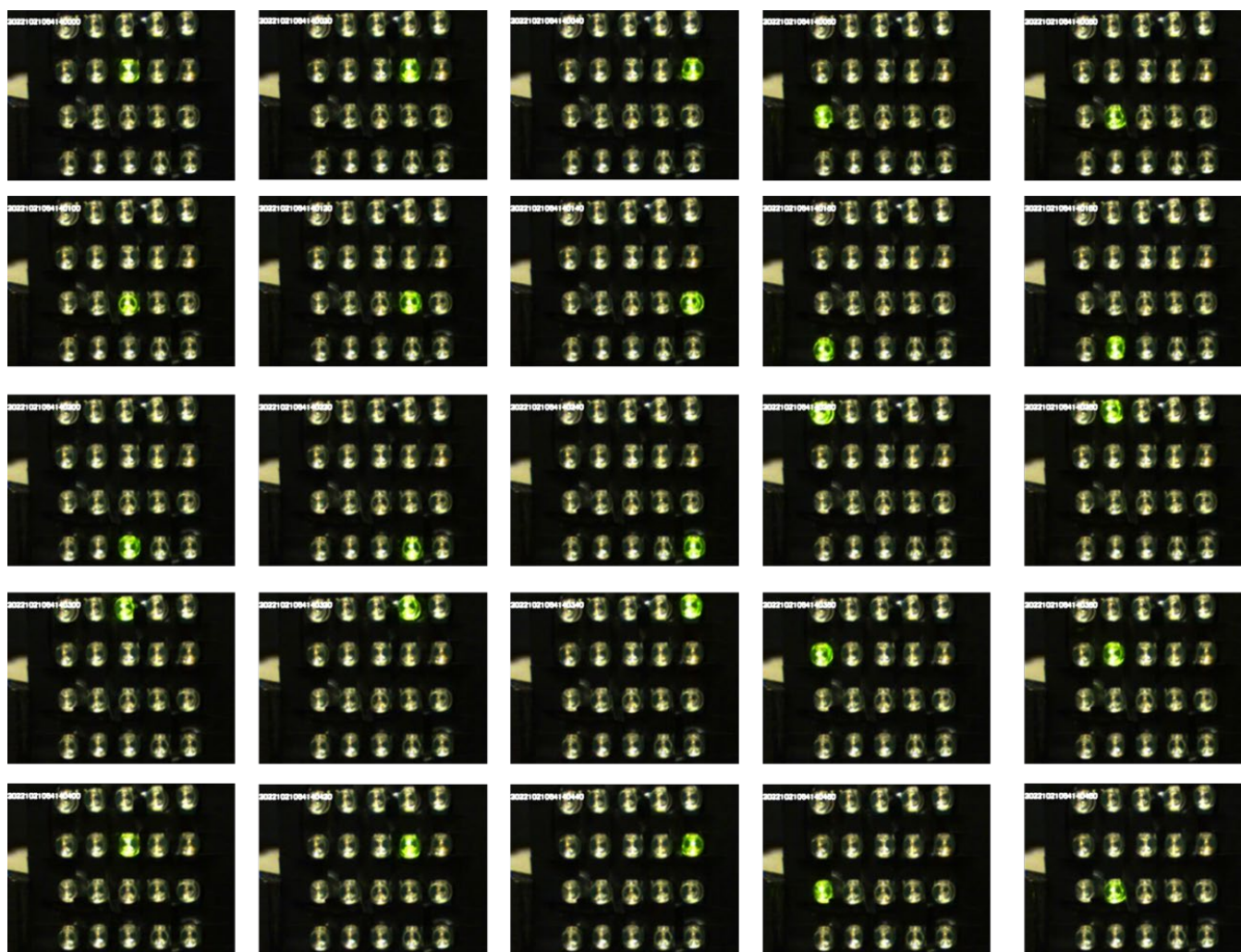

Figure 11. Continuous images from the experimental result.

The performance verification experiment on the time synchronization of developed camera sensor device was carried out as shown above. It is confirmed that time synchronization among the developed digital sensor devices with camera is achieved. The development of this digital sensing platform has enabled time-synchronized measurements between digital accelerometers, camera sensors, and many types of external input analog sensors, as well as multimodal analysis between measurement data.

V. TIME STAMP VERIFICATION EXPERIMENT

The time stamps added to the images acquired by the camera sensor were experimentally verified. Figures 12 and 13 show the experimental system configuration and GPS module, respectively. The camera sensor was used to capture images of the LEDs on the GPS module to see whether the increase in the number of seconds coincided with the seconds of the time stamp. When the power is turned on, the LED of TP1 turns off at a timing of 1 PPS of the GPS. The time to turn off the LED can be determined with a pulse width of 1 PPS,

which in this case is 100 ms. In other words, the LED is OFF for 100 ms and ON for 900 ms every second. Figure 14 shows the results obtained every 20 ms. Since the time when the LED is OFF is set to 100 ms, the five images from 000 ms to 080 ms capture the state of the LED when it is OFF, and it can be seen that after 100 ms, the LED is ON, indicating that the seconds of the time stamp coincide with the OFF state of the LED. Figure 15 shows photos after 980 ms. After 980 ms, the LED is lit, but after the next 000 ms, it turns off, and after 100 ms, it is lit again.
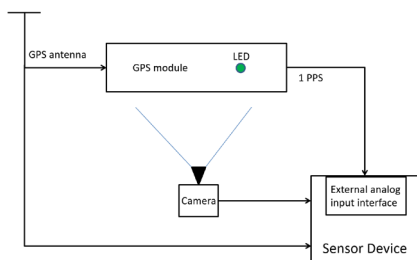
Figure 12. Experimental system configuration for time stamps.

Figure 13. GPS module overview.

| (a) 01:08:58.000 | (b) 01:08:58.020 | (c) 01:08:58.040 |
| (d) 01:08:58.060 | (e) 01:08:58.080 | (f) 01:08:58.100 |
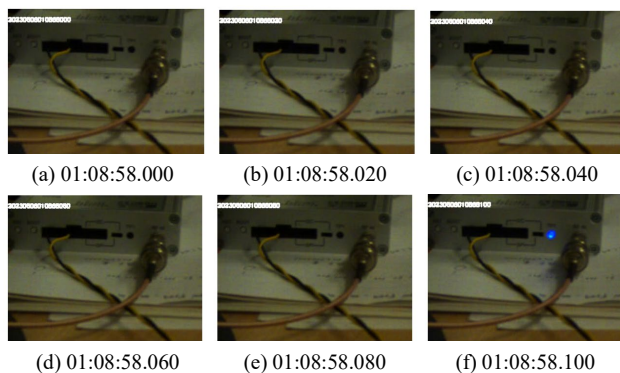
Figure 14. Sequential photos of experimental results.

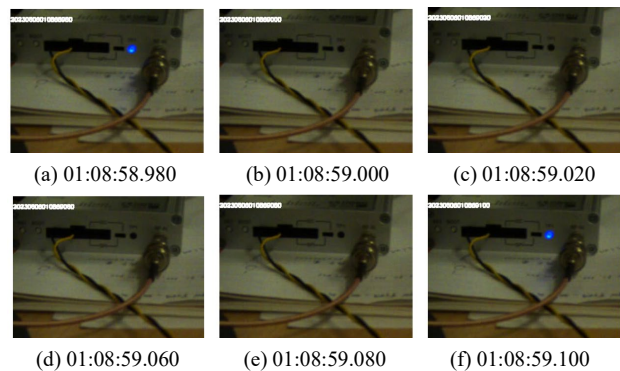| (a) 01:08:58.980 | (b) 01:08:59.000 | (c) 01:08:59.020 |
| (d) 01:08:59.060 | (e) 01:08:59.080 | (f) 01:08:59.100 |

Figure 15. Sequential photos of experimental results (after 980 ms).

From the above results, it was confirmed that 1 PPS of the GPS coincides with the seconds of the time stamp. Since the camera takes photos every 20 ms, it was thus possible to verify that actual phenomena coincided with the images, at least to within 20 ms.

VI. CONCLUSION

In this paper, the development of an autonomous sensing system that maintains highly precise absolute time information by applying a CSAC was reported. First, an autonomous time-synchronized sensing system and its circuit configuration were described, and a mechanism for adding ultra-high-precision absolute time information to sensor data by the CSAC, and the development of a sensor device, were described in detail. A function to add the same time stamp to the output from a camera sensor, the output from an internal digital accelerometer and the input from an external analog input interface, was implemented. The results of experiments to verify the time synchronization performance of the camera sensor were also reported. It is planned to verify the time synchronization performance of this new sensing system with regard to measurement data obtained by the camera sensor, the internal digital accelerometer and the external analog input sensor.

REFERENCES

[1] N. Kurata, "Disaster Big Data Infrastructure using Sensing Technology with a Chip Scale Atomic Clock," World Engineering Conference and Convention (WECC2015) WFEO, Dec. 2015, pp. 1-5.

[2] N. Kurata, "Basic Study of Autonomous Time Synchronization Sensing Technology Using Chip Scale Atomic Clock," 16th International Conference on Computing in Civil and Building Engineering (ICCCBE2016) ISCCBE, July 2016, pp. 67-74.

[3] N. Kurata, "An Autonomous Time Synchronization Sensor Device Using a Chip Scale Atomic Clock for Earthquake Observation and Structural Health Monitoring" The Eighth International Conference on Sensor Device Technologies and Applications (SENSORDEVICES 2017) IARIA, Sep. 2017, pp.31-36, ISSN: 2308-3514, ISBN: 978-1-61208-581-4

[4] N. Kurata, "Seismic Observation and Structural Health Monitoring of Buildings by Improved Sensor Device Capable of Autonomously Keeping Accurate Time Information," International Journal on Advances in Systems and Measurements, IARIA, vol 12, no 1&2, pp. 41-50, 2019.

[5] N. Kurata, "Digital Sensing Platform with High Accuracy Time Synchronization Function for Management of Buildings and Cities," The Tenth International Conference on Sensor Device Technologies and Applications (SENSORDEVICES 2019) IARIA, Oct. 2019, pp. 53-58, ISSN: 2308-3514, ISBN: 978-1-61208-745-0

[6] N. Kurata, "High-precision Time Synchronization Digital Sensing Platform Enabling Connection of a Camera Sensor," The Twelfth International Conference on Sensor Device Technologies and Applications (SENSORDEVICES 2021) IARIA, Nov. 2021, pp. 98-104, ISSN: 2308-3514, ISBN: 978-1-61208-918-8

[7] S. Knappe, et al., "A Microfabricated Atomic Clock," Applied Physics Letters, vol. 85, Issue 9, pp. 1460-1462, Aug. 2004, doi:10.1063/1.1787942.

[8] Q. Li and D. Rus, "Global Clock Synchronization in Sensor Networks," IEEE Transactions on Computers, vol. 55, Issue 2, pp. 214-226, Jan. 2006, ISSN: 0018-9340.

[9] R. Lutwak, et al., "The Chip-Scale Atomic Clock - Prototype Evaluation," 39th Annual Precise Time and Time Interval (PTTI) Meeting, Nov. 2007, pp. 269-290.

[10] D. Mills, "Internet Time Synchronization: the Network Time Protocol," IEEE Transactions on Communications, vol. 39, Issue 10, Oct. 1991, pp. 1482-1493, doi:10.1109/26.103043.

[11] M. Maroti, B. Kusy, G. Simon, and A. Ledeczi, "The Flooding Time Synchronization Protocol," Proc. the 2nd International Conference on Embedded Networked Sensor Systems (SenSys '04) ACM, Nov. 2004, pp. 39-49, doi:10.1145/1031495.1031501.

[12] J. Spilker Jr., P. Axelrad, B. Parkinson, and P. Enge, "Global Positioning System: Theory and Applications," Vol. I, American Institute of Aeronautics and Astronautics (AIAA), 1996, ISBN: 978-1-56347-106-3.

[13] J. Elson, L. Girod, and D. Estrin, "Fine-Grained Network Time Synchronization using Reference Broadcasts," Proc. 5th Symposium on Operating Systems Design and Implementation (OSDI'02), Dec. 2002, pp. 147-163, doi:10.1145/844128.844143.

[14] S. Ganeriwal, R. Kumar, and M. B. Srivastava, "Timing-sync Protocol for Sensor Networks," Proc. the 1st International Conference on Embedded Networked Sensor Systems (SenSys '03) ACM, Nov. 2003, pp. 138-149, doi:10.1145/958491.958508.

[15] K. Romer, "Time Synchronization in Ad Hoc Networks," Proc. the 2nd ACM International Symp. on Mobile Ad Hoc Networking & Computing (MobiHoc'01) ACM, Oct. 2001, pp. 173-182, doi:10.1145/501436.501440.

Beam-shaping for a LIDAR System for Urban Scenarios

Marcus Baumgart[1], Rainer Reichert[3], Boris Kirillov[2], Marcus Hennecke[2], Martin Pfennigbauer[3], Andreas Hofbauer[3], Andreas Tortschanoff[1]

[1]Photonics Systems, Silicon Austria Labs, Villach, Austria

[2]Infineon Technologies Austria, Graz, Austria

[3]Riegl, Horn, Austria

E-mail address of the corresponding author: andreas.tortschanoff@silicon-austria.com

Abstract—**Automotive LIDAR sensors are generally considered as enabling technology for higher-level autonomous driving. Different concepts to design such a sensor can be found in the industry. In the course of an Austrian research project, a MEMS based LIDAR system for automotive applications is currently developed and within this paper we describe the overall system concept and, in some detail, the requirements and the design of the emitter optics which turn out to be rather complex, in order to enable the sensor to detect objects of about 10 cm x 13 cm size at a distance of 80 m and a field-of-view of 20° x 90.**

Keywords—LIDAR; MEMS; scanner; beam shaping.

I. INTRODUCTION

Light detection and ranging (LIDAR) is arguably one of the key components for future autonomous driving and there is much interest in developing robust, compact and price-effective solutions. Consequently there has been a lot of research in recent years [1],[2],[3],[4]. Among different scanning technologies, Microelectromechanical Systems (MEMS) scanning mirrors provide unrivalled advantages in terms of size, speed and cost over other types of laser scanners, making them ideal for LiDAR in a wide range of applications [5].

Current Advanced Driver Assistance Systems (ADAS) focus on comparatively simple scenarios with objects behaving in predictable ways, such as highway traffic or parking assistance without pedestrians, cyclists or transversal traffic. Yet, there is an urgent need to extend ADAS and Automated Driving (AD) to handle urban traffic scenarios. Also, the 'European new car assessment programme' now defines test cases that involve Vulnerable Road Users (VRUs) such as adult pedestrians, children and cyclists in urban scenarios [6].

For complex scenarios, like urban traffic, high resolution and large field of view is a key requirement, which is challenging to achieve. The Austrian project "Integrated LIDAR Sensors for Safe & Smart Automated Mobility" (iLIDS4SAM) addresses this issue by developing a novel LIDAR-based system for predictive assessment of hazardous situations involving VRUs in an urban setting [7]. Within this project a compact LIDAR system, based on a MEMS scanner mirror is developed.

The remaining of the paper is structured as follows. Section II presents the general concept of the ilids4sam-LIDAR. In Section III we describe in detail the emitter-optics and, finally, in Section IV provide a short summary and outlook.

II. CONCEPT

As outlined above the targeted scenario of urban traffic necessitates high resolution, large field of view and robust operation under ambient light conditions. The target specifications, we deduced for the LIDAR system, are listed in Table 1.

TABLE 1: TARGET SPECIFICATIONS OF THE LIDAR SYSTEM

Quantity	Target-specification
Wavelength	905 nm
Field of view	60° x 20 °
Distance	Up to 80 m
Resolution	<0.07° (≙ 10cm@80m)
Depth resolution	30 cm
Framerate	25 fps

The key component of the LIDAR is a 1D MEMS scanner mirror [8], which is electrostatically actuated. In its latest generation, the MEMS features a mirror-diameter of 5 mm, a mechanical amplitude of the tilting angle of 10° (corresponding to an optical scanning range of 40°) and a frequency of 2 kHz.
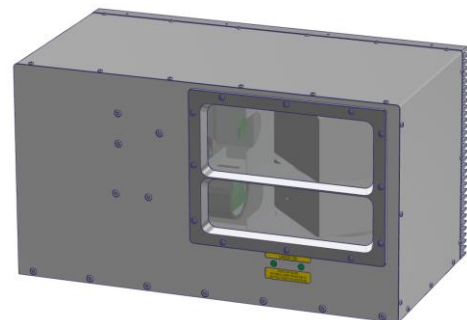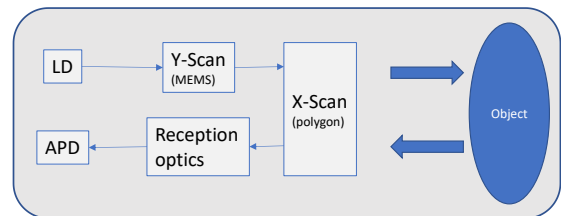

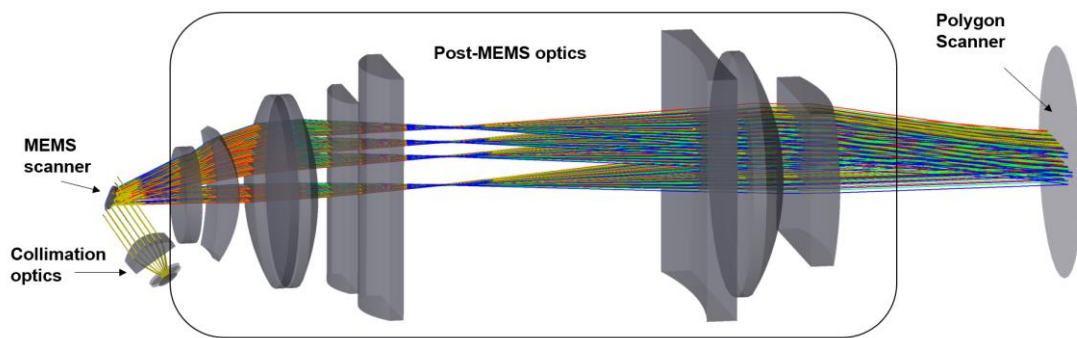Fig. 1. Overall system concept and design of the full system.

Fig. 2: Optical layout of the LIDAR emitter optics comprise a collimation of the laser diode stack, the MEMS scanner mirror and a multi element lens for beam shaping.

The concept foresees that the beam is scanned via this MEMS in one direction, while the second dimension is scanned via a subsequent larger polygon scanner. This approach enables scanning of the required field of view and use of a large second scanner enables high collection efficiency of the back scattered light in the corresponding dimension. Thus, for one dimension, the light collection can be performed behind the scanning optics, which significantly reduces background light levels on the detectors, because only back reflected light is detected. Thus, rather than observing the whole scene, the detector channel only detects a line, strongly improving signal to noise, in particular, for the (realistic) situation of strong background from sunlight.

Since LIDAR is based on measuring the backscattered light system, the measurement time for an individual point cannot be arbitrary short for long range LIDAR based on pulsed time of flight (e.g., a minimum waiting time of ~0.5 µs is required for 80m distance). Therefore, it would not be possible to measure the required point-cloud with the specified density and framerate by pure point-scanning. Some way of multiplexing is required. While in previous realizations, relying on pure 1D scanning, a vertical line was scanned and detected with a linear detector array, here we follow a hybrid approach and scan in two dimensions, albeit still the measurement is multiplexed by projecting a line, which is detected on a line-detector with 16 APDs.

While this paper focuses on the beamshaping, performed in the emitter branch, a more detailed description of the overall LiDAR system can be found in [9]. Most relevant for this presentation are the resulting requirements for the scanned laser beam. Besides ensuring that the whole FOV is scanned as efficiently as possible, there are stringent requirements on the beam-profile. The beam should ideally feature a top hat profile in the form of a thin line, with minimal vertical divergence, but an accurately defined horizontal divergence with a full width of 1.5°.

III. EMITTER DESIGN

The crucial part of the overall LIDAR system, is the design of the emitter optics which have to fulfill the following requirements:

- Collimation of the laser diode bar to a beam with well-defined asymmetric divergence.
- Fine calibration of the field of view of the sensor since the mirror maximal amplitude does not well correspond to the whole FOV.

Simulations were performed using Zemax, Opticsstudio.

The overall optical layout is shown in Fig. 2. It consists of sub-units, namely the laser diodes and first beam collimation, the MEMS scanner mirror, which scans the beam in one dimension and subsequently beam shaping optics to generate the required characteristics, before hitting the second scanner device, which is a rotating polygon mirror. These elements are shortly outlined in the following.

A. Collimation

The laser diode is a stack with 8 emitters with a pitch of 400 µm and each consisting of 3 epitaxially stacked emitters, resulting in three stacked lines in the emission profiles.

Collimation of this stack is done using a cylindrical lenslet array placed at a distance of 1mm in front of the emitting facets for slow axis collimation and, a fast axis collimation, placed at a larger distance, for beam collimation of the vertical axis, where small divergence is required.
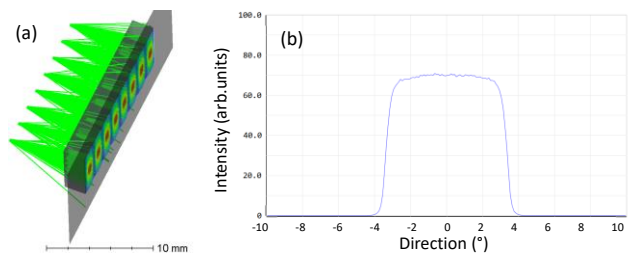

Fig. 3: (a) laser diode with a cylindrical lenslet array for slow axis collimation, (b) angular profile of combined beam in slow axis

As shown in Fig. 3, in this configuration we can achieve a nearly perfect top-hat-profile in angular space for the slow

axis collimation. The divergence still has to be reduced by a factor of 4 in order to achieve the targeted divergence of 1.5°. This step is performed by telescope-optics after the MEMS.

For fast axis collimation an aspheric lens with a focal distance of 4 mm is used, in order to collimate the beam in the vertical axis.
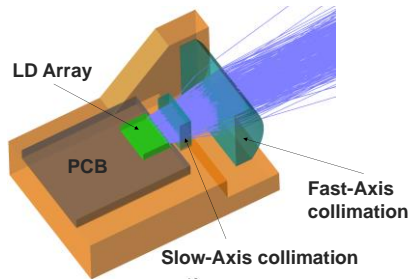

Fig. 4: 3D sketch of the laser diode collimation.

A sketch of the arrangement of the laserdiode bar and the cylindrical collimation optics is shown in Fig. 4 and Fig. 5 shows the beam profile, which is obtained after collimation directly in front of the MEMS scanner.
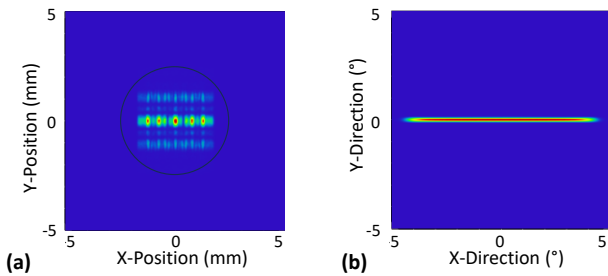
Fig. 5: Beam profile directly after collimation before the MEMS mirror: (a) intensity distribution (b) radial distribution

B. MEMS

The MEMS mirror is an electrostatically driven scanner. It has a diameter of 5 mm, and a mechanical amplitude of +/-10°. It´s resonance frequency is above 2kHz, which makes it very insensitive to mechanical vibrations.
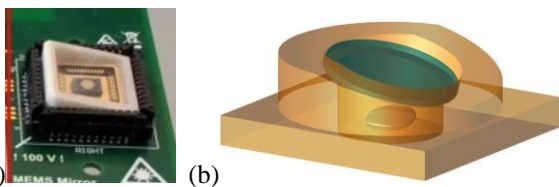

Fig. 6: (a) typical MEMS scanner mirror [4] (b) housing with tilted cap

In the set-up the MEMS is hit by the beam under a small angle of 30° for efficient coverage of the mirror area. Furthermore, it is packaged with a tilted cover window, so that the static reflection from the window does not lie within the field of view of the LIDAR scanner.

C. Telescope for beam shaping

Following the MEMS element, we have designed an anamorphic telescope, which provides a magnification of 2x and 4x for horizontal and vertical direction, respectively. This ensures that the field of view generated by the MEMS scanner is reduced from 40° optical scan to the 20°, which are the target value for the vertical FOV. Also, the 4x magnification decreases the vertical divergence of the beam to <0.07°, which matches to the required resolution.

The telescope design (see Fig. 7) includes eight lens-elements. Several simpler designs were also evaluated, but they did not provide sufficient quality.
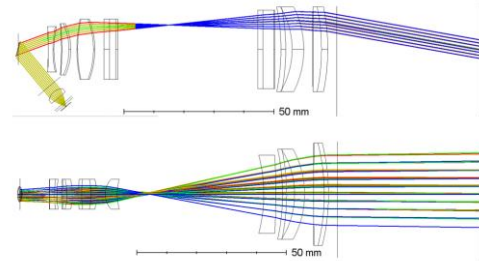

Fig. 7. Side-view and top-view of the optical design of the telescope optics.

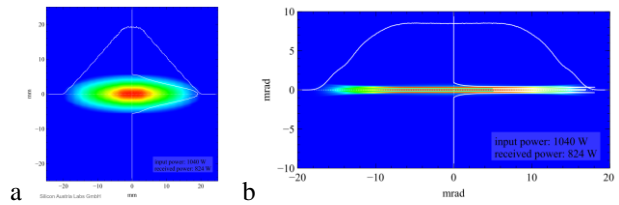As demonstrated in Fig. 8, this design provides the required specifications.

Fig. 8 Beam profile in the (a) nearfield and (b) farfield (Note that for the near-field the spatial and for the far-field the angular distribution is plotted.)

The differences in magnification for the horizontal axis, depending on MEMS tilt angle and y-aberrations due to axes crosstalk are noticeable and partially impact performance. This can be seen in the far field pattern, shown in Fig. 9.
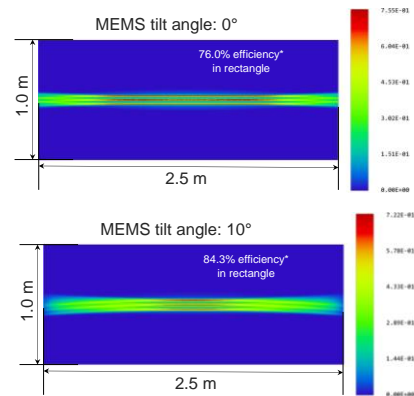

Fig. 9 Far-field intensity distribution at a distance of 80m for mirror tilt angles of 0° and 10°, which is the maximal tilt.

D.   Overall system assembly

For the first demonstrator system, based on the presented design, we aim for an elegant breadboard style with still a partially adjustable mechanical frame for the optical system, including e.g., translational stages, since tolerances of some of the components are ill defined. Furthermore, we were aiming at the use of standard components as far as possible, rather than pushing towards maximal miniaturization.

Fig. 10 shows a photo of the first assembled emitter unit mock-up, where, however, still some functional components are missing.
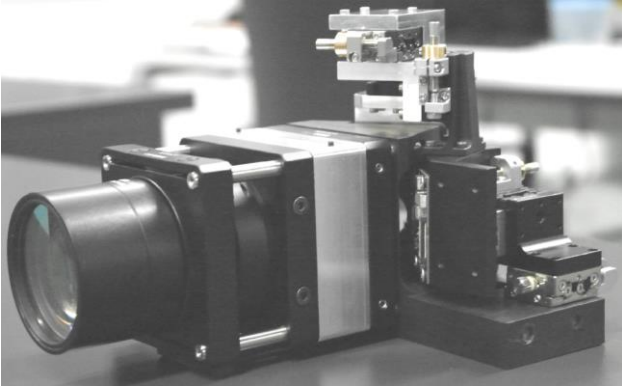

Fig. 10: Picture of the assembled emitter unit, waiting for the final components and electronics.

IV. CONCLUSIONS AND OUTLOOK

We presented an overview of the design of the emitter part for a LIDAR system, which is under development. In the simulations presented we could fulfill all requirements and specifications. The assembly of a demonstrator on the level of elegant breadboard is ongoing and first results from characterization of the emitter unit, as well as the complete LIDAR sensor, are expected in the next months. The complete LIDAR system will be tested in real-word use-cases. Further developments will target miniaturization and a ruggedized and cost optimized version.

REFERENCES

[1] Y. Li and J. Ibanez-Guzman, "Lidar for autonomous driving: The principles, challenges, and trends for automotive lidar and perception systems." IEEE Signal Processing Magazine, 37(4), 50-61 (2020), doi:10.1109/MSP.2020.2973615;

[2] R. Roriz, J. Cabral, and T. Gomes, "Automotive LiDAR technology: A survey." IEEE Transactions on Intelligent Transportation Systems, 23(7), 6282-6297 (2021), doi:10.1109/TITS.2021.3086804

[3] H. Holzhüter, J. Bödewadt, S. Bayesteh, A. Aschinger, and H. Blume, "Technical concepts of automotive LiDAR sensors: a review". Optical Engineering, 62(3), 031213-031213 (2023), doi:10.1117/1.OE.62.3.031213

[4] T. Goelles, B. Schlager, and S. Muckenhuber, "Fault detection, isolation, identification and recovery (fdiir) methods for automotive perception sensors including a detailed literature survey for lidar". Sensors, 20(13), 3662 (2020), doi: 10.3390/s20133662

[5] D. Wang, C. Watkins, and H. Xie, "MEMS mirrors for LiDAR: A review." Micromachines, 11(5), 456 (2020), doi:10.3390/mi11050456

[6] https://www.euroncap.com/en/for-engineers/protocols/vulnerable-road-user-vru-protection/ (visited 09/07/2023)

[7] https://www.ilids4sam.at (visited 08/2/2023)

[8] H.W. Yoo, N. Druml, D. Brunner, C. Schwarzl, T. Thurner, M. Hennecke, and G. Schitter, G. "MEMS-based lidar for autonomous driving". *Elektrotech. Inftech.* **135**, 408–415 (2018)

[9] A. Hofbauer, R. Reichert, M. E. Hennecke, M. Baumgart, and A. Tortschanoff, "Design and development of an integrated LiDAR sensor for autonomous driving", Proceedings of SPIE Sensors and Imaging, 12737-29, (2023)

[10] N. Druml, I. Maksymova, T. Thurner, D. van Lierop, M. Hennecke, and A. Foroutan, "1D MEMS micro-scanning LiDAR," Conference on Sensor Device Technologies and Applications (SENSORDEVICES 2018), Sept. 2018, ISBN: 978-1-61208-660-6

Automated Guidance Based on indoors Visible Light Communication

Paula Louro, Manuela Vieira, Manuel Augusto Vieira

DEETC/ISEL/IPL,
R. Conselheiro Emídio Navarro, 1959-007
Lisboa, Portugal

CTS-UNINOVA
Quinta da Torre, Monte da Caparica, 2829-516,
Caparica, Portugal

e-mail: plouro@deetc.isel.pt, mv@isel.ipl.pt, mv@isel.pt

Abstract— **Wireless communication devices have generated growing interest in indoor navigation over the past few years. The Internet of Things (IoT) and the inherent connectivity of billions of devices are making indoor localization and proximity detection increasingly attractive. Global Positioning System (GPS) has poor, unreliable performance when used in closed spaces, requiring alternative techniques and wireless technology. Due to the unlicensed free spectrum, optical wireless technologies are currently playing an important role in this field. Light Emitting Diodes (LEDs) are the basis for Visible Light Communication (VLC) technology due to their ability to simultaneously provide low energy consumption light and enable the possibility of wireless communication. These features empowered VLC as an effective communication technology due to the ubiquity of the illumination spots, especially in indoor applications. We propose the use of Visible Light Communication (VLC) to support guidance and communication for signaling in an indoor environment. The research focuses on developing guidance VLC systems, transmitting control data information, and decoding techniques. The communication system uses RGB white LEDs as emitters and pinpin photodiodes with selective spectral sensitivity as receivers. The downlink communication occurs between the infrastructure and the mobile user, while uplink communication occurs in the opposite direction. Different modulation methods, such as On-Off keying and Manchester codes, are used, allowing a comparison between them. The decoding strategy is based on accurate calibration of the output signal. We will discuss coding schemes, modulation formats, and decoding algorithms in this paper, as well as the characteristics of transmitters and receivers.**

Keywords - Visible Light Communication; positioning; footprint map, On-Off keying, Mancheste coding.

I. INTRODUCTION

Light emitting diodes (LEDs) are the basis for Visible Light Communication (VLC) technology due to their ability to simultaneously provide low energy consumption light and enable the possibility of wireless communication. Due to the widespread of the LED light spots, especially in indoor applications, these features enabled VLC as a communication technology [1][2]. The high bandwidth and immunity to electromagnetic interference of VLC make it a promising option for future generations (5G/6G) of wireless communications, as it is a good candidate for indoor interconnection and networking in parallel with radiocommunications [3][4]. In addition to its high capacity, unregulated spectrum, immunity to radio frequency electromagnetic interference, spatial confinement, and low power consumption, VLC is also an energy efficient green technology [5]. In indoor navigation it is also a promising application, where GPS signals are inefficient walls and other obstacles greatly attenuate GPS signals. As in VLC the density of optical transmitters addresses a high density of beacons, visible light enables a higher level of accuracy on location [6][7]. This is the key to provide guidance and navigation services.

The focus of this paper is the use of VLC to implement an indoor positioning system with added communication abilities. The system is composed of a pinpin heterostructure a:SiC:H [8] device to perform the photodetection of the optical signals generated by white trichromatic RGB LEDs. The photodetector [9][10] is based on a-SiC:H/a-Si:H heterostructures, operating therefore in the visible spectrum. It exhibits active filtering and amplification properties and a selective sensitivity, as its design was tailored to address a wavelength sensitive device [11][12]. When different visible signals are encoded in the same optical transmission path, the device multiplexes the different optical channels, performs different filtering processes (amplification, switching, and wavelength conversion) and outputs a multiplexed signal. Decoding of this signal enables the recovery of the modulated signal transmitted by each emitter [13]. This procedure demands accurate regulation of each photocurrent level [14] to produce a reliable calibration curve. On-Off keying modulation and Manchester codes will be used to analyze bit decoding from the multiplexed signal.

The paper is organized as follows. After the introduction (Section I), the VLC system specifications is presented in Section II covering the transmitter and receiver, data coding, modulation schemes and the calibration for decoding. In Section III experimental scenarios are detailed and the obtained results are presented and discussed. Conclusions and guidelines for future work are addressed in Section IV.

II. VLC SYSTEM SPECIFICATIONS

This section covers the specifications of the VLC system, including the transmitter, receiver, coding and modulation techniques.

A. VLC Transmitter

Transmission of data is carried out by one modulated chip using white polychromatic RGB LEDs. The modulation and conversion from digital to analog data is software defined. Four LEDs are mounted in square arrangement on VLC transmitters using one red or blue emitter in each LED for data transmission. In each VLC transmitter two blue and two red emitters are modulated. The remaining emitters do not communicate.

The photodetector used in the receiver unit is a photodiode composed of a pinpin heterostructure based on a-SiC:H/a-Si:H. It exhibits active filtering and amplification properties and a selective sensitivity, as its design was tailored to address a wavelength sensitive device in the visible spectrum. In this photodiode, two a-Si:H pins are mounted on top of one a-SiC:H pin, which allows the device to be used over the full visible spectrum. The device is operated under reverse bias to improve collection efficiency. Steady state optical bias using short visible wavelength (400 nm) is used to improve amplification of the longer wavelengths and attenuation of the short ones. Fig. 1 shows the plot of the spectral emission of three optical emitters of the VLC transmitter and the spectral sensitivity of the sensing photodiode.
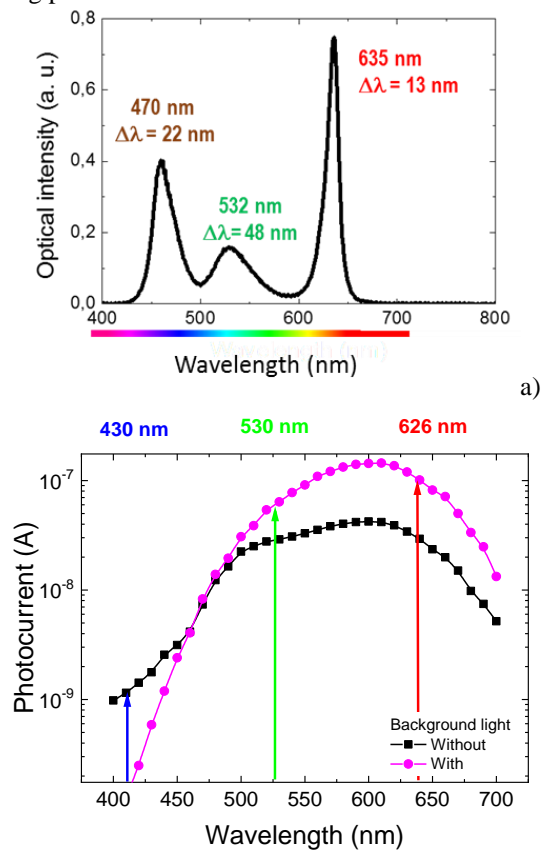

a)

b)

Fig. 1. a) Spectral emission of thee VLC transmitter and b) spectral sensitivity of the VLC receiver.

B. Channel model

A Lambertian beam distribution for each LED was used to model the VLC channel. The channel gain was computed using line-of-sight conditions that included both the transmitter and receiver devices' fields of view. Fig. 2 shows the map of the coverage signal on a 2D representation, due to the four emitters located at the corners of a square configuration. The map representation is expressed in dBm. At the center of the region, there is the highest power signal because there is contribution from all four emitters. There is less received power at the corners, as only three emitters contribute to the signal, while it is even less at the sides, where only two emitters participate.
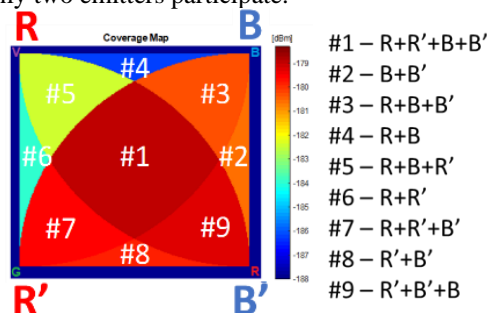

Fig. 2. Signal coverage produced by each emitter and definition of the footprints enabled by the signals transmitted by each emitter.

The optical signals reaching each position determine the spatial coverage of the VLC transmitter. Therefore, the position can be inferred more accurately inside this delimited area. In this coverage area, each optical excitation is assigned to a specific footprint. Fig. 1shows the unit navigation cell and the footprints associated with it. Those footprint regions marked #1, #2, ..., #9 correspond to the optical excitations shown also on Fig. 2.

C. Data coding

Specific data codes are needed to define the communication link and the type of message to be transmitted. In every channel, it was used synchronous transmission based on a data frame of fixed length. Synchronization of the frames can be enabled using different approaches. The SoT is placed at the beginning of the frame and the EoT at the end. Then a TYPE block with 4 bits is used to define the type of message (0000 in request/acknowledge mode, 0011 in standard/update mode). The complete structure of the data frame has the format displayed in Fig. 3.
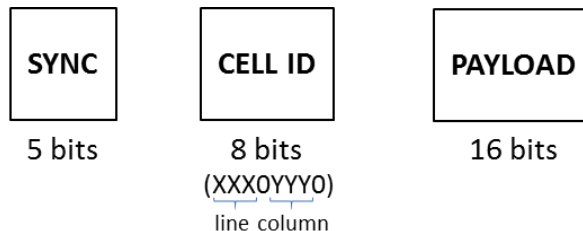

Fig. 3. Data frame structure of the VLC communication channel.

The block labelled GEO-LOCATION (16 bits) identifies the cell and footprint. The cell identification is coded as XXX0YYY0, where XXX addresses the line and YYY the column of the cell. The footprint is produced by coding the R and B emitters with four bits set to 1 and four bits set to 0, while the R' and B' emitters are coded with two bits set to 1 and two bits set to 0, and then two bits set to 1 and two bits set to 0. The 36 bits MESSAGE block addresses specific instructions transmitted to the user and depends on the type of communication mode.

D. Modulation schemes

Data transmission demands the use of a specific modulation scheme. Here we will use both On-Off Keying (OOK) and Manchester. OOK has proven to be a valuable modulation scheme in VLC due to its low complexity and ease of implementation, but it still severely limits data rates, which is further exacerbated by systems using different dimming levels. This paper aims to look at OOK and Manchester coding VLC modulation techniques with distinct levels of complexity, allowing for a comparative evaluation between the two.

OOK assigns different levels of amplitude to each of the data bits we wish to modulate, with a bit time duration of b_t. Manchester assigns both levels to each bit, one per bit time duration b_t, but it is the transitions from on to off ("on-off") or off to on ("off-on") that distinguish between '0' and '1' data bits. In this paper the Manchester codes use the convention of considering "off-on" transitions as '0's and "on-off" transitions as '1's. The representation under OOK and Manchester modulations is shown in Fig. 4.
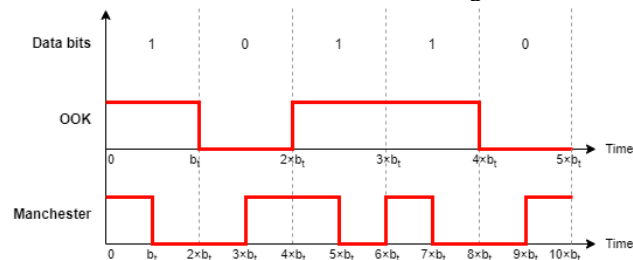

Fig. 4. Representation of data bits in OOK and Manchester, in the time domain.

Data transmission in Manchester is halved since it takes twice as long to transmit the "on" or "off" pulses that encode the same information as in OOK. In contrast, Manchester forces at least one level transition per bit of data, leading to lower levels-permanence, even in long sequences of the same bit.

E. Calibration for decoding

With each optical emitter data transmission, a multiplexed signal is produced at the photodetector. Due to the VLC transmitter's four independent emitters, the output optical signals can combine one, two, three, or four optical excitations. If the driving currents for each emitter are adjusted correctly, this can produce 16 different optical combinations and therefore 16 different photocurrent levels.

The bit decoding of the multiplexed signal corresponds to the correct assignment of each photocurrent level to the respective optical excitation. This is provided using a previous system calibration, by adjusting the photocurrent levels of the multiplexed signal. Since Manchester codes demand the double of the bits to encode the same information, each 'on' or 'off' state of the LED produces two adjacent photocurrent levels.

Fig. 5 shows the calibration signal with 16 levels assigned to each input optical state. The optical signal transmitted by each emitter is displayed on top of the picture. The multiplexed signal is shown under OOK and Manchester modulations.
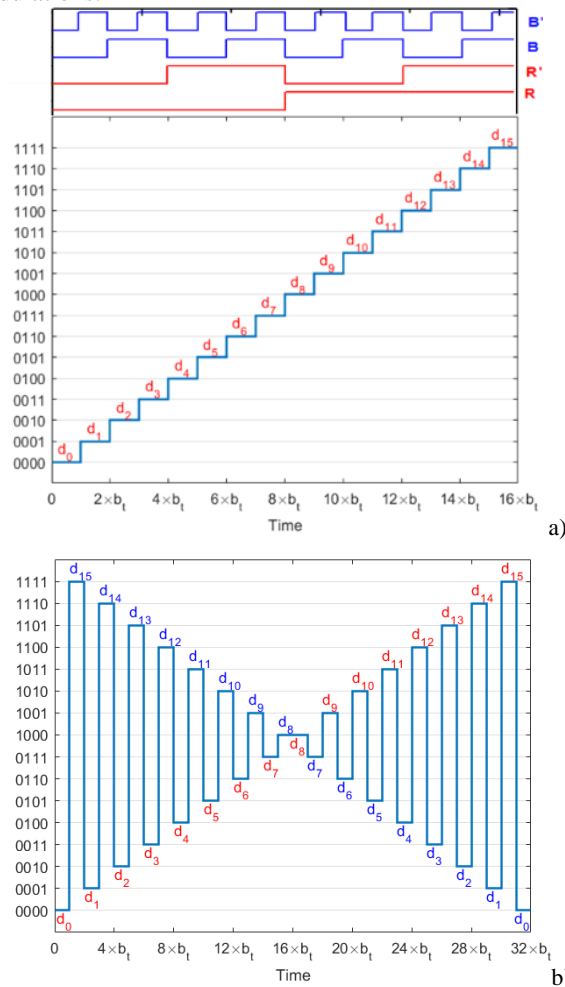

Fig. 5. Calibration curve for a) OOK modulation; b) Manchester codes.

In OOK modulation (Fig. 5a), the set of 16 distinct calibration levels produce a staircase-like shape in the MUX signal, each associated with a particular optical excitation type. The left side of Fig. 6 a) indicates the correspondence of the optical state RR'BB' and the level label (d_i, i =0, 1, …, 15) using binary notation. When using Manchester codes (Fig. 5b), the same data bit sequence takes twice as long as OOK, which half the data rate. The calibration curve takes on a very different shape. This occurs because of how

Manchester uses 2 bits to represent each data bit, leading to the calibration curve having a shape of two alternating OOK calibration curves with one rising branch and the other falling branch.

III. RESULTS AND DISCUSSION

In this study, different optical signals were generated by the four optical transmitters of each LED lamp, using OOK and Manchester codes to infer about the decoding process. The transmitted frame has 29 bits, including a 5 bit synchronization header followed by the cell ID with 8 bits and a 16 bit randomly generated message.

Fig. 6 shows the acquired multiplexed signal under OOK and Manchester coding. On top of the figure the optical signals transmitted by each transmitter are also represented. The signals of the R and B LEDs are represented by the solid red and blue lines, and R' and B' LEDs by the red and blue dashed lines, respectively.
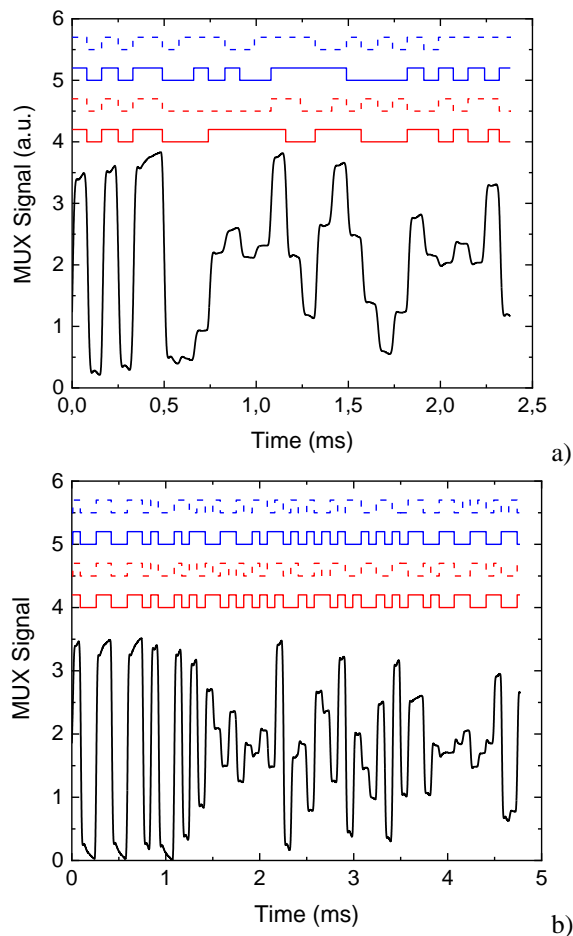

Fig. 6. Transmitted data message using: a) OOK and b) Manchester modulations (R and B are represented by the solid red and blue lines, and R' and B' by the red and blue dashed lines, respectively).

The output resultant signal acquired by the receiver device shows different levels of photocurrent that can be assigned to the correspondent optical excitation. As the device exhibits capacitive effects, the photocurrent level exhibits a rising or falling slope, dependent whether the

transition occurs from a lower to an upper level, or vice-versa. Consequently, this effect becomes more evident when two or more adjacent bits have the same state.

In OOK modulation as the bit states are simply represented by '0's or '1's, it is possible that the signal contains many similar adjacent symbols ('1s' or '0s'), which reinforce this effect. It is clear from Fig. 6a) that, for example, the upper levels achieved by every single 'on' bit are lower than those obtained by two adjacent 'on' bits. This may induce errors in the bit decoding process. When using Manchester coding, Fig. 6b) each state is represented with a transition between different states. Therefore, no more of two similar bits occur during the transmission and the limitations imposed by the capacitive effects of the sensing device are attenuated.

On the other hand, frame synchronization that is established by the heading block transmitted in the beginning of each frame is crucial to ensure correct data transmission. As this block is composed of a sequence of 5 specific states ('on'-'off'-'on'-'off'-'on') followed by the identification labels of the transmitting cells, the correct identification of the block among the transmitted frames is not a hard issue to complete successfully. Nevertheless, under Manchester coding a level transition is less likely to coincide with the start of a frame due to the halved data rate, or even with the start of a data bit since a transition is forced to occur in the middle of each data bit. An effective way of ensuring synchronization is to allocate more bits to the synchronization header block at the cost of the payload length.

Direct comparison of the signal levels with the calibration signal is achieved by assigning the bit level to the level closest to the calibration signal. Bits represented by close values may be improperly decoded. This is especially important when using OOK modulation, since capacitive effects can mislead the decoded level, whereas Manchester modulation minimizes this problem. Parity check bits are a possible solution to reduce the bit error decoding.

IV. CONCLUSIONS

The proposed application focuses on the technique of decoding the multiplexed signal measured by the VLC receiver using OOK and Manchester modulations. The VLC transmitter uses RGB white LEDs to illuminate the space and to transmit information defining footprints inside each navigation cell. Coding uses frames coded with different information blocks. As the multiplexed signal results from multiple optical channels, its waveform is complex. It is necessary to use decoding techniques to determine the correct bits transmitted by each optical channel. Improvements to the decoding technique include parity check error control. The imposed state transitions for the representation of each bit used in Manchester coding minimizes the capacitive effects of the sensing photodiode. As a result, photocurrent levels were better defined for each state.

Improvements to the decoding technique include parity check error control. More experimental data and different

operating scenarios can be used to further enhance the decoding techniques.

REFERENCES

[1] A. M. Căilean and M. Dimian, "Current Challenges for Visible Light Communications Usage in Vehicle Applications: A Survey". IEEE Communications Surveys & Tutorials 2017, vol. 19, no. 4, pp. 2681-2703. doi: 10.1109/COMST.2017.2706940 364.

[2] M. Z. Chowdhury; Hossan, M. T; Islam, A.; Jang, Y. M. A Comparative Survey of Optical Wireless Technologies: Architectures and Applications. IEEE Access 2018, vol. 6, pp. 9819-9840, doi: 10.1109/ACCESS.2018.2792419

[3] L. N. Alves, L. Rodrigues, J. Cura, "Lighting and Communications: Devices, Systems", em Zabih Ghassemlooy, Luis Nero Alves, Stanislav Zvanovec, Mohammad-Ali Khalighi, "Visible Light Communications: Theory and Applications", CRC Press, Taylor & Francis Group, June, 2017, ISBN: 9781498767538.

[4] P. H. Pathak, X. Feng, P. Hu, P. Mohapatra, Visible Light Communication, Networking, and Sensing: A Survey", Potential and Challenges. IEEE Communications Surveys Tutorials 2015, vol. 17, pp. 2047–2077.

[5] H. Haas, L.Yin, Y. Wang, and C.Chen, "What is LiFi?," J. Lightwave Technol. 34, 1533-1544, 2016.

[6] M.F. Keskin, A.D. Sezer, S. Gezici, "Localization via Visible Light Systems", Proceedings of the IEEE 2018, 597 106, pp. 1063–1088. doi:10.1109/JPROC.2018.2823500

[7] Y. Zhuang et al., "A Survey of Positioning Systems Using Visible LED Lights". IEEE Communications Surveys Tutorials, 2018, vol. 20, pp. 1963–1988.

[8] M. Vieira, M. Fernandes, J. Martins, P. Louro, A. Maçarico, R. Schwarz, and M. Schubert, "Improved Resolution in a p-i-n Image Sensor by Changing the Structure of the Doped Layers", Amorphous and Heterogeneous Silicon Thin Films-2000, Mat. Res. Soc. Symp. Proc., S. Francisco, April 24-28 U.S.A., Vol. 609, 2000.

[9] M. A. Vieira, M. Vieira, V. Silva, P. Louro "Optical signal processing for indoor positioning using a-SiCH technology" Proc. SPIE 9891, Silicon Photonics and Photonic Integrated Circuits V, 98911Z, 2016.

[10] P. Louro, M. Vieira, M. Fernandes, J. Costa, M. A. Vieira, J. Caeiro, N. Neves, M. Barata, "Optical demultiplexer based on an a-SiC:H voltage controlled device", Phys. Status Solidi C vol. 7, No. 3–4, pp. 1188–1191, 2010. DOI: 10.1002/pssc.200982702.

[11] P Louro, V Silva, I Rodrigues, M.A. Vieira, M Vieira "Transmission of Signals Using White LEDs for VLC Applications" - Materials Today: Proceedings, vol. 3, no. 3, 2016, pp. 780–787 doi:10.1016/j.matpr.2016.02.009.

[12] M. A. Vieira, M. Vieira, P. Louro, V. Silva, A. S. Garção, "Photodetector with integrated optical thin film filters", Journal of Physics: Conference Series 421, 2013, 01201, http://iopscience.iop.org/1742-6596/421/1/012011/. doi:10.1088/1742-6596/421/1/012011.

[13] P. Louro, M. Vieira, M. A. Vieira, "Geolocalization and navigation by visible light communication to address automated logistics control," Opt. Eng. Vol. 61, no. 1, 016104, 2022, doi: 10.1117/1.OE.61.1.016104.

[14] P. Louro, M. Vieira, M. A. Vieira, "Bidirectional visible light communication," Opt. Eng. Vol. 59 no. 12, pp. 127109, 2020, doi: 10.1117/1.OE.59.12.127109.